



HAL
open science

New echocardiographic imaging modalities for guiding and monitoring of therapy by focused ultrasound of calcified aortic stenosis

Daniel Suarez Escudero

► **To cite this version:**

Daniel Suarez Escudero. New echocardiographic imaging modalities for guiding and monitoring of therapy by focused ultrasound of calcified aortic stenosis. Physics [physics]. Université Paris sciences et lettres, 2019. English. NNT : 2019PSLET015 . tel-02946265

HAL Id: tel-02946265

<https://pastel.hal.science/tel-02946265>

Submitted on 23 Sep 2020

HAL is a multi-disciplinary open access archive for the deposit and dissemination of scientific research documents, whether they are published or not. The documents may come from teaching and research institutions in France or abroad, or from public or private research centers.

L'archive ouverte pluridisciplinaire **HAL**, est destinée au dépôt et à la diffusion de documents scientifiques de niveau recherche, publiés ou non, émanant des établissements d'enseignement et de recherche français ou étrangers, des laboratoires publics ou privés.

THÈSE DE DOCTORAT
DE L'UNIVERSITÉ PSL

Préparée à l'École supérieure de physique et de chimie industrielles de la ville de Paris (ESPCI)

Laboratoire : Physique pour la médecine Paris

Nouvelles modalités d'imagerie échocardiographique pour le guidage et le monitoring du traitement par ultrasons focalisés de la sténose aortique calcifiée

New echocardiographic imaging modalities for the guidance and monitoring of focused ultrasound therapy for the treatment of calcified aortic stenosis

Soutenue par

Daniel SUAREZ

Le 14 octobre 2019

Ecole doctorale n° 564

Physique en Île-de-France

Spécialité

Physique

Composition du jury :

| | |
|--|------------------------------|
| Bijan, GHALEH-MARZBAN PU/PH, INSERM | <i>Président</i> |
| David, MELODELIMA Directeur de recherche, INSERM | <i>Rapporteur</i> |
| Jean-Michel, ESCOFFRE Chargé de recherche, INSERM | <i>Rapporteur</i> |
| Claire, PRADA Directrice de recherche, CNRS | <i>Examinatrice</i> |
| Fabienne, BETTING Ingénieure, Cardiawave SA | <i>Examinatrice</i> |
| Eric, SALOUX PH, CHU de Caen | <i>Examineur</i> |
| Mathieu, PERNOT Directeur de recherche, INSERM | <i>Directeur de thèse</i> |
| Mickael, TANTER Directeur de recherche, INSERM | <i>Co-directeur de thèse</i> |

Confidentielle jusqu'au 31 août 2019



Aux papys qui vont pouvoir améliorer leur qualité de vie

To grandpas who will be able to improve their quality of life

Acknowledgements

I first want to thank Fabienne Betting and Mathieu Pernot, the first two people I met in the lab, those who trusted me and guided me through these very exciting years of work. This thesis was for me a true dream job. Thank you, Fabienne, for your kindness, your management, the experience you passed on to me and of course for all the conversations we could have besides work. Thank you, Mathieu, for all the good ideas, your patience, your experimental knowledge and for helping me even in the very small problems. I am also very grateful to my other supervisor Mickaël Tanter, the head of the lab, a source of inspiration for the team who has helped and encouraged me throughout. Finally, I want to thank Benjamin Bertrand, Cardiawave's CEO, a true leader, who was always receptive, giving advices and encouraging the team.

I had the chance to work in three different places, the laboratory, Physics for Medicine, the hospital, HEGP, and the company, Cardiawave, which allowed me to experience three faces of the biomedical world: research, clinics and industry. The practical and human experience I acquired are truly immeasurable. I want to thank my colleagues from the three worlds, for all the help, the good moments, the good working environment, the coffee breaks even if I do not like coffee and of course for all the science and experience we shared. I did not work alone for this thesis, and there is a lot of people who contributed to this work.

Participating in Cardiawave's preclinical trials was a thrilling and exciting experience. I want to thank Pr. Emmanuel Messas for his kindness and for his clinical knowledge. I also want to thank all the team that helped us for the trials and in particular Julie, Dr. Guillaume Goudot and Dr. Lina Khider. Lastly, I want to thank all the pigs that helped us with preclinical trials, I hope you will forgive us one day.

After the preclinical trials, we got the authorization for the first clinical trial for the non-invasive treatment of aortic stenosis in ten patients. This was much more than thrilling and exciting. I want to thank all of them patients for they courage.

I want to thank Dr. David Melodelima and Dr. Jean-Michel Escoffre, who kindly accepted to be rapporteurs of my work. I also want to thank Dr. Bijan Ghaleh-Marzban, Dr. Eric Saloux and Dr. Claire Prada who accepted to be reviewers for my PhD defense.

I also want to thank my family and friends who are always here.

Finally, for funding this work, I want to thank Cardiawave SA, the ANRT, the ANR-10-IDEX-0001-02 PSL* Research University, the ANR-17-CE19-0019 "Valvosoft" and the European Union's Horizon 2020 research and innovation programme under grant agreement n° 829492.

These have been wonderful three years.

Contents

| | |
|---|--------|
| Acknowledgements | iii |
| Contents..... | iv |
| Table of figures | vii |
| Résumé en français..... | xii |
| I.I La physique des thérapies par ultrasons cavitationnels pulsés (PCUT) | xii |
| I.I.I Physique des ultrasons | xii |
| I.I.II Thérapies ultrasonores à haute intensité | xiii |
| I.I.III L'ingénierie des PCUT | xiv |
| I.II La sténose aortique calcifiée | xv |
| I.II.I Physiologie du cœur..... | xv |
| I.II.II Une dégénérescence valvulaire très répandue | xv |
| I.II.III Une nouvelle approche médicale | xvi |
| I.III Le monitoring des PCUT : challenges et paradigmes actuels..... | xvii |
| II Une nouvelle modalité d'imagerie de cavitation : de la 2D à la 3D..... | xviii |
| II.I Imagerie de cavitation : bref état de l'art | xviii |
| II.II Imagerie passive cohérente : théorie..... | xix |
| II.III Méthodes et preuves de concept..... | xxi |
| II.IV Vers l'imagerie de cavitation 3D..... | xxvi |
| II.V Vers l'imagerie de cavitation bi-plane : un compromis entre la 2D et la 3D ... | xxvii |
| III Conception d'un nouveau transducteur de thérapie pour la thrombotripsie | xxviii |
| III.I La thrombose veineuse profonde | xxviii |
| III.II La thrombotripsie et l'approche de Physique pour la Médecine | xxix |
| III.III Conception d'un nouveau transducteur de thérapie | xxx |
| IV Conclusion | xxx |
| IV Conclusion | xxx |
| General introduction..... | 1 |
| Chapter I - State of art..... | 3 |
| 1.1 The physics of pulsed cavitation ultrasound therapies | 3 |
| 1.1.1 Ultrasound physics | 3 |
| 1.1.2 Focused ultrasound therapies in short | 4 |
| 1.1.3 Inertial cavitation and bubbles behaviour | 4 |
| 1.1.4 The engineering of histotripsy..... | 6 |
| 1.2 Ultrasound imaging for the guiding and the monitoring of PCUT | 8 |
| 1.2.1 B-Mode ultrasound imaging in short | 8 |
| 1.2.2 Focalisation and resolution..... | 10 |
| 1.2.3 Ultrafast imaging..... | 12 |
| 1.2.4 From HIFU monitoring to histotripsy monitoring | 13 |
| 1.3 Calcified aortic stenosis | 14 |
| 1.4 A potential solution for calcified aortic stenosis using a PCUT solution | 17 |
| 1.4.1 Cardiawave SA..... | 17 |
| 1.4.2 Safety and efficacy parameters | 18 |
| 1.4.3 Quick feedback of ultrasound imaging in preclinical trials | 19 |
| 1.4.4 Valvosoft® | 20 |
| Bibliography..... | 22 |
| Part I: New imaging modality for cavitation imaging: from 2D to 3D..... | 26 |
| Chapter II - Passive coherent cavitation imaging..... | 27 |
| 2.1 Introduction | 27 |
| 2.2 Passive coherent imaging and spatiotemporal filter..... | 29 |

| | |
|---|----|
| 2.2.1 Theory | 29 |
| 2.2.2 Experimental setup for coherent passive feasibility..... | 30 |
| 2.2.3 From passive images to cavitation map: the singular value decomposition filter | 32 |
| 2.2.4 Ultrafast active acquisitions | 35 |
| 2.2.5 Cavitation map evaluation..... | 36 |
| 2.3 Experiments and results | 37 |
| 2.3.1 <i>In vitro</i> experiments | 37 |
| 2.3.2 <i>In vivo</i> experiments | 43 |
| 2.4 Axial resolution improvement in coherent passive imaging..... | 48 |
| 2.4.1 Quick Introduction | 48 |
| 2.4.2 Focal spot size and position in simulations..... | 49 |
| 2.4.3 Cavitation cloud size and position using active imaging..... | 51 |
| 2.4.4 Cavitation cloud size and position using coherent passive imaging..... | 53 |
| 2.4.5 Cavitation cloud size and position using coherent passive imaging and adding an extra cycle | 54 |
| 2.4.6 Quick conclusion and discussion | 56 |
| 2.5 Discussion and conclusions..... | 57 |
| Bibliography..... | 60 |
| Chapter III - From 2D to 3D cavitation imaging | 63 |
| 3.1 Introduction | 63 |
| 3.2 3D passive coherent imaging and spatiotemporal filter | 64 |
| 3.2.1 Experimental setup..... | 64 |
| 3.2.2 Results | 66 |
| 3.3 Measurement of ultrasonic attenuation through a swine thorax | 67 |
| 3.3.1 Objective and methods | 67 |
| 3.3.2 Results | 69 |
| 3.4 Cavitation monitoring of an aberrated beam..... | 70 |
| 3.4.1 Introduction | 70 |
| 3.4.2 Setup and methods | 71 |
| 3.4.3 Back to 2D imaging..... | 72 |
| 3.4.4 Cavitation monitoring using 3D imaging..... | 75 |
| 3.4.5 Cavitation cloud three-dimensional shape | 76 |
| 3.5 Discussion and conclusion | 79 |
| Bibliography..... | 80 |
| Chapter IV - From 2D to bi-plane imaging..... | 82 |
| 4.5 Introduction | 82 |
| 4.6 Beamforming methods | 84 |
| 4.6.1 Complete ultrafast delay-and-sum beamforming..... | 84 |
| 4.6.2 Complete delay-and-sum beamforming with an acoustic spherical lens | 85 |
| 4.6.3 Thin lens approximation for delay-and-sum beamforming..... | 87 |
| 4.6.4 Beyond the thin lens approximation for delay-and-sum beamforming..... | 88 |
| 4.6.5 Evaluation of the errors in emission, on simulations | 90 |
| 4.7 Beamforming results | 91 |
| 4.7.1 Material and methods | 91 |
| 4.7.2 Frame rate..... | 92 |
| 4.7.3 Thin less approximation errors..... | 92 |
| 4.7.4 Lateral resolution loss between the P4-2 (Philips©, USA) probe and the PAXY probe (Vermon©, France)..... | 94 |

| | |
|---|-----|
| 4.8 Bi-plane coherent passive cavitation imaging using the PAXY (Vermon©, France) probe..... | 95 |
| 4.9 Conclusion..... | 98 |
| Bibliography..... | 99 |
| Part II: Guidance and safety parameters and procedures for the therapy..... | 101 |
| Chapter V - Focal spot three-dimensional position monitoring challenges | 102 |
| 5.1 Introduction | 102 |
| 5.2 Therapeutic speed of sound..... | 105 |
| 5.2.1 Objective and motivations..... | 105 |
| 5.2.2 Experimental setup | 106 |
| 5.2.3 Methods..... | 106 |
| 5.2.4 Results | 107 |
| 5.2.5 Conclusion..... | 108 |
| 5.3 Alignment verification protocol | 108 |
| 5.3.1 Objectives..... | 108 |
| 5.3.2 Plaster sticks verification protocol | 110 |
| 5.4 Focal spot and cavitation cloud behaviours | 112 |
| 5.4.1 Objectives and motivations | 112 |
| 5.4.2 Numerical simulations..... | 114 |
| 5.4.3 Active cavitation imaging analysis | 116 |
| 5.4.4 Expected results and hypothesis..... | 118 |
| 5.4.5 Results | 119 |
| 5.5 Discussion and conclusions..... | 121 |
| Bibliography..... | 123 |
| Part III: Thrombotripsy | 125 |
| Chapter VI – New transducer design and tools for the improvement of thrombotripsy | 126 |
| 6.1 Introduction | 126 |
| 6.1.1 Deep venous thrombosis in short | 126 |
| 6.1.2 Thrombotripsy | 127 |
| 6.2 New transducer design | 128 |
| 6.2.1 Characteristics and challenges | 128 |
| 6.2.2 Design based on simulations | 129 |
| 6.3 Device improvements, tools and further studies | 134 |
| 6.3.1 Passive cavitation imaging in thrombotripsy | 134 |
| 6.3.2 Following improvements..... | 135 |
| 6.4 Discussion and conclusion | 136 |
| Bibliography..... | 138 |
| General conclusion..... | 140 |
| Annexes | 143 |
| Annexe 1 – Designed therapeutic transducer and imaging probe for thrombotripsy..... | 143 |
| Annexe 2 – Human machine interface designed to control the robotic arm in thrombotripsy | 143 |
| Annexe 3 – 3D coherent passive image rendering while cavitation in water | 144 |
| Annexe 4 – Acoustic characteristics of biological tissues and other materials..... | 145 |

Table of figures

| | |
|--|----|
| Figure 1 – Nucleation, growth and collapse of a bubble while cavitation under an acoustic field [1]..... | 6 |
| Figure 2 - Optical images of bubbles produced by 345 kHz, 500 kHz, 1.5 MHz and 3 MHz histotripsy pulses inside agarose tissue phantoms of increasing Young modulus [8]..... | 7 |
| Figure 3 – A: Typical histotripsy pressures at the focus [5] B: Non-thermal histotripsy common timings showing the typical non-linear waveform at high pressure regimes [5] | 8 |
| Figure 4 - Left: Linear scan Right: Sector scan [20] | 9 |
| Figure 5 - Lateral resolution scheme a) Ultrasound emission. The medium contains two reflectors b) The two points are resolved in the image c) The two points are confused in the image | 11 |
| Figure 6 - Delay law for ultrasound focalisation [20] | 12 |
| Figure 7 - Ultrafast imaging principle [21] (a) Individual plane waves sent with the compound method (b), (c), (d) The coherent synthetic addition of the plane waves with the adequate delays enables lateral and axial focusing..... | 13 |
| Figure 8 – A: Hemodynamic forces during the systole and the diastole in the aortic root [19] B: Cellular architecture of the aortic valve [19] | 15 |
| Figure 9 - Left: Healthy aortic valve Right: Aortic valve with calcified stenosis | 16 |
| Figure 10 - Conventional B-Mode imaging while histotripsy <i>in vivo</i> in a healthy aortic valve, on the pig a) Moment before the cavitation nucleation b) Following frame, where the cavitation cloud begins to grow c) Cavitation over the healthy valve The green dot lines join at the therapeutic target spot | 20 |
| Figure 11 - Valvosoft platform [16]..... | 21 |
| Figure 12 - In vivo B-mode image of the liver during therapeutic exposure with cavitation occurring at the focal zone. The bubble cloud is not easy to differentiate from the tissues. It is located inside the region of interest defined in the image by the green rectangle..... | 28 |
| Figure 13 – Coherent passive image acquisition while cavitation The therapeutic transducer emits focused ultrasound waves, and the backscattered echoes are acquired by the imaging probe. For the beamforming, it is necessary to include the time-delays δt between both transducers..... | 30 |
| Figure 14 –Setup for real-time passive cavitation imaging. The phased array imaging probe, driven by a Verasonics system is attached to the single element therapy transducer. A function generator is used as a master clock..... | 31 |
| Figure 15 - Casorati matrix construction In red is highlighted the first frame | 34 |
| Figure 16 - Timings for the passive and active imaging sequences Pulse repetition frequency = 100 Hz for passive acquisitions and Pulse repetition frequency = 4000 Hz for active acquisitions There is a dead time between the passive and the active acquisition to avoid artefacts on the image | 36 |
| Figure 17 - Set-up for the <i>in vitro</i> experiments..... | 38 |
| Figure 18 – A): In vitro unfiltered passive image while therapeutic pulse emission (no cavitation) B): In vitro unfiltered passive image while therapeutic pulse emission (cavitation) C): In vitro filtered passive image while therapeutic pulse emission (no cavitation) D): In vitro filtered passive image while therapeutic pulse emission (cavitation)..... | 39 |

| | |
|---|----|
| Figure 19 – 2D in vitro cavitation map Contrast-to-Noise Ratio (CNR) evaluation while cavitation A) CNR as a function of p when $n_t=10, q=10$ B) CNR as a function of n_t when $p=2, q=n_t$ C) CNR for different active and passive sequences, when $n_t = 10, p = 2, q = n_t$ Here are presented static tissue and moving tissue conditions..... | 40 |
| Figure 20 - Spatial singular vectors of a passive image while cavitation when $n_t = 10$ | 42 |
| Figure 21 – Upper row: “Active 100 Hz with compounding” B-Mode and derived cavitation maps, in static and moving conditions Lower row: Passive image and derived cavitation maps, in static and moving conditions | 43 |
| Figure 22 – Complete monitoring sequence. The passive cavitation map is overlaid onto the B-Mode image for the bubble cloud anatomic localization in real time | 44 |
| Figure 23 – A) Passive cavitation map Region of Interest (ROI) average backscattered intensity as a function of the estimated minimal focal pressure, in vitro and in vivo B) B-Mode, passive cavitation map and active cavitation map normalized dB Region of Interest (ROI) average backscattered intensity as a function of the estimated minimal focal pressure, in vivo Error bars show the standard deviation with $n = 30$ | 46 |
| Figure 24 – Contrast-to-Noise Ratio (CNR) of the the active and the passive cavitation maps for each <i>in vivo</i> experiment, when $n_t = 10, p = 2, q = n_t$ | 47 |
| Figure 25 – Monitoring sequence. A and B: Examples of overlays of the cavitation map over the B-Mode, on two different views of the liver | 47 |
| Figure 26 - Simulation parameters for the acoustic propagation of ultrasound using different number of cycles per burst | 49 |
| Figure 27 - For different number of cycles: Top left: focal spot maximal pressure Top right: focal spot centroid position in depth Bottom left: focal spot minor axis dimensions at -3 dB Bottom right: focal spot major axis dimensions at -3 dB..... | 50 |
| Figure 28 - Simulation results of bursts containing one cycle (left) and 35 cycles (right)..... | 50 |
| Figure 29 - Cavitation cloud size and position following different number of burst cycles The positions are relative to a region of interest. $N = 100$ | 52 |
| Figure 30 - Results of cavitation imaging. Top left: 10 cycles Top right: 20 cycles Bottom left: 30 cycles Bottom right: 40 cycles | 52 |
| Figure 31 - Coherent passive cavitation imaging for different number of cycles per burst We can see that the axial resolution decreases with the number of cycles | 53 |
| Figure 32 - Cavitation cloud size and position following different number of burst cycles. $N = 100$ The positions are relative to a region of interest..... | 54 |
| Figure 33 – Timings of the ultrasound emission sequence intended to improve coherent passive imaging resolution while histotripsy We an extra cycle 300 μ s after the main histotripsy burst | 54 |
| Figure 34 – Left: Passive image while cavitation, 20 cycles Right: Passive image while cavitation, 20 cycles and an extra cycle | 55 |
| Figure 35 - Cavitation cloud size and position following different number of burst cycles and an extra cycle for passive imaging. $N = 100$ The positions are relative to a region of interest..... | 56 |
| Figure 36 – B-Mode image of histotripsy over a bioprosthetic valve The bubble cloud, outlined in green, presents an asymmetrical shape | 64 |
| Figure 37 - 3D in vitro passive cavitation map Contrast-to-Noise Ratio (CNR) evaluation while cavitation A) CNR as a function of p when $n_t=10, q=10$ B) CNR as a function of n_t when $p=2, q=n_t$ | 66 |

| | |
|---|----|
| Figure 38 - 3D passive cavitation map over volumetric B-Mode A: Plane X = 128/256. B: Plane Y = 128/256. C: 3D rendering The voxel size is 0.7 mm x 0.7 mm x 0.7 mm | 67 |
| Figure 39 - Setup for ultrasonic attenuation measurement trough the ribs of a swine model | 69 |
| Figure 40 - Human ribs placed in front of the therapeutic transducer to create an aberration The imaging fields in front of the probes are not aberrated, Left: P4-2 phased array (Philips [®] , USA) Right: 32x32 matrix array (Vermon [®] , France) | 72 |
| Figure 41 - Histotripsy in water while emitting trough human ribs a) B-Mode b) Active cavitation map (CM) c) Passive cavitation map (CM) | 73 |
| Figure 42 - B-Mode of histotripsy through human ribs in degassed water From left to right, we can appreciate frame by frame a second cavitation cloud nucleation, pointed by the green arrow, that will join the main cavitation cloud Estimated imaging frame rate: 20 frames per second | 74 |
| Figure 43 - 3D passive cavitation map while histotripsy through human ribs in degassed water Left: Plane X = 128/256. Right: Plane Y = 128/256..... | 75 |
| Figure 44 - 3D passive cavitation map while histotripsy through human ribs in degassed water Left: Plane X = 128/256. We can observe inside the blue circle a second cavitation cloud Right: Plane Y = 128/256 | 76 |
| Figure 45 - Human ribs placed in front of the therapeutic transducer to create an aberration The imaging field in front of the 32x32 matrix array (Vermon [®] , France) is not aberrated The transducer is placed to generate cavitation over a human calcified aortic valve leaflet | 77 |
| Figure 46 - Histotripsy through human ribs over a calcified human aortic valve leaflet a): B-Mode b), c): 3D passive cavitation map b): Plane X = 128/256. C): Plane Y = 128/256 | 78 |
| Figure 47 - Scheme: red: cavitation cloud, grey: Imaging plane Left: cavitation monitoring using a single plane Right: cavitation monitoring using two orthogonal X and Y planes The shape of the bubble cloud vary following the imaging plane position | 78 |
| Figure 48 - PAXY probe including a convex cylindrical acoustic lens | 83 |
| Figure 49 - Complete image beamforming (with no acoustic lens) | 85 |
| Figure 50 - Complete imaging beamforming with an acoustic lens | 86 |
| Figure 51 - Thin lens approximation imaging beamforming with an acoustic lens The FD is not corrected..... | 87 |
| Figure 52 - Thin lens approximation imaging beamforming with an acoustic lens The FD is corrected..... | 89 |
| Figure 53 - K-wave simulation environment for the source position correction using time reversal Sensors pitch: 0.15 mm | 90 |
| Figure 54 - Received emissions on the array after the lens. Time is in ns Left: The sensor array is placed 1 cm after the lens Right: The sensor array is placed 20 cm after the lens Blue: Without any correction Red: Thin lens beamforming with source correction Green: Complete beamforming without approximations | 91 |
| Figure 55 - Bi-plane B-Mode X and Y orthogonal planes of an imaging phantom using the PAXY (Vermon [®] , France) probe with a dynamic range of 50 dB Up: Complete beamforming Down: Thin lens approximation with source correction beamforming..... | 92 |
| Figure 56 - 6 points used to evaluate the dB loss between the complete beamforming and the thin lens approximation beamforming | 93 |

| | |
|--|-----|
| Figure 57 – B-Mode of an imaging phantom with a dynamic range of 50 dB using: Left: The P4-2 probe (Philips©, USA) Right: The PAXY probe (Vermon©, France) (thin lens approximation with source correction beamforming)..... | 95 |
| Figure 58 - Bi-plane cavitation maps while histotripsy on a PVA phantom using the PAXY probe Left: X plane Right: Y plane..... | 96 |
| Figure 59 - CNR for cavitation maps evaluation using the P4-2 probe and the PAXY probe | 97 |
| Figure 60 - Bi-plane passive cavitation map while histotripsy in a PVA phantom using the PAXY probe Left: X plane. We can observe inside the blue circle a second cavitation cloud Right: Y plane | 97 |
| Figure 61 – Electronic steering along the central axis of the transducer..... | 104 |
| Figure 62 – a) 3D representation of both therapeutic and imaging fields volumes b) Representation of misaligned therapeutic and imaging planes c) Representation of aligned therapeutic and imaging planes..... | 109 |
| Figure 63 - Alignment protocol target points P1, P2 P3 O represents the origin of the imaging plan and O' represents the bottom The target points are not aligned and cover the whole steering range of the transducer.. | 110 |
| Figure 64 - Imaging plane volume | 111 |
| Figure 65 - Setup for the qualitative alignment verification protocol | 112 |
| Figure 66 - Result of the alignment verification protocol when both transducers are aligned | 112 |
| Figure 67 - Scheme of the simulation environment. Blue: water; White: imaging probe and therapeutic transducer Source for absorption value: [4]. The imaging probe acts as a reflector. | 115 |
| Figure 68 - Scheme of the simulation environment. Blue: water; Red: tissue; White: imaging probe and therapeutic transducer. Left: no tilt. Right: 10° tilt Source for tissue and absorption: [4]. The imaging probe acts as a reflector..... | 115 |
| Figure 69 - a) Setup without the Zerdine with no tilt b) Setup with the Zerdine with no tilt c) Setup without the Zerdine with a transducer tilt of 10° d) Setup with the Zerdine with a Transducer tilt of 10° | 116 |
| Figure 70 - a) Raw B-Mode image acquired by Valvosoft® during the cavitation experiment, through Zerdine®, at a therapeutic target depth of 85mm with no tilt and b) corresponding cavitation cloud segmentation c) Raw B-Mode image acquired by Valvosoft during the cavitation experiment, through water, at a therapeutic target depth of 85mm with a 10° Transducer tilt and d) corresponding cavitation cloud segmentation To be noted that the imaging depths are different for a) and for c) | 117 |
| Figure 71 – Up: Simulated pressure field for a therapeutic target depth of 80 mm in mediums containing tissue without tilt (left) and with a transducer tilt of 10° (right). Down: Simulated pressure field for a therapeutic target depth of 160 mm in mediums containing tissue without tilt (left) and with a transducer tilt of 10° (right) The scan head is visible at the top of the map. The colorbar represents the pressure. To be noted: the colorbar scale is not the same between both images..... | 120 |
| Figure 72 - Example of venous thrombosis [3]..... | 126 |
| Figure 73 - Recanalization of the thrombotic vein, allowing the blood flow to go through the clot..... | 127 |
| Figure 74 - Scheme presenting the thrombotripsy basic elements and the new transducer's steering range objective along its central axis | 129 |
| Figure 75 - Transducer's principal characteristics to be defined | 130 |
| Figure 76 - Scheme of the simulation environment. White: Imaging probe (Y plane); Yellow: tissue; Blue: therapeutic transducer. Source for tissue and absorption: [5]. The imaging probe acts as a reflector..... | 132 |

| | |
|--|-----|
| Figure 77 - Upper row: X plane (left) and Y plane (right) of the simulated pressure field for a therapeutic target depth of 20 mm under the probe Lower row: X plane (left) and Y plane (right) of the simulated pressure field for a therapeutic target depth of 60 mm under the probe..... | 133 |
| Figure 78 - Steering range of the proposed multi-element transducer | 134 |
| Figure 79 – Left: Cavitation cloud while thrombotripsy <i>in vivo</i> Right: Cavitation cloud while thrombotripsy <i>in vivo</i> over B-Mode..... | 135 |

Résumé en français

I.I La physique des thérapies par ultrasons cavitationnels pulsés (PCUT)

I.I.I Physique des ultrasons

Le son est une onde mécanique longitudinale qui produit un déplacement de particules dans un milieu donné : il s'agit d'une suite de compressions et de raréfactions. L'onde est caractérisée par son amplitude, sa fréquence et sa longueur d'onde. Le son audible par l'homme est compris entre 20 et 20000 Hz, et les ondes de fréquence située au-dessus de cette bande sont dites ultrasonores. Dans le domaine médical, on travaille généralement dans une plage comprise entre 1 et 20 MHz, avec une pression maximale de l'ordre de 3 MPa pour l'imagerie. En milieu fluide, où c est la Vitesse de l'onde, χ_s le coefficient de compressibilité adiabatique et ρ_0 la densité du milieu, nous avons :

$$c = \sqrt{\frac{1}{\chi_s \rho_0}} \quad (1)$$

La vitesse du son dépend donc du milieu de propagation, et respecte l'équation suivante où λ est la longueur d'onde et f est la fréquence d'émission :

$$\lambda = \frac{c}{f} \quad (2)$$

On définit l'impédance acoustique comme la réaction d'un matériau au passage de l'onde sonore. Ainsi, une interface acoustique sépare des milieux ayant une impédance acoustique différente. En échographie on s'intéresse notamment au coefficient de réflexion R , qui quantifie la proportion d'onde qui sera réfléchi à la rencontre d'une interface acoustique. Un coefficient égal à 0 indique que l'onde est complètement transmise, et un coefficient égal à 1 indique que l'onde est complètement réfléchi. Nous avons :

$$R = \frac{z_2 - z_1}{z_2 + z_1} \quad (3)$$

Enfin, deux phénomènes sont à prendre en compte lors de l'étude du son : l'absorption et la diffusion. L'absorption a pour conséquence la dissipation de l'énergie dans le milieu, qui peut se transformer en chaleur. La diffusion a comme conséquence que l'onde se divise dans plusieurs directions.

Lors de sa propagation dans un tissu, les ondes vont ainsi s'atténuer. En effet, l'absorption et la diffusion de l'onde imposeront des limites d'utilisation notamment en échographie où la profondeur d'exploration sera limitée. Il est possible de quantifier l'atténuation grâce au coefficient d'atténuation, mesuré en dB/cm et différent cependant selon les milieux de propagation.

I.I.II Thérapies ultrasonores à haute intensité

Les thérapies par ultrasons focalisées à haute intensité sont des procédures chirurgicales non invasives permettant d'induire un effet mécanique souvent destructif sur un point focal précis. Il s'agira généralement d'effets de chauffe, de coupe ou de réduction de tissus cibles pathologiques. Les impulsions ultrasonores sont émises par des transducteurs mono-éléments ou multi-éléments à focalisation géométrique et/ou électronique, utilisant dans ce dernier cas des lois de retard entre les éléments.

Les premières procédures réussies remontent aux années 1980 pour des applications ophtalmologiques et reposent sur des effets thermiques conduisant à la nécrose irréversible des tumeurs. On commence à parler d'ultrasons focalisés de haute intensité (HIFU, en anglais), caractérisés par une élévation importante de la température au point focal due à l'absorption ultrasonore. Depuis, les thérapies par ultrasons ont été largement développées pour différentes applications médicales dans différents organes du corps humain, et on peut trouver aujourd'hui trois principales modalités thérapies par ultrasons focalisées :

- Les HIFU, qui repose sur l'action thermique produite par l'émission d'impulsions longues avec une pression focale généralement autour de 8 MPa, principalement utilisée en oncologie pour la nécrose tumorale ;

- La lithotripsie, qui repose sur l'émission d'impulsions courtes avec une pression focale généralement autour de 40 MPa, entraînant des effets mécaniques dus aux ondes de choc et à des bulles de cavitation non contrôlées, principalement utilisées pour la réduction des calculs rénaux [30];

- Les thérapies par ultrasons cavitationnels pulsés (PCUT), telles que l'histotripsie, qui reposent sur l'action de bulles de cavitation inertielle nucléées, avec une pression focale généralement d'environ 100 MPa. Cette thèse portera sur cette dernière modalité.

Plus en détail dans notre cas, la cavitation est un phénomène qui consiste en la création et l'oscillation de bulles de gaz dans un fluide compressible, à la suite de l'introduction d'une pression acoustique négative suffisante. La pression négative provoque le changement d'état du fluide, qui est séparé aux endroits contenant des impuretés gazeuses. Des cavités, ou « bulles », vont alors se former, s'élargir et potentiellement s'effondrer. Dans le cas de la cavitation inertielle, les bulles vont s'effondrer violemment après quelques oscillations en générant un flux localisé et des ondes de choc, et induisant un effet mécanique dans le milieu environnant. Nous aurons affaire plus précisément à des microbulles qui, ensemble, formeront un nuage de bulles dense dans une zone cible précise.

Les propriétés et le comportement des bulles sont complexes et dépendent des propriétés du tissu sonifié, ainsi que des paramètres acoustiques tels que la durée des impulsions, l'intensité ou le rapport cyclique. Le rayon des bulles est par exemple proportionnel à la longueur d'onde des ultrasons, qui dépend à son tour de la fréquence des ultrasons et du milieu de propagation.

I.I.III L'ingénierie des PCUT

Les PCUT regroupent donc les processus consistant à générer et à contrôler des bulles de cavitation inertielle pour des applications médicales. Ils reposent sur l'émission d'impulsions ultrasonores focalisées très courtes, intenses et répétées avec un faible rapport cyclique, induisant une pression négative dans le milieu à l'intérieur d'un point focal précis, et provoquant la nucléation d'un nuage de cavitation inertielle dense et énergétique. L'implosion de bulles aura une action mécanique non thermique sur les tissus environnants.

Un transducteur acoustique se chargera d'émettre de courtes rafales d'ondes ultrasonores sinusoïdales, celles-ci se focalisant à leur tour dans la zone cible. Les sinusoïdes seront émises à une fréquence centrale comprise entre 700 kHz à 4 MHz, constituées de 1 à 20 cycles par rafale et à une fréquence de répétition des rafales comprise entre 1 et 1000 Hz. Les PCUT produisent localement des pressions allant jusqu'à 100 MPa et jusqu'à -25 MPa.

Il faut garder à l'esprit que les PCUT ont des nombreuses applications. Entre autres, la création d'une communication inter-auriculaire, la réduction du tissu adipeux, la thrombolyse, le traitement du cancer du foie ou l'hyperplasie de la prostate sont en cours de développement.

I.II La sténose aortique calcifiée

I.II.I Physiologie du cœur

Le cœur est un organe vital qui assure la circulation du sang dans le corps à travers deux systèmes principaux : la circulation pulmonaire et la circulation systémique. Le cœur est comparable à une pompe à pistons qui, grâce à l'ouverture et fermeture de quatre valves, va rythmer de manière synchrone le flux sanguin dans ces deux systèmes. Cette activité mécanique est coordonnée par un influx électrique, qui assure la synchronisation du mouvement.

Le cœur se compose en effet de quatre chambres : deux oreillettes et deux ventricules. L'oreillette droite communique avec le ventricule droit via la valve tricuspide et l'oreillette gauche communique avec le ventricule gauche via la valve mitrale. De même, le ventricule droit communique avec l'artère pulmonaire via la valve pulmonaire et le ventricule gauche communique avec l'artère aorte via la valve aortique. Lors de la contraction (systole) et de la relaxation (diastole) du myocarde, ces quatre valves auront pour fonction de s'ouvrir et se fermer cycliquement grâce aux variations de pression ainsi générées.

En particulier, la valve aortique permet le passage du sang chargé en oxygène vers l'aorte. Pendant la diastole et le début de la systole elle est fermée et pendant le reste de la systole elle est ouverte. La valve aortique se compose de trois « feuillets », composés à leur tour de trois couches cellulaires : la fibrosa, la spongiosa et la ventricularis.

I.II.II Une dégénérescence valvulaire très répandue

Le rétrécissement aortique calcifié (RAC) est une dégénérescence de la valve aortique qui consiste en une accumulation progressive de dépôts calcaires dans le tissu. Les facteurs qui favorisent l'apparition et le développement de cette pathologie sont l'âge, le cholestérol, le tabac et même des prédispositions génétiques, entre autres, et elle a pour effet une déficience de l'ouverture de la valve qui se traduit par des douleurs thoraciques et des essoufflements dans un premier temps et évolue vers l'insuffisance cardiaque et enfin la mort.

Le RAC atteint environ 3% des personnes âgées de plus de 65 ans et environ 12% des personnes âgées de plus de 75 ans. En Europe, on parle de 4,9 millions de patients dont 1,3 million souffre de sténose aortique sévère symptomatique : leur survie moyenne est de 2 à 5 ans.

Aujourd'hui, la principale réponse médicale à cette pathologie est de remplacer la valve native par une valve artificielle (biologique ou mécanique) via deux solutions : la chirurgie à cœur ouvert ou l'implantation de valve par voie percutanée (TAVI). Ces interventions, à risque élevé (3 à 10% de décès en cours d'intervention) s'accompagnent de plusieurs menaces du type AVC, arrêt cardiaque, morbidité ou infections entre autres. De plus, il reste un pourcentage de patients qui n'est pas éligible à la chirurgie.

I.II.III Une nouvelle approche médicale

Nous pouvons dire avec conviction qu'il existe un besoin médical non satisfait, et c'est à ce niveau-là que naît l'idée non pas de remplacer la valve aortique native, mais de la réparer à travers une technologie innovante : les PCUT. En effet, les ultrasons permettent de réaliser des interventions chirurgicales non-invasives très précises et moins coûteuses que les chirurgies conventionnelles, et les avantages sont considérables : réduction de certains risques liés à la chirurgie (infections, complications, morbidité), rentrée du patient chez-lui le jour même de la chirurgie, récupération post-opératoire plus facile, absence de cicatrices extérieures ou réduction de la morbidité, entre autres.

A ce jour, la société Cardiawave SAS développe un système innovant de thérapie ultrasonore pour réparer la valve aortique calcifiée, en partenariat avec Physique pour la médecine Paris et l'Hôpital Européen Georges Pompidou. L'objectif de la société est de développer un dispositif de thérapie guidée par échographie, appliquée au niveau du thorax du patient, qui permettra de casser mécaniquement les calcifications du RAC et ceci sans blesser les tissus sains, sans effets de chauffe et en ramollissant la valve aortique. Un premier prototype de thérapie guidée par échographie, le dispositif Valvosoft®, est en cours de développement et des essais de sécurité et d'efficacité ont été menés.

Tout d'abord, des essais précliniques de thérapie sur des valves biologiques calcifiées implantées ont été effectués sur 8 moutons et 7 porcs. La fonction aortique a été améliorée avec une diminution significative du gradient de pression de $21,1 \pm 4$ mmHg à $9,6 \pm 2$ mmHg et une ouverture plus large de la valve. En outre, les valves calcifiées ont été ramollies, leur rigidité ayant été évaluée par élastographie et montrant une diminution de $105,8 \pm 9$ kPa à $46,6 \pm 4$ kPa *in vitro* et de $82,6 \pm 9$ kPa à $41,8 \pm 7$ kPa *in vivo* [14].

Ensuite, des essais précliniques de thérapie chez 30 porcs sains ont été menés pour évaluer les effets de la cavitation sur les tissus cardiaques et les poumons, la réponse de la fonction cardiaque pendant et après la sonication et la taille possible des débris libérés. Nous avons trouvé que :

- Il n'y a pas de gros débris ;
- Il n'y a pas de perforation tissulaire ;
- Il n'y a aucun signe d'accident vasculaire cérébral, d'insuffisance cardiaque ou de régurgitation aortique.

I.III Le monitoring des PCUT : challenges et paradigmes actuels

Les thérapies par ultrasons cavitationnels pulsés (PCUT) sont des technologies prometteuses qui pourraient avoir un impact important sur le monde médical. Elles sont non invasives, très adaptables à de multiples pathologies sur différents organes du corps humain et représentent un risque moins élevé pour le patient par rapport aux standards chirurgicaux actuels.

Pour ce faire, un positionnement précis du point focal thérapeutique par rapport aux tissus anatomiques cibles et le suivi du nuage de cavitation pendant la procédure sont essentiels pour garantir la sécurité et l'efficacité de la procédure. Comme les médecins ne disposent pas d'un retour visuel direct du nuage de bulles, une modalité d'imagerie pratique, non invasive et en temps réel serait idéale pour guider et surveiller la thérapie.

À ce jour, les PCUT sont généralement guidées et surveillées par l'échographie en mode B, qui est une modalité d'imagerie en temps réel non invasive permettant de visualiser le nuage de cavitation en relation avec l'anatomie du patient. Le nuage de bulles étant très échogène, le contraste de l'imagerie est généralement suffisant pour permettre une visualisation correcte de la dynamique des nuages. Néanmoins, dans les organes profonds ou en mouvement, les performances d'imagerie diminuent et le contraste n'est pas suffisant pour permettre une différenciation objective entre le nuage de bulles et les tissus, ce qui compromet la surveillance de la procédure.

En outre, l'imagerie classique en mode B permet d'imager un plan bidimensionnel. Cependant, le transducteur thérapeutique et la sonde d'imagerie sont dans la plupart des cas des dispositifs indépendants, et le potentiel défaut d'alignement mécanique entre les deux

transducteurs pourrait faire sortir le nuage de cavitation du plan d'imagerie, qui serait « invisible » pour le médecin, ce qui constitue un risque pour la sécurité et l'efficacité de la procédure. De plus, dans les milieux hétérogènes tels que les côtes, le crâne ou les tissus adipeux (c.f. *in vivo*), les ultrasons peuvent être aberrés et le point focal pourrait également être déplacé en dehors du plan d'imagerie. Comme la cavitation est un phénomène tridimensionnel et que sa position peut être hors du plan soit par un désalignement mécanique soit par une aberration acoustique, une technique d'imagerie tridimensionnelle adaptée serait idéale pour une surveillance complète de la procédure.

Du fait que les PCUT se rapprochent rapidement de la clinique, à mesure que nous nous rapprochons du patient nous devons garantir une procédure extrêmement sûre, pour ne pas mettre la vie du patient en danger et en assurer l'efficacité maximale.

L'objectif de cette thèse était de développer des modalités d'imagerie adaptées au guidage et à la surveillance des PCUT, en particulier pour les applications cardiaques et en particulier pour le traitement de la sténose aortique calcifiée développé par Cardiawave, Physique pour la médecine Paris et l'Hôpital Européen Georges Pompidou. Nous avons divisé ce travail en trois parties principales : une première partie concernant le développement de modalités d'imagerie par cavitation ainsi qu'une réflexion globale sur les limites des techniques actuellement disponibles, une seconde partie sur l'évaluation de la forme, de la position et de la dynamique de la cavitation sur la thérapie développée par Cardiawave et une troisième partie concernant le développement d'un nouveau transducteur et la mise en place de l'imagerie par cavitation pour la thrombotripsie.

II Une nouvelle modalité d'imagerie de cavitation : de la 2D à la 3D

II.I Imagerie de cavitation : bref état de l'art

Différentes méthodes de cartographie de l'activité de cavitation ont fait l'objet de recherches au cours de la dernière décennie et plusieurs approches ont été proposées. Des méthodes d'imagerie par échographie conventionnelle ou par échographie « ultrarapide » ont été développées en augmentant la sensibilité et la spécificité des ultrasons aux échos de bulles de cavitation, sur la base du comportement non linéaire ou spatio-temporel des bulles de cavitation. Ces méthodes permettent d'augmenter le contraste des cartes de cavitation par rapport à l'imagerie conventionnelle en mode B, mais les cartes de cavitation apparaissent très

bruitées par les échos des diffuseurs dans des tissus qu'il est difficile d'annuler complètement, en particulier lorsque ceux-ci se déplacent rapidement.

D'autres approches s'appuient sur des méthodes d'imagerie dites « passives », basées sur l'enregistrement des échos rétrodiffusés du faisceau thérapeutique par une sonde d'imagerie. Dans la plupart des cas, ces méthodes ont été développées afin de localiser l'activité de la cavitation dans le cadre des thérapies à effet de chauffe (HIFU), caractérisées par l'émission de signaux continus ou de rafales longues. Cependant, avec ce type d'émission continue ou pseudo-continue, la formation de l'image doit être réalisée sans connaître les délais absolus entre l'émission de l'onde ultrasonore et la réception de ses échos sur la sonde d'imagerie, ce qui entraîne une formation de faisceau sous-optimale avec une faible résolution axiale. De plus, ces méthodes sont basées sur l'estimation de l'intensité de la rétrodiffusion qui est moyennée de manière incohérente sur chaque pixel de l'image pendant l'émission, ainsi, l'intensité rétrodiffusée n'est pas spécifique aux bulles de cavitation car elle est également associée aux réflexions des diffuseurs dans le milieu qui ne peuvent être discriminées que par les amplitudes relatives de l'écho. En conséquence, ces méthodes sont bien adaptées au contrôle de la cavitation dans des tissus statiques et homogènes, mais elles restent limitées pour localiser la cavitation en temps réel dans des tissus hétérogènes et en mouvement.

II.II Imagerie passive cohérente : théorie

II.II.I Acquisition cohérente et formation de l'image

Nous avons mis en place une modalité d'imagerie de cavitation basée sur une acquisition passive des échos thérapeutiques rétrodiffusés, où nous profitons en plus du fait que les rafales des PCUT sont très courtes et nous pouvons de ce fait mesurer très précisément le temps de propagation et de rétrodiffusion des ondes émises. Ainsi, nous pouvons former une image en « pulse-écho » cohérente avec une bonne résolution axiale basée sur la réception par la sonde d'imagerie des échos rétrodiffusés provenant des émissions thérapeutiques :

- Lorsque la cavitation n'est pas encore nucléée, l'image passive montrera le faisceau de l'émission thérapeutique ;
- Lorsque la cavitation est nucléée, les bulles étant des réflecteurs non-linéaires très échogènes, le nuage sera imagé avec un contraste élevé ;

- Néanmoins, pour supprimer tout bruit potentiel et du fait que le nuage de cavitation présente un comportement spatio-temporel différent de celui des tissus, la combinaison de l'imagerie passive cohérente avec un filtre spatio-temporel permettra d'augmenter le contraste du nuage de cavitation.

Les deux appareils sont ainsi synchronisés. De plus, une imagerie échographique anatomique en mode B peut être réalisée entre les impulsions de thérapie, et la « carte de cavitation » peut être superposée sur cette image pour pouvoir visualiser le nuage de cavitation vis-à-vis des tissus cibles.

Il est à noter que nous supposons que la sonde est dans une position fixe par rapport au transducteur, et que le retard ultrasonore δt entre la sonde d'imagerie et le transducteur thérapeutique, à inclure dans l'algorithme de formation de l'image, a été mesuré au préalable. Il est également à noter que la résolution axiale dépendra de la longueur de la rafale thérapeutique : plus la rafale est courte, meilleure est la résolution axiale.

Enfin, comme le signal ultrasonore rétrodiffusé par cavitation inertielle est large bande, il n'est pas nécessaire de choisir une sonde d'imagerie ayant une fréquence centrale spécifique, et il est donc possible d'utiliser les sondes cardiaques conventionnelles du marché.

II.II.II Filtrage spatiotemporel : la décomposition en valeurs singulières

Grâce à l'imagerie passive cohérente, le nuage de cavitation est formé avec un contraste élevé. Cependant, en fonction du milieu sonifié et notamment des tissus très échogènes et des interfaces, il peut rester du bruit pouvant conduire à des ambiguïtés quant à l'interprétation de la position, de la forme et de la taille du nuage de bulles. Or, les bulles de cavitation présentent un comportement spatio-temporel différent de celui des tissus : d'une part elles sont très échogènes, et d'autre part leur dynamique est rapide, chaotique et non linéaire par rapport à celle des tissus biologiques. Il est ainsi possible de combiner les acquisitions d'images passives avec un filtrage spatio-temporel permettant de supprimer un maximum de bruit possible et d'augmenter d'avantage le contraste du nuage de cavitation.

Une méthode de filtrage spatiotemporelle utilisant une décomposition en valeurs singulières (SVD) d'images « ultrarapides » a été introduite et appliquée à l'imagerie du flux sanguin dans un premier temps, et adaptée par la suite à l'imagerie de cavitation active dans les organes en mouvement. En effet, il a été démontré que les vecteurs singuliers les plus élevés

correspondent au signal provenant des tissus, tandis que le sang, le bruit et d'autres signaux incohérents spatio-temporellement se situent dans les faibles valeurs singulières, et en particulier il s'avère que les signaux des nuages de bulles sont extrêmement incohérents. Cette méthode dépend toutefois fortement de la fréquence d'images et est moins efficace dans les organes en mouvement où le signal des tissus est également présent dans les faibles valeurs singulières, et se présente ainsi comme du bruit.

Maintenant, l'imagerie passive ne reconstruit que les échos provenant du signal thérapeutique, qui est focalisé, et a par définition moins de sources de bruit. Par conséquent, nous nous attendons à ce que le filtrage SVD soit plus efficace dans les tissus en mouvement. Le défi du filtrage restera le choix des bons vecteurs singuliers associés.

II.III Méthodes et preuves de concept

II.III.1 Filtrage spatiotemporel : la décomposition en valeurs singulières

Nous avons conçu un montage expérimental spécifique pour prouver la faisabilité et l'efficacité de la méthode d'acquisition passive cohérente pour imager la cavitation lors des PCUT. Nous avons utilisé un transducteur de thérapie focalisé à 1 MHz ($f = 100$ mm, $f / D = 1$), (Imasonic ©, France) pour les émissions ultrasonores de haute intensité, actionné par un amplificateur de puissance de 2,5 kW (RITEC ©, USA). Une sonde d'imagerie cardiaque (64 éléments, P4-2, Philips ©, USA) a été insérée dans le trou central du transducteur et les deux ont été fixées à l'aide d'un support imprimé en 3D spécialement conçu. La sonde d'imagerie était connectée à un scanner ultrasonore programmable (Vantage 256, Verasonics ©, USA). Le signal de commande du transducteur de thérapie était émis par un générateur de fonctions et consistait en une onde sinusoïdale de 8 cycles à 1 MHz avec une fréquence de répétition des rafales (PRF, *pulse repetition frequency* en anglais) de 100 Hz (rapport cyclique de 0,08%). Le générateur de fonctions avait également un rôle d'horloge pour synchroniser l'entrée du scanner d'imagerie et l'amplificateur.

Le transducteur a été préalablement calibré à l'aide d'un interféromètre optique hétérodyne dans l'eau [16]. La pression acoustique négative maximale a été estimée entre -8 MPa et -9 MPa *in vitro*.

Pour la première validation *in vitro* de notre méthode, nous avons préparé un gel mimant les tissus en mélangeant 1 litre d'eau et 8% d'alcool polyvinylique (PVA, Sigma-Aldrich

Chemistry ©, St-Louis, MO, USA). Nous avons rajouté diffuseurs d'ultrasons en utilisant 1% de particules de cellulose de 20 µm de diamètre (Sigmacell cellulose, Sigma-Aldrich Chemistry ©, St-Louis, MO, USA). La sonde et le transducteur ont été fixés à un moteur à deux axes (PI, Micos, Eschbach, Allemagne) et placés à l'intérieur d'un aquarium rempli d'eau dégazée de telle sorte à générer le nuage de cavitation à l'intérieur du gel en PVA. Nous avons programmé une vitesse de déplacement maximale des moteurs d'environ 10 mm/s pour les directions axiale et latérale des moteurs. Les mouvements axiaux et latéraux ont été induits en même temps et avec la même vitesse.

II.III.II Séquence d'imagerie et filtrage

Considérons un ensemble de n_t images passives de dimensions n_x et n_z , où n_x et n_z sont respectivement le nombre d'échantillons spatiaux dans les directions x et z. L'ensemble peut être réorganisé dans une matrice matricielle bidimensionnelle $X(n_x \times n_z, n_t)$, la matrice de Casorati. La décomposition en valeurs singulières (SVD) de cette matrice consistera à trouver les vecteurs singuliers temporels et spatiaux, respectivement regroupés dans les colonnes de deux matrices U et V, et les valeurs singulières σ_i associées disposées de la plus énergétique à la moins énergétique.

À la suite de la décomposition en valeurs singulières (SVD) de la matrice X, il s'agira de reconstruire la carte de cavitation en utilisant uniquement les vecteurs singuliers associés au nuage de bulles. En supposant que les bulles sont contenues dans un ensemble contigu de vecteurs singuliers, le but sera de définir les deux valeurs singulières limites p et q pour ne retenir que le signal spécifique aux bulles $X_{bubbles}$:

$$X_{bubbles}(n_x \times n_z, n_t) = \sum_{i=p}^q \sigma_i U_i V_i^T \quad ()$$

Cette nouvelle matrice peut être réorganisée sous une forme matricielle tridimensionnelle $X_{bubbles}(n_x, n_z, n_t)$, et nous pourrons ensuite calculer son intégrale de puissance, destinée à cartographier les zones les plus énergétiques de l'image, pour arriver ainsi à la carte de cavitation (CM) :

$$CM(n_x, n_z) = \int |X_{bubbles}(n_x, n_z, n_t)|^2 dt \quad ()$$

Ainsi, n_t images nous donneront une carte de cavitation, de telle sorte que les cartes de cavitation auront une fréquence d'image divisée par n_t par rapport à la cadence d'acquisition d'images passives (dans notre cas, $100/n_t$ Hz). En fonction des applications, il est important d'optimiser le nombre de trames n_t à utiliser.

La carte de cavitation pourra alors être superposée au mode B dans une échelle de couleurs différente et en temps réel, ce qui nous conduit à une séquence hybride complète de surveillance des PCUT.

Cette méthode a été brevetée sous le numéro suivant :

- PCT / EP2019 / 063455

Et publiée :

- Daniel Suarez Escudero, Guillaume Goudot, Michael Vion, Mickael Tanter, and Mathieu Pernot. "2D and 3D Real-Time Passive Cavitation Imaging of Pulsed Cavitation Ultrasound Therapy in Moving Tissues." *Physics in Medicine & Biology* 63, no. 23 (December 6, 2018): 235028.

II.III.III Résultats in vitro

Pour évaluer la faisabilité et l'efficacité de notre méthode, nous avons comparé le rapport contraste-sur-bruit (CNR, *contrast-to-noise ratio* en anglais) des cartes de cavitation acquises avec notre méthode passive et celles acquises avec l'imagerie « ultrarapide » pendant cavitation sur le gel en PVA, sur des conditions statiques et en mouvement. Nous avons en plus programmé différentes séquences actives ayant différents compromis entre vitesse d'acquisition et qualité d'image.

Nous avons d'abord évalué le CNR lorsque le gel était dans un état statique. Nous avons fixé n_t égal à 6, 10 et 14 et nous avons étudié l'évolution du CNR suivant différentes valeurs de p et q .

- Nous avons observé que le CNR est maximal lorsque $p = 2$ et $q = n_t$ autour de 18 pour les séquences actives et autour de 15 pour la séquence passive ;

Résumé en français

- Nous avons remarqué que le bruit à basse fréquence spatio-temporelle (à savoir, les tissus) est généralement condensé dans le premier vecteur singulier, et que les fréquences spatio-temporelles élevées correspondant au nuage de bulles sont condensées dans les vecteurs singuliers restants ;
- Nous avons également comparé l'influence de n_t sur le CNR lorsque $p = 2$ et $q = n_t$ et nous avons observé que la courbe suit une évolution logarithmique et atteint un plateau autour de 18 pour les séquences actives et autour de 16 pour la séquence passive globalement après $n_t = 20$. Les valeurs p et q doivent être soigneusement choisies pour obtenir de bonnes performances de filtrage en perdant le moins d'information de cavitation possible.

Deuxièmement, en considérant le cas où les moteurs sont constamment en mouvement, nous avons fixé n_t à 6, 10 et 14, $p = 2$ et $q = n_t$, nous avons appliqué le filtre SVD et nous avons calculé le CNR sur les cartes de cavitation pour les différentes séquences d'imagerie. Nous avons observé une diminution importante de CNR, inférieur à 3 pour toutes les séquences actives. En revanche, le CNR est resté proche de sa valeur en condition statique pour la séquence passive. Avec le mouvement, le CNR pour les acquisitions passives apparaît nettement plus élevé (10 vs 1) que le CNR calculé pour toutes les séquences actives.

II.III.IV Analyse des résultats in vitro

En utilisant l'imagerie active ultrarapide de cavitation, le filtrage SVD n'est pas aussi efficace dans la condition en mouvement que dans la condition statique. Nous avons observé que le signal des tissus est inévitablement distribué sur tous les vecteurs singuliers, que cette distribution évolue dans le temps et que fatalement il n'est pas possible de fixer des valeurs de p et q . L'imagerie de cavitation active en mouvement nécessite de calcul constant de p et q , ce qui n'est pas encore optimal en temps réel. De plus, même lors de la mise à jour des valeurs p et q , la carte de cavitation active CNR diminue considérablement par rapport aux applications statiques.

L'imagerie passive présente l'avantage de bénéficier d'une spécificité spatiale accrue, en effet le champ traité est réduit et les échos rétrodiffusés proviennent uniquement de l'émission thérapeutique focalisée. Pour les deux conditions statiques et en mouvement, les basses fréquences spatiotemporelles représentant la contribution du tissu sont compactées dans le premier vecteur singulier, et la contribution de l'activité du nuage de bulles est

approximativement répartie dans les vecteurs singuliers restants (2 à n_t). Cette distribution est par ailleurs constante dans le temps, ce qui rend plus fiable la fixation des valeurs p et q pour toute une session de thérapie et permettant une surveillance de la cavitation en temps réel.

II.III.V Expérience in vivo

Suite à la validation *in vitro* de la méthode, nous avons mené des expériences *in vivo* sur le foie de trois porcs. L'étude a été approuvée par le comité d'éthique local (école de médecine vétérinaire de Maison Alfort, France). Trois jeunes porcs en bonne santé de 25 kg ont été utilisés. Les animaux ont été complètement anesthésiés avec de l'isoflurane, intubés et placés sur une table chirurgicale en décubitus dorsal, puis maintenus sous anesthésie par inhalation d'isoflurane (2,5%) pendant toute la durée de la procédure. Chaque animal a été contrôlé par un oxymètre de pouls et un moniteur d'électrocardiogramme. La vitesse maximale estimée du mouvement du foie était de 8 mm/s.

Les mêmes transducteurs et la même séquence d'imagerie que pour les expériences *in vitro* ont été utilisés. Les transducteurs ont été attachés à un bras flexible chirurgical et mis en contact avec la peau des animaux à l'aide d'une membrane en latex. Le système a été positionné pour cibler le parenchyme hépatique et la PCUT a été appliqué par voie transcutanée pendant 3 minutes dans une position fixe, sous ventilation normale de l'animal. Pour les expériences *in vivo*, les paramètres du filtre SVD ont été fixés à $n_t = 10$, $p = 2$ et $q = n_t$.

Nous avons appliqué le filtre SVD pour des acquisitions actives et passives pendant la cavitation, et nous avons calculé le CNR moyen sur les cartes de cavitation obtenues pour chaque porc. Avec l'acquisition de 300 images actives et passives, nous avons obtenu 30 cartes de cavitation. Nous avons observé que le CNR calculé pour les acquisitions passives était significativement supérieur au CNR calculé par les acquisitions actives pour tous les animaux (CNR moyen de $6,7 \pm 0,9$ par rapport à $1,9 \pm 1,0$, $p < 0,05$).

En utilisant la séquence de surveillance complète, il a été possible d'acquérir simultanément des images actives et passives, puis de superposer en temps réel les cartes de cavitation passives sur les images échographique en mode B, ce qui nous a permis de localiser précisément le nuage de bulles dans les structures anatomiques hépatiques et de suivre l'évolution de la forme et de la taille du nuage de bulles.

II.IV Vers l'imagerie de cavitation 3D

II.IV.I Intérêt et défis de l'imagerie 3D

Pour dépasser les limitations mécaniques et acoustiques de l'imagerie bidimensionnelle, nous avons ensuite étendu la modalité à l'imagerie 3D. Le principe et les synchronisations restent comparable à la 2D, ainsi que le rapport contraste sur bruit de la carte de cavitation 3D résultante. L'imagerie 3D permet de surveiller tout un volume sonifié et d'évaluer la forme et la position du nuage de bulles dans son ensemble, et donc la totalité effective de la zone traitée. Le nuage peut être en effet asymétrique et, dans des cas extrêmes, des nuages secondaires peuvent être nucléés hors-centre, et ainsi un seul plan d'imagerie donnera dans ces cas des informations incomplètes. Cependant, l'imagerie 3D reste coûteuse et la qualité de l'image peut ne pas être suffisante pour notre application.

II.IV.II Preuve de concept et résultats

Nous avons dans un premier temps prouvé la faisabilité de l'imagerie passive cohérente de cavitation en 3D, en utilisant le même montage expérimental que précédemment, mais en remplaçant la sonde d'imagerie par une sonde matricielle 32x32 centrée à 3 MHz (Vermon®, France) couplée à un système d'imagerie programmable basé sur 4 systèmes Vantage synchronisés.

Nous avons calculé le CNR pour différentes combinaisons des paramètres n_t , p et q lors d'expériences statiques et en mouvement. Nous avons acquis 200 volumes pour chaque séquence, et nous avons appliqué le filtre SVD en post-traitement. Le nuage de bulles a été imaginé avec succès en 3D *in vitro*. Le CNR était légèrement plus faible en 3D qu'en 2D (11 vs 15), ce qui peut s'expliquer par la plus petite ouverture de la sonde matricielle. Nous avons observé que le CNR est maximal approximativement lorsque $p = 3$ et $q = n_t$. Par rapport aux résultats 2D, la dépendance avec p était cependant moins marquée. Nous avons également comparé l'influence de n_t lorsque $p = 2$ et $q = n_t$ et nous avons observé que la courbe suit une évolution logarithmique et atteint un plateau globalement après $n_t = 15$ volumes. De plus, contrairement aux résultats 2D, il n'y avait pas de diminution significative du CNR entre les expériences statiques et en mouvement en 3D. Ce résultat met en évidence la robustesse de l'imagerie 3D par rapport à l'imagerie 2D qui subit un effet de décorrélation dans la direction d'élévation.

Le comportement de la modalité d'imagerie reste très comparable à la 2D, et les performances du filtrage SVD permettent de calculer une carte de cavitation volumétrique débruitée (sans contributions du tissu).

II.V Vers l'imagerie de cavitation bi-plane : un compromis entre la 2D et la 3D

II.V.I Intérêt et défis de l'imagerie bi-plane

Un bon compromis entre l'échographie en mode B et l'imagerie 3D peut être une modalité d'imagerie bi-plane. Cette modalité consiste à utiliser une sonde ayant deux réseaux piézoélectriques orthogonaux dans le but d'imager successivement deux plans orthogonaux X et Y. Elle permet de surveiller une grande partie du volume sonifié, et reste peu coûteuse et facilement implémentable par rapport à l'imagerie 3D. De plus, la qualité d'image reste similaire à la qualité de l'échographie conventionnelle.

Il est à noter que le principal inconvénient de cette technique est la perte de la cadence d'image, divisée par deux par rapport à l'imagerie conventionnelle (car nous devons former deux plans).

II.V.II Conception et fabrication d'une sonde bi-plane cardiaque

Nous avons conçu et fabriqué une sonde bi-plane clinique centrée à 2.8 MHz basé sur la sonde PAXY (Vermon©, France), adaptée à la cardiologie et au dispositif Cardiawave, et nous avons développé (grâce aux travaux de Jingjing Xia) une lentille sphérique permettant d'aboutir à une focalisation en élévation pour les deux réseaux. Cette lentille étant en silicone et ayant une courbure sur les plans de l'image, induit toutefois d'une correction de l'algorithme de formation de l'image. Le résultat est une diminution considérable de la cadence d'images, autour de 7 images par seconde.

Nous avons mis en place une technique de formation de l'image basée sur une approximation à lentille mince, permettant d'alléger la correction de l'algorithme de formation de l'image malgré une perte en résolution latérale pour parvenir à un bon compromis entre qualité d'image et cadence d'image, autour de 20 images par seconde. Cette approximation consiste en supposer que la lentille a une épaisseur constante devant chaque élément piézoélectrique, et nous nous sommes basés sur le fait que l'épaisseur de la lentille (épaisseur maximale $h = 0,6$ mm) est en moyenne faible par rapport à la longueur d'onde ultrasonore.

II.V.III Évaluation de la sonde bi-plane

Nous avons testé les capacités et les performances de la sonde bi-plane en mode B et en imagerie de cavitation passive cohérente.

Concernant l'approximation en lentille mince, nous avons trouvé une perte maximale de contraste de 2.4 dB et une perte maximale de résolution latérale de 0.8 mm. De plus, la perte de résolution diminue avec la profondeur et est quasiment nulle sur champ lointain. En effet, la correction de lentille mince induit généralement des erreurs dans le champ proche mais a très peu d'effet dans le champ lointain. L'acceptabilité ou non des erreurs présentées précédemment dépendra d'une évaluation clinique.

Concernant la sonde PAXY en elle-même, nous avons trouvé une perte maximale de résolution latérale de 2 mm par rapport à la sonde P4-2 (l'erreur augmente avec la profondeur). Comme prévu, la sonde latérale PAXY a une perte légère de résolution latérale en raison de nos hypothèses de formation de faisceau, des différences de conception et du fait que notre sonde n'est pas encore totalement optimisée.

Enfin, nous avons évalué notre modalité d'imagerie passive de cavitation sur gel en PVA et nous avons trouvé des résultats très similaires à ceux trouvés en 2D, avec une très légère perte en CNR par rapport à la sonde P4-2 (16 vs 15). Il est à noter qu'il existe une légère différence de CNR entre les plans X et Y de la sonde PAXY, qui peut résulter de la conception mécanique de la sonde.

III Conception d'un nouveau transducteur de thérapie pour la thrombotripsie

III.I La thrombose veineuse profonde

La thrombose veineuse profonde se produit lorsqu'un thrombus (ou un caillot de sang) se forme le long d'une veine, généralement au niveau des jambes du patient. Il peut être non occlusif et même asymptomatique lorsque le sang coule toujours dans la veine, ou occlusif lorsque le thrombus bloque le flux sanguin. Des douleurs à la jambe ou des gonflements peuvent survenir, et le principal danger pouvant avoir lieu est la rupture ou le détachement du thrombus (ou d'un morceau de thrombus), qui pourra se loger au niveau des poumons et provoquant une embolie pulmonaire.

Les principales solutions sont les anticoagulants, les thrombolytiques ou les bas de compression. Ces techniques réduisent la capacité de coagulation du sang, aident à réduire le caillot ou empêchent le gonflement des jambes, mais leur efficacité est généralement difficile à atteindre, en particulier pour les thrombus de grande taille.

Lorsque le thrombus est très volumineux, il existe d'autres solutions invasives, telles que la thrombectomie, consistant à retirer le caillot de l'intérieur de la veine par une intervention chirurgicale. Néanmoins, les thrombectomies présentent des risques tels que des infections, des saignements excessifs, des lésions veineuses ou une embolie pulmonaire en cas d'échec.

Le traitement de la thrombose veineuse par PCUT, la thrombotripsie, est présenté comme une solution alternative non invasive qui permettrait de liquéfier mécaniquement le thrombus dans le but de créer un canal pour rétablir le flux sanguin, sans relargages importants de débris et en évitant les risques de la chirurgie.

III.II La thrombotripsie et l'approche de Physique pour la Médecine

Depuis 2009, le département de génie biomédical de l'Université du Michigan explore des procédures de thrombotripsie non invasives basées sur PCUT, permettant de recanaliser avec succès les modèles de veine thrombotique et montrant des résultats prometteurs.

En parallèle, Physique pour la Médecine Paris, en partenariat avec l'Hôpital Européen Georges Pompidou et Cardiawave SA, explore une approche robotisée du traitement de la thrombose veineuse profonde par thrombotripsie. Son efficacité a été prouvée sur un modèle porcine en utilisant un bras robotique à 6 axes pour déplacer automatiquement le transducteur le long de la trajectoire du thrombus. La procédure est guidée par échographie et les positions des cibles le long du thrombus sont déterminées manuellement, la cavitation étant centrée sur la veine afin d'éviter d'endommager ses parois. Cette approche est basée sur un transducteur mono-élément à 2,25 MHz (Imasonic ©, France) pour les émissions thérapeutiques et une sonde linéaire (SL10-2, SuperSonic Imagine ©) pour l'imagerie. Une deuxième étude *in vivo* utilisant un modèle porcine est en cours.

Cependant, d'importants problèmes subsistent car la position du point focal géométrique intrinsèque à un mono-élément limite la zone thérapeutique et il est difficile d'atteindre les thrombus en dehors de cette zone. La position du nuage de cavitation doit être soigneusement placée pour permettre la création d'un seul canal traversant l'ensemble du thrombus, permettant

ainsi l'efficacité du traitement et ne détruisant pas les cellules saines le long des parois veineuses.

Nous proposons la conception d'un nouveau transducteur thérapeutique adapté à cette pathologie et permettant de focaliser les ultrasons thérapeutiques à différentes profondeurs sur l'axe central du transducteur. De plus, nous voulions optimiser la fréquence centrale pour traiter une zone plus grande et améliorer l'efficacité de la procédure.

De plus, nous avons intégré dans le système l'imagerie de cavitation passive et conçu une interface homme-machine (IHM) spécifique permettant de contrôler facilement le bras robotique et d'obtenir les paramètres de déplacement et de vitesse. Ces paramètres sont utiles pour calculer la dose de cavitation nécessaire à une désintégration efficace des thrombus. D'autres améliorations doivent être apportées.

III.III Conception d'un nouveau transducteur de thérapie

Une étude préliminaire menée auprès de 30 patients à l'Hôpital Européen Georges Pompidou par le Dr. Lina Khider a montré que la position haute moyenne du thrombus était à $2,09 \pm 0,7$ cm et la position basse moyenne du thrombus était de $4,84 \pm 1,12$ cm de la peau. Ainsi, le dispositif de thrombotripsie idéal devrait pouvoir atteindre une profondeur cible comprise entre 2 et 6 cm sous la peau. Par ailleurs, par des raisons de sécurité, nous voulions créer un nuage de cavitation de diamètre maximal inférieur à 10 mm.

Nous proposons la conception d'un transducteur multi-éléments annulaire de forme sphérique permettant une focalisation électronique et géométrique des ultrasons le long de son axe central. Les transducteurs annulaires minimisent le niveau des lobes secondaires avec un petit nombre de éléments. L'idée à plus long terme était d'assurer la compatibilité du transducteur avec le dispositif Cardiawave, de sorte que la procédure soit facilement transposable en clinique.

Le nouveau transducteur doit comporter en plus un trou central pour le positionnement de la sonde. En pratique, le rayon sphérique du transducteur, qui définit la largeur du transducteur ainsi que sa focale naturelle, et le diamètre du trou central, étaient les deux paramètres critiques à optimiser car ils définissent la taille des éléments piézoélectriques et la plage de focalisation. En effet, plus les éléments sont larges, plus ils sont plus directifs, ce qui détériore les capacités de focalisation.

La conception a été optimisée à l'aide de simulations 3D, nous avons simulé différentes configurations de transducteurs adaptés à nos besoins jusqu'à aboutir à une solution nous permettant de focaliser dans les plages de profondeur souhaitées pour l'application. Nous avons choisi une fréquence d'émission centrale de 1.6 MHz ($\lambda = 0,96$ mm) et dans nos simulations nous avons trouvé une longueur maximale de tâche focal de 6,67 mm à -3 dB à une profondeur de 6 cm sous la peau : il s'agit de la taille maximale du point focal accessible. De plus, nous avons gagné 17% en surface active.

IV Conclusion

Premièrement, une nouvelle modalité d'imagerie du nuage de cavitation basée sur une acquisition ultrasonore passive cohérente et associée à un filtre spatio-temporel a été développée, adaptée aux applications cardiaques et facilement transposable aux appareils à ultrasons du commerce. La modalité tire parti des impulsions courtes de la PCUT et, en connaissant les retards absolus entre l'émission thérapeutique et la réception des échos par la sonde, elle permet de créer une image cohérente en « pulse-écho » du champ ultrasonore thérapeutique. La modalité a d'abord été testée en 2D, *in vitro* et *in vivo*, puis transposée en 3D.

Deuxièmement, nous avons développé des outils de sécurité pour assurer le guidage et la surveillance de la thérapie. La cavitation étant un phénomène tridimensionnel, il était nécessaire, en fonction de la conception du dispositif Cardiwave, d'assurer le positionnement précis du point focal thérapeutique. Une nouvelle sonde cardiaque a été conçue pour le projet. Des acquisitions ultra-rapides bi-planes en mode B ont été développées et testées, puis associées à l'imagerie de cavitation. Une modalité de formation d'image spécifique permettant une cadence d'image suffisante pour la surveillance et adaptée aux spécifications mécaniques de la sonde a également été mise au point sur la base de théories physiques et de simulations.

Simultanément, la PCUT est présentée comme une solution potentielle pour traiter la thrombose veineuse profonde en créant un canal pour permettre le passage du sang à travers le thrombus, en utilisant la cavitation inertielle. Nous avons proposé la conception d'un nouveau transducteur de thérapie adapté à cette pathologie et permettant de focaliser des ultrasons de haute intensité à différentes profondeurs. La conception a été optimisée à l'aide de simulations. Enfin, nous avons couplé l'ensemble du système PCUT, assisté par robot, à l'imagerie de cavitation pour permettre de positionner facilement la cible, et aboutir à un dispositif transposable en clinique.

Résumé en français

Nous pouvons conclure que le résultat de cette thèse est le développement d'une gamme de modalités permettant de mieux guider et contrôler les PCUT, ainsi qu'une réflexion globale sur les besoins et les limites de la procédure. L'utilisation effective ou non de nos modalités dépendra des contraintes de chaque dispositif, ainsi que des tissus cibles et des exigences et limites spécifiques de chaque pathologie. Il reste encore beaucoup de travail à faire pour développer et améliorer les modalités de surveillance et de guidage des PCUT, et des normes internationales doivent être élaborées afin d'homogénéiser l'ingénierie et les tests de la thérapie

General introduction

Histotripsy is a non-invasive pulsed cavitation ultrasound therapeutic (PCUT) approach that relies on the non-thermal mechanical effects generated by inertial cavitation bubbles in a controlled focal area. It is characterized by a short-pulsed highly intense focused ultrasound emission that will induce the nucleation of the cavitation bubbles, that together will join in a dense and energetic cavitation cloud. Developed in the 2000's, histotripsy may be effective in several medical indications such as tumour liquefaction or blood clots recanalization, but still remains very recent and there is a need to develop imaging modalities for the guiding and the monitoring of the procedure, and to ensure its maximal safety. Furthermore, at this date, there are no international standards for the technology.

In particular, histotripsy has been proved to be an effective solution for the calcified aortic stenosis (CAS) treatment. In fact, the calcifications in the valve leaflets can be mechanically broken by the effects of cavitation without damaging the healthy tissues, this softening the valve and restoring a more physiological cardiac function. No surgery is required, and this solution may be presented as an alternative and a complementary solution to heavy procedures such as open-heart surgery or the transcatheter aortic valve replacement (TAVR), which are today's gold standards.

Usually guided by conventional B-Mode ultrasound, histotripsy devices include a therapy transducer, that will focus ultrasound at the target zone, and an imaging probe, that will image both the sonicated tissues and the cavitation bubble cloud. However, the ultrasound imaging contrast is often limited in deep or moving organs such as the liver or the heart, and the visualization of the bubble cloud results qualitative and subjective for the operator. Moreover, B-Mode imaging allows to visualize the tissues inside an imaging plane, but on the one hand inertial cavitation is a three-dimensional phenomenon, and on the other hand it imposes the bubble cloud to be located inside the imaging plane, which cannot be completely ensured as there are uncontrolled variables such as ultrasound aberration or mechanical misalignments that may drive the therapeutic focal spot outside the imaging plane. This awakens the need for a three-dimensional imaging tool development, as for safety reasons it is essential to be able to precisely place the therapeutic focal spot on the target zone and to visualize the bubble cloud during the whole procedure.

General introduction

The present work explores different tools for the guidance and monitoring of the histotripsy treatment of CAS developed by Cardiawave SA, in partnership with Physics for Medicine Paris and the European Hospital Georges Pompidou. We divided the work in three principal parts.

First, a new modality for the cavitation cloud imaging based on a passive acquisition and combined with a spatiotemporal filter was developed, adapted to cardiac applications and easily transposable to commercial ultrasound devices. The modality takes advantage of the short-pulses of histotripsy, and by knowing the absolute time delays it allows a “pulse-echo” coherent beamforming of the therapeutic ultrasonic field. The modality was first tested in 2D imaging, *in vitro* and *in vivo*, then transposed to 3D imaging and tested *in vitro*. Nevertheless, as 3D imaging remains expensive and requires heavy electronics, we designed a bi-plane cardiac probe for the project, which results in a good compromise between 2D and 3D modalities in terms of cost and monitored area. We developed and tested conventional B-Mode, ultrafast and passive cavitation bi-plane imaging. We also set up a thin lens approximation-based beamforming allowing to improve the frame rate despite a slight loss in image quality.

Secondly, following Cardiawave’s device current design, we evaluated the therapeutic focal spot dimensions and behaviour in the whole therapeutic steering range in simulations at low pressures, and we evaluated the bubble cloud dimensions, behaviour and dynamics at high pressures *in vitro* while sonication through a tissue mimicking phantoms. Next, aiming to ensure the safe and precise guiding and monitoring of each procedure, as cavitation is a three-dimensional phenomenon and both the imaging probe and the therapeutic transducer may suffer mechanical misalignments, we developed specific tools to check the position of the therapeutic focal spot in relation to the imaging plane before each therapeutic trial.

Thirdly, histotripsy has been presented as a potential solution to treat venous thrombosis by liquefying the thrombus and creating a channel for blood flow. We propose the design of a new therapy transducer adapted to this pathology and allowing to focus high intensity ultrasound at different depths. Finally, we integrated the whole robotically assisted PCUT system for this therapy allowing coherent passive cavitation monitoring and an easy positioning of the target, hopefully easily transposable to clinics.

Chapter I - State of art

1.1 The physics of pulsed cavitation ultrasound therapies

1.1.1 Ultrasound physics

Sound is a longitudinal mechanical wave that produces a displacement of particles, in a series of successive compressions and rarefactions. The sound audible by the man is between 20 and 20000 Hz, and sound waves with a frequency above this band are called ultrasound. Waves are characterized by their amplitude, frequency and wavelength, and the propagation speed of sound depends on the propagation medium's mechanical properties. In a fluid, where c is the velocity of the wave, χ_s is the adiabatic compressibility coefficient and ρ_0 is the density, we have:

$$c = \sqrt{\frac{1}{\chi_s \rho_0}} \quad (1)$$

The wavelength of the emitted wave depends on its velocity (c.f. on the propagation medium) and on its central emission frequency. Where λ is the wavelength is f is the emission frequency, we have:

$$\lambda = \frac{c}{f} \quad (2)$$

Acoustic impedance is defined as the reaction of a material to the passage of a sound wave, and an acoustic interface separates media having different acoustic impedances. When the sound wave meets an acoustic interface, it will be partially transmitted and partially reflected following the reflexion coefficient R . Where z_i represents the acoustic impedance of a medium, we have:

$$R = \frac{z_2 - z_1}{z_2 + z_1} \quad (3)$$

Two additional phenomena are to be taken into account when studying sound: absorption and diffusion. Absorption results in the dissipation of energy in the medium, which can be transformed into heat. Diffusion causes the wave to divide in several directions. During its propagation in a tissue, sound waves will attenuate. Furthermore, the absorption and

diffusion of the wave will impose limits on ultrasound imaging as the depth of exploration will be limited.

1.1.2 Focused ultrasound therapies in short

Focused ultrasound therapies are non-invasive surgical procedures based on the emission of high intensity ultrasound pulses and allowing to induce a mechanical effect in a precise focal spot, usually heating, cutting or reducing a pathological target tissue. Ultrasound pulses are emitted by mono-element or multi-element transducers which ensure a geometrical or an electronical focusing, using in the latter case delay-laws between the elements [29].

The first successful procedures go back to the 1980's in ophthalmological applications [27] and are founded on thermal effects leading to the irreversible necrosis of tumours. We are talking about High Intensity Focused Ultrasound (HIFU), which is characterized by an important temperature elevation at the focal spot due to ultrasonic absorption.

Since then, ultrasound therapies have been widely developed for different medical applications in different organs of the human body [23][25], and today we can find three principal focused ultrasound therapies:

- HIFU, which is based on the thermal action produced by the emission of long pulses with a focal pressure usually around 8 MPa, mostly used in oncology for tumour necrosis [29];
- Lithotripsy, which is based on the emission of short pulses with a focal pressure usually around 40 MPa, leading to mechanical effects due to shockwaves and uncontrolled cavitation bubbles, mostly used for kidney stones reduction [30];
- Pulsed cavitation ultrasound therapies (PCUT) such as histotripsy, which are based on the action of nucleated inertial cavitation bubbles, with a focal pressure usually around 100 MPa [5]. This thesis will focus on this latter modality.

1.1.3 Inertial cavitation and bubbles behaviour

Cavitation is a phenomenon that consists of the creation and oscillation of gas bubbles in a compressible a fluid, following the introduction of a sufficient negative pressure. The negative pressure causes the change of state of the fluid, which is separated at places containing

gassy impurities, or "weak spots". Bubbles will then form, grow and potentially collapse [1][2]. The number of nucleated bubbles is inevitably proportional to the density of "weak spots".

We can distinguish stable cavitation, where bubbles will oscillate in size and shape without collapsing, from inertial cavitation, where bubbles will collapse violently after a few oscillations. In the latter case, we are dealing with implosions that generate localized streaming, shockwaves and can produce heat under certain conditions [1]. There are several ways of generating the depression in the fluid. For example, by the Bernoulli principle, an increase in velocity leads to a decrease in pressure:

$$\frac{1}{2}\rho v^2 + \rho gh + P = cte \quad (4)$$

This is the case for example of a working boat propeller where, at a certain rotation speed, cavitation may be nucleated and it can damage the material [2].

We will focus in this work on inertial acoustic cavitation, whose nucleation origin is based on the pressure fluctuations produced under a focused ultrasound field. We will deal with microbubbles that together will form a dense cloud of bubbles in a precise target area.

The bubbles properties and behavior are complex and depend on the medium properties, as well on acoustic parameters such as the pulse duration, the intensity or the duty cycle [1][2]. The radius of the bubbles is for example proportional to the ultrasound wavelength, which depends in turn on the ultrasonic frequency and on the propagation medium [8]. In general, bubbles oscillate in phase with the ultrasonic wave, they can meet another bubble and grow, before becoming unstable and collapsing or fragmenting in smaller bubbles as seen in Figure 1. They contract during ultrasonic compression and extend during ultrasonic rarefaction. During compression, the bubble envelope becomes thicker and during the rarefaction it becomes thinner, until instability [3]. In inertial cavitation, bubbles usually oscillate rapidly then violently collapse, inducing a mechanical effect in the surrounding media. This will be the principle of our studied therapeutic procedure.

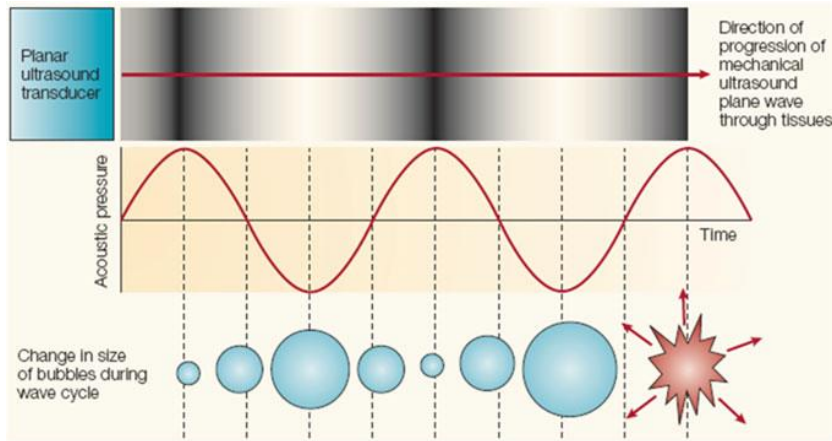


Figure 1 – Nucleation, growth and collapse of a bubble while cavitation under an acoustic field [1]

Furthermore, cavitation bubbles extend and contract asymmetrically under the acoustic field: the density and stiffness of the gas in the bubble increase during compression and decrease during the rarefaction. The oscillating gaseous bubbles become in consequence non-linear reflectors under an acoustic field and have a high echogenicity due to their high-density contrasts in relation to the surrounding tissues [4]. Non-linear behaviour causes:

- Ultrasonic signal distortion in the time domain, and enrichment in the frequency domain;
- Broadband signal reflexion for inertial cavitation [1];
- Presence of harmonics and subharmonics of the ultrasonic signal reflected after interaction with the bubble.

Such particular acoustic signal signatures are interesting and widely used for the cavitation detection and even for cavitation localization.

1.1.4 The engineering of histotripsy

Histotripsy is the process consisting in generating and controlling inertial cavitation bubbles for medical applications. It relies on the emission of short, intense and repeated focused ultrasonic pulses with a small duty cycle inducing a negative pressure in the medium inside a precise focal spot, causing the nucleation of a dense and energetic inertial cavitation cloud. The implosion of bubbles will have a non-thermal mechanical action on the tissues [5][15].

During histotripsy, an acoustic transducer generates short bursts sinusoidal ultrasound waves that will focus in the target zone, usually working at a central emission frequency

between 700 kHz and 4 MHz, with 1 to 20 repeated cycles per burst at a pulse-repetition frequency between 1 and 1000 Hz. Histotripsy locally produces pressures of up to 100 MPa and down to -25 MPa (Figure 3) [15].

The method was originally developed within the Department of Biomedical Engineering at the University of Michigan and has evolved since its introduction, as today we can find some derivations following the aimed application. For example, in 2015 the University of Washington in partnership with the University of Moscow set up a method that uses longer pulses (with a duration of the order of one second), and whose cavitation cloud also induces thermal effects: "boiling" histotripsy [6]. Both histotripsy and "boiling" histotripsy are pulsed cavitation ultrasound therapies (PCUT).

Several studies have been carried out on the bubble expansion, the effects of the propagation medium rigidity and the mechanical effects of cavitation while histotripsy on different biological tissues at the cellular and tissue level [5][7][8][9]. For example, it has been proved that the expansion of the bubbles is a function of the stiffness of the propagation tissue and of the frequency of the pulses (Figure 2), and this last parameter is to be determined according to the applications and the target tissue.

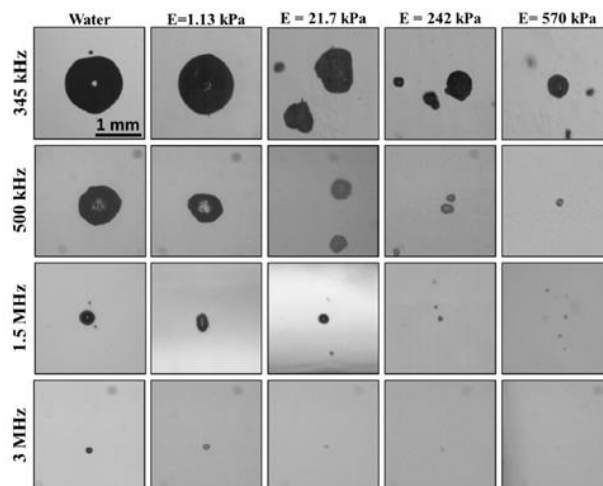


Figure 2 - Optical images of bubbles produced by 345 kHz, 500 kHz, 1.5 MHz and 3 MHz histotripsy pulses inside agarose tissue phantoms of increasing Young modulus [8]

As a consequence, acoustic parameters such as the therapeutic central frequency, the number of cycles per burst and the pulse-repetition frequency shall be chosen depending on the therapeutic application, and particularly depending on the nucleation medium, on the mechanical properties of the target tissue and on the required cavitation cloud size. For example,

in applications inside tight places such as the veins for thrombolysis using histotripsy [10], the cavitation cloud size must be big enough to allow the treatment efficacy, but small enough not to destroy the healthy cells along the vein walls.

It should be kept in mind that histotripsy has a wide range of applications. Among others, the creation of inter-atrial communication [7], adipose tissue reduction, thrombolysis [10], liver cancer or prostatic hyperplasia are under development [5].

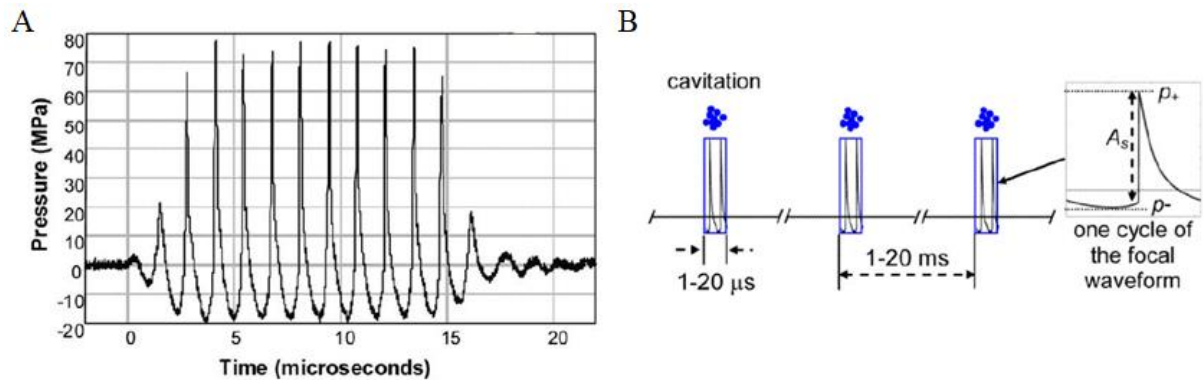


Figure 3 – A: Typical histotripsy pressures at the focus [5]
 B: Non-thermal histotripsy common timings showing the typical non-linear waveform at high pressure regimes [5]

1.2 Ultrasound imaging for the guiding and the monitoring of PCUT

1.2.1 B-Mode ultrasound imaging in short

Ultrasound imaging is a technique consisting in sending ultrasonic waves into a heterogeneous physical medium through a probe and in a privileged direction. When crossing the different acoustic interfaces in the medium, the ultrasonic waves will be partially reflected. Those reflections are called "echoes". The echoes will then be received by the probe, processed and digitized. The processing of these signals makes it possible to reconstruct a greyscale image in real time.

The probe contains complex electronics for the signal conditioning and processing, and in particular it is composed of transducers (usually made of piezoelectric materials) that transform both an electronic signal into an acoustic signal for the creation of ultrasonic waves, and an acoustic signal into an analogical electrical signal for the reception of the echoes. Thus, an ultrasound sequence is composed first of an emission period ($\approx 1\%$ of the time) and secondly of a listening period.

Basically, transducers will emit ultrasound in a specific direction, and the amplitude of the echoes received from this emission will allow to form a line with different grey levels. Next, a second emission in a contiguous direction will allow the formation of a second line, and so on the formation and juxtaposition of several lines will produce a two-dimensional ultrasound image in “conventional” B-Mode (B for "brightness"). B-Mode images evolve over time and allow the dynamic visualization of a region of the body usually between 10 and 70 frames per second.

A first technical challenge stands on the line-by-line scanning of the area to explore, which is mostly electronical. For a linear scan, it consists of the ultrasonic emission through subgroups of transducers, and the shift of the subgroups at each transmission-reception. Each subgroup of transducers will form a shooting line (Figure 4 - Left). For a sector scan, for example for cardiac applications, it consists of the emission of ultrasound with delays between the transducers. Delays will steer the exploration line in specific directions for scanning, and each transmission-reception will have a given delay law (Figure 4 - Right).

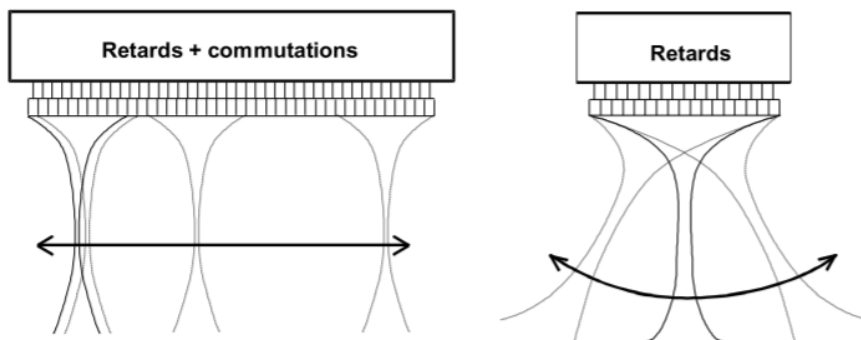


Figure 4 - Left: Linear scan
Right: Sector scan [20]

The shooting line density and the scanning frequency will influence the quality and the frequency of the images. Furthermore, apart from the pure digital signal processing, there are several factors that affect the quality of the signal and that will depend on the desired medical application:

- Mechanical focusing thanks to an acoustic lens;
- Electronical focusing quality;
- The number and arrangement of the transducers used;
- The geometry and size of the probe (and of the transducers);

- The amplitude of the pulses;
- The frequency and duration of the pulses.

We usually work in an emission frequency range between 1 and 20 MHz, with an acoustic pressure of about 3 MPa, and we usually assume that ultrasound travels at a constant speed of 1540 m/s, which is the mean speed of sound of biological tissues. This is nonetheless a strong assumption (Annexe 4).

1.2.2 Focalisation and resolution

Image resolution is defined as the ability of a device to separate two close reflective points in the sonicated medium. The two points are either resolved, confused (Figure 5) or at the resolution limit.

More in detail, the resolution may be characterized following three axes [22]. First, the axial resolution is the resolution that occurs along the beam axis. It is inversely proportional to the duration of the pulse and remains constant over the entire depth. As a consequence, a higher emission frequency will result in a better axial resolution despite a loss in imaging depth. Next, the lateral resolution is perpendicular to the axial resolution (on the imaging plane) and generally decreases with depth. For B-mode imaging, it depends mostly on the number and on the width of scan lines. Finally, the elevation resolution is perpendicular to the imaging plane and generally decreases with depth. The elevation resolution is linked to the thickness of the imaging plane. Moreover, both the lateral and the elevation resolution can be improved by using electronic or mechanical focusing.

A second technical challenge stands on focalisation to improve the image resolution, and consequently the image quality.

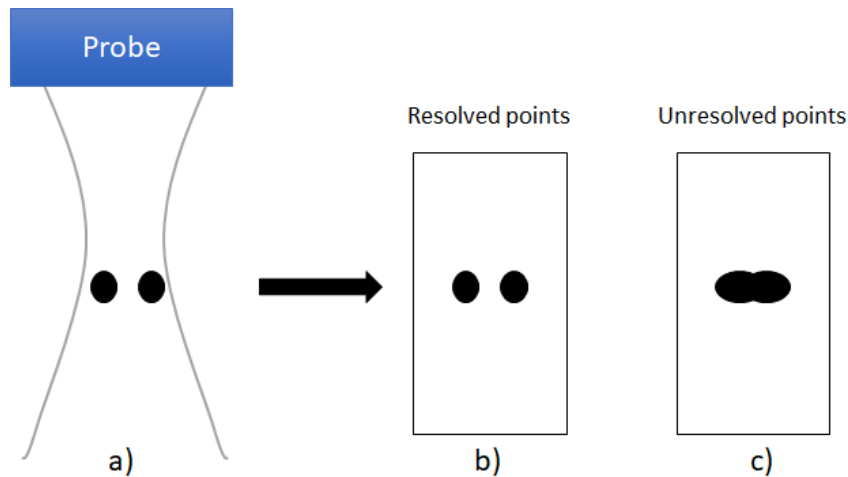


Figure 5 - Lateral resolution scheme

- a) Ultrasound emission. The medium contains two reflectors
- b) The two points are resolved in the image
- c) The two points are confused in the image

In fact, in order to obtain a thin and directional ultrasound beam with a maximum acoustic intensity, ultrasonic waves must be focused at a certain focal point where the beam width is minimal. In practice, it remains difficult to focus an ultrasound beam very locally, and we will rather speak of an area where the width of the ultrasound beam is minimal and therefore where the resolution is the best: the focal spot (Figure 6). There are mainly two technical solutions to focus ultrasound, mechanical or electrical.

Two mechanical solutions coexist mainly. The first solution consists in designing an adapted geometry of the probe so that the transducers are oriented towards the same point. This solution may improve the elevation resolution, but it is rarely used in imaging as it does not allow a dynamic focusing when scanning and it imposes a fixed focal spot. It is nonetheless widely used for therapy transducers.

The second mechanical solution consists in setting an acoustic lens at the output of the probe. The lens allows the ultrasound to be focused without using the electronics and therefore without affecting the processing performance, but again the focus spot is fixed. Acoustic lenses, usually cylindrical, are widely used to improve the elevation resolution.

Today, most of solutions for the lateral resolution improvement are electrical and consist in the setup of delay laws between the transducers (commonly on all the transducers for a sector scan and on subgroups of transducers for a linear scan, Figure 4 and Figure 6). The ultrasonic waves will therefore be emitted at different times, and next they will interfere

constructively so their sum results in the convergence of the beam towards the focal spot (Figure 6). Furthermore, with this solution it is possible to vary the depth of the focal spot and thus easily control the exploration depth.

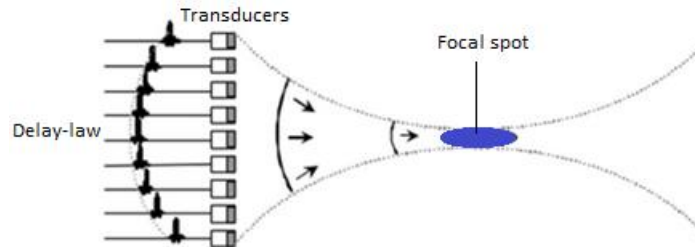


Figure 6 - Delay law for ultrasound focalisation [20]

1.2.3 Ultrafast imaging

The engineering of ultrasound has been constantly evolving along with technology, and other modalities exist today such as ultrafast imaging. Ultrafast imaging is based on the emission and processing of the "echoes" from a single plane or divergent wave sonicating the whole medium. Theoretically, for a wave velocity of 1540 m/s and a depth of 50 mm, the frame rate may reach about 10000 frames per second.

At this frame rate, it is possible to precisely observe very fast phenomena, such as longitudinal waves propagation (c.f. elastography [31]) or blood flow in a whole imaging plane (c.f. functional ultrasound imaging [32]).

Ultrafast imaging allows very high frame rates, but heavy electronics are required to process all the data at the same time and the image is degraded in terms of contrast and resolution compared to conventional B-Mode [21]. To go further, coherent compounding may be used to improve the image quality. It consists in the emission of plane waves at different angles, followed by the sum/recombination of the successive echoes of the emitted plane waves, this increasing the signal-to-noise ratio (SNR) as presented in Figure 7 despite a loss in frame rate.

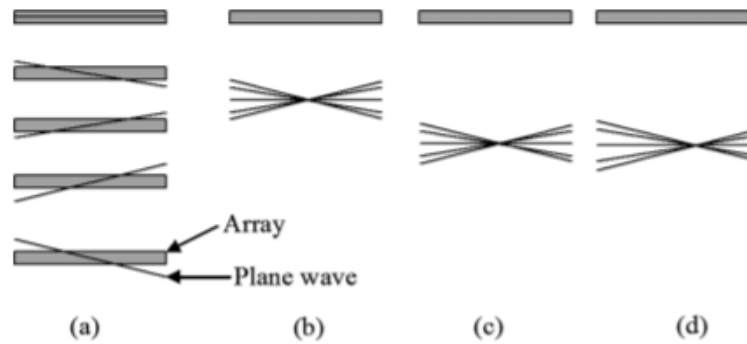


Figure 7 - Ultrafast imaging principle [21]

(a) Individual plane waves sent with the compound method
 (b), (c), (d) The coherent synthetic addition of the plane waves with the adequate delays enables lateral and axial focusing

1.2.4 From HIFU monitoring to histotripsy monitoring

Focused ultrasound therapies are non-invasive surgical procedures that started to quickly develop since the 1980's [27] and due to their non-invasiveness, there is no direct visual feedback of the therapies targeting and action. Nevertheless, for safety reasons, it is essential to ensure the proper advancement of the procedure by knowing the exact ultrasonic action zone in relation to the anatomical tissues.

Different imaging modalities for monitoring have been developed since then. For example, HIFU Magnetic Resonance Imaging (MRI) guidance allows to estimate the temperature elevation at the focal spot non-invasively [28]. However, the temporal resolution and the clutter and the cost of MRIs are big difficulties for a device set-up.

At this point, ultrasound imaging allows to easily visualize the inner tissues of a patient, non-invasively and in real-time. HIFU monitoring modalities have been widely developed for the temperature elevation estimation using the propagation speed of sound, displacement estimation or pulse-inversion among others [23][24][26]. Other modalities consist in using elastography for the evaluation of the rigidity of the medium, and this way precisely evaluating the lesion location [25].

Now, the monitoring problematics in therapies such as histotripsy are very different as there are no heating effects and, as we saw, cavitation bubbles are non-linear reflectors and have a high echogenicity under an ultrasonic field [4], which typically allows to discriminate the bubble cloud from the surrounding tissues. Today, histotripsy is commonly guided and monitored using conventional B-Mode imaging [5][10][14]. For guiding, while the therapy is

disabled, ultrasound imaging allows to position the therapeutic focal spot in relation to the anatomical tissues. For monitoring, while the therapy is on, ultrasound imaging allows to visualize the cavitation cloud position in relation to the anatomical tissues, and to ensure that the target is correctly reached for a safe procedure.

A first engineering challenge in histotripsy guiding and monitoring involves the fact that the imaging probe must be positioned in a way that the bubble cloud nucleates inside the imaging plane, usually in a coaxial position with the therapeutic transducer, and the mechanical alignment of both transducers shall be ensured during the whole procedure.

Some other technical challenges exist, as both the therapeutic and the imaging emissions are ultrasound-based. In fact, histotripsy pulses may be emitted at the same time as imaging pulses, and as they are more energetic, they will take over and “pollute” some B-Mode image scan lines. This phenomenon will interfere with the proper monitoring of the procedure. As histotripsy pulses are usually very short, a quick solution to this problem is simply to trigger the imaging emission to wait for the therapeutic wave to do a round-trip in the medium. This way, imaging scan lines are emitted between therapeutic bursts, and B-Mode images may be properly formed (with a slight loss on the frame rate nonetheless).

Yet, the B-Mode image lacks specificity and its quality is deteriorated in depth, and in deep organs the monitoring capabilities decrease as the bubble cloud is less easily differentiated from the tissues, being particularly difficult in moving organs. The bubble cloud visualization becomes subjective, and it is not simple to differentiate its shape and boundaries. As a consequence, there is a need to develop alternative imaging modalities to extract the bubble cloud information, and to allow a proper histotripsy monitoring even in deep and moving organs.

This is the case of cardiac applications.

1.3 Calcified aortic stenosis

The aortic valve is the valve in the human heart placed between the left ventricle and the aorta (Figure 8 C). Anatomically, it has three leaflets, each one composed of four cellular layers: endothelial cells, the *fibrosa*, the *spongiosa* and the *ventricularis* (Figure 8 B), all together assuring the strength and the elasticity of the valve for its proper function [19].

Physiologically, the aortic valve ensures the blood ejection from the heart to the rest of the body (systemic circulation) and prevents backflow (Figure 8 A).

When the left ventricle contracts (systole), its internal pressure starts to rise as the valves are closed, and when this pressure reaches a threshold above the physiological pressure in the aorta, the aortic valve opens, and blood is ejected. When the ventricular contraction ends (diastole), pressure in the left ventricle rapidly drops, the aortic valve closes, the ventricle is refilled with fresh blood and the cycle is repeated at every heartbeat [17].

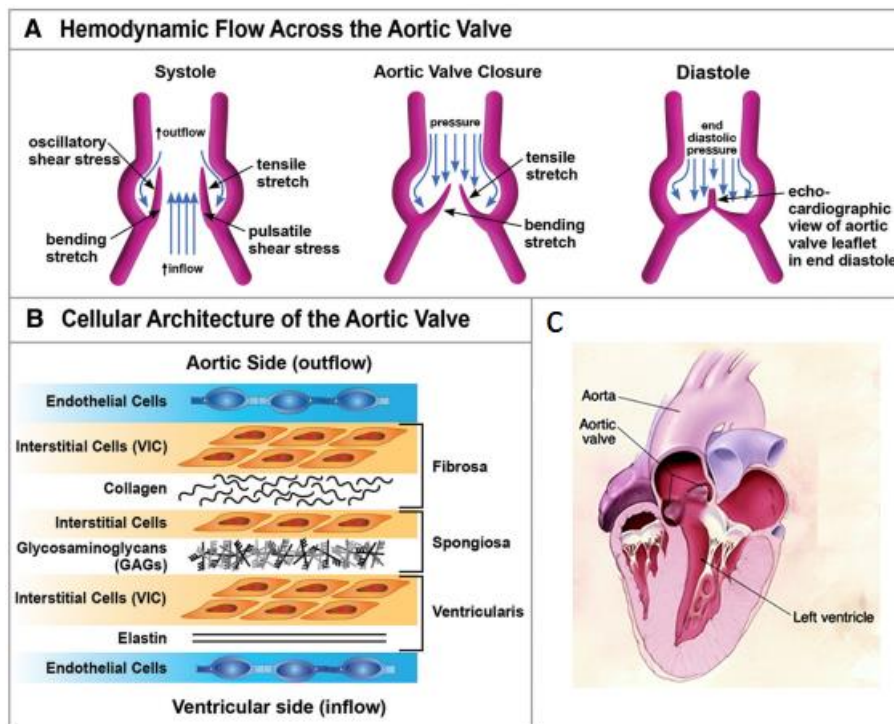


Figure 8 – A: Hemodynamic forces during the systole and the diastole in the aortic root [19]

B: Cellular architecture of the aortic valve [19]

C: Scheme of a slice of the human heart. Are visible the left ventricle, the opened aortic valve and the aorta [18]

Calcified aortic stenosis (CAS) is a degeneration of the aortic valve that consists of a gradual accumulation of calcareous deposits inside the leaflets, usually in the *fibrosa*, causing the stiffening of the tissue and the narrowing of the opening of the aortic valve as seen in Figure 9. As the aortic valve opening is impaired, the heart is forced to provide a bigger effort to open it and to ensure the blood ejection, and the consequences in time are chest pain, shortness of breath, heart insufficiency and finally heart failure [11]. The factors that promote the onset and the development of this pathology are age, cholesterol, tobacco and there are even genetic predispositions, among others.



Figure 9 - Left: Healthy aortic valve
Right: Aortic valve with calcified stenosis

In current medical practice, it is possible to diagnose CAS by calculating the pressure gradient ΔP_{moy} between the left ventricle and the aorta, usually estimated by ultrasound in Doppler mode. The physiological gradient is smaller than 7 mmHg and three stages of stenosis are defined [13]:

- Minor stenosis: $7 \text{ mmHg} < \Delta P_{moy} < 20 \text{ mmHg}$;
- Moderate stenosis: $20 \text{ mmHg} < \Delta P_{moy} < 40 \text{ mmHg}$;
- Severe stenosis: $\Delta P_{moy} > 40 \text{ mmHg}$.

Aortic stenosis affects 3% of the population aged 65 and over and 12% of people over 75: it has become a major public health concern because of the ageing Western population. 1 person out of 10 could be affected in the near future and there are currently 10 million patients affected in Western countries. A patient affected with a severe symptomatic aortic stenosis has a survival rate of 2 to 5 years, and the overall cost to treat aortic valve disease exceeds \$50bn in Europe and in the US.

Today, the highly invasive highly risky gold standard medical response to this pathology is to replace the native valve with an artificial one (biological or mechanical) via an open-heart surgery, consisting in:

- Accessing the heart via a thoracotomy;
- Connecting the patient to an extra-corporeal circulation that will replace the cardiac function;
- Stopping the heart;
- Opening the heart, replacing the valve, closing the heart;
- Restarting the heart.

Nevertheless, in the recent years, cardiac surgery has been evolving to less risky and less invasive solutions. Since 2002, transcatheter aortic valve replacement (TAVR) is more and

more in use, consisting in pushing a thin catheter through major arteries all the way to the heart and to deploy an artificial valve, crushing the native one.

These kind of high-risk interventions (3 to 10% of deaths in the course of intervention) remain expensive, they need anaesthesia and are accompanied by risks such as stroke, cardiac arrest or heavy infections, among others [12]. The postoperative is painful, usually leaves sequelae and sometimes leads to morbidity. Moreover, it remains a percentage of patients who is simply not eligible for surgery, for medical or personal reasons.

There is still a medical need to pursue the development of novel cardiac surgery modalities.

1.4 A potential solution for calcified aortic stenosis using a PCUT solution

1.4.1 Cardiawave SA

Cardiawave is a start-up created in 2014 from the work of the medical team of the Langevin Institute in Paris (now Physics for Medicine Paris) on non-invasive solutions for cardiac pathologies using ultrasound.

The goal of the company is to develop an ultrasound-guided histotripsy device, applied on the thorax of the patient, that will mechanically break CAS calcifications and this without hurting the healthy tissues as there are no heating effects, softening the aortic valve and reducing the pressure gradient to more physiological values. Of its non-invasive character, histotripsy results less expensive than conventional surgeries, allows the reduction of certain risks related to surgery such as infections, allows the patient to return home on the same day of the procedure, with an easier postoperative recovery, the absence of external scars and the reduction of morbidity.

Cardiawave's proposed therapy is based on a cavitation cloud steering over the valve surface: cavitation is not static, which prevents the drilling of the valve. A first paper was published proving the improvement of the valvular function using histotripsy on calcified bioprosthesis [14].

Valve replacements are today's gold standard for the treatment of CAS, and even if there is a constant improvement of the techniques, in particular with the mini-invasive tendencies, they still represent a high risk for the patient and there is a medical need.

Nevertheless, it is to be noted that it is hard to know exactly what is happening between cavitation bubbles and CAS calcifications. Two principal mechanisms are highlighted:

- The shockwaves known to weaken the solid structures. This effect has been demonstrated on kidney stones and explains that they are reduced into several pieces [15];
- Microjets known to attack the interfaces of solid materials (solid-soft tissue interfaces). This effect has also been demonstrated experimentally by filming inertial cavitation bubbles. This effect contributes to the damage of boat propellers [1].

There are also other possible mechanisms. For example, in soft tissues histotripsy, the cells are damaged directly by the force exerted by the bubbles in their vicinity [1][15]. In our case, we can imagine that there are all these effects.

The project is developed in partnership with Physics for Medicine Paris and the European Hospital Georges Pompidou, and at this date, both safety and efficacy preclinical trials have already been driven.

1.4.2 Safety and efficacy parameters

Preclinical trials of therapy on implanted calcified biologic valves were performed on 8 sheep and 7 pigs. Efficacy was proved as the aortic valve function was improved with a statistically significant decrease of the pressure gradient from 21.1 ± 4 mmHg to 9.6 ± 2 mmHg, and a wider opening of the valve. Furthermore, the calcified valve was effectively softened by inertial cavitation. The stiffness of the valve was evaluated using shear wave elastography proving a decrease from 105.8 ± 9 kPa to 46.6 ± 4 kPa *in vitro* from 82.6 ± 9 kPa to 41.8 ± 7 kPa *in vivo* [14].

On the other hand, at this date, preclinical trials of therapy in 30 healthy pigs, with healthy valves, were driven to evaluate the effects of histotripsy on cardiac tissues and on the lungs, the response of the cardiac function during and after sonication and the possible released

debris size, all of this to assess the safety of the procedure. Each session consisted in sonication for 80 minutes for each pig with a 30-days follow-up. The result was that:

- There are no large debris;
- There is no tissue perforation;
- There are no signs of stroke, heart failure or aortic regurgitation.

1.4.3 Quick feedback of ultrasound imaging in preclinical trials

As presented before, Cardiawave SA ran preclinical trials of therapy in 30 healthy pigs (with healthy valves) to prove the safety of the procedure. For now, Cardiawave's therapy is guided using conventional B-Mode which allows sufficient guidance and monitoring performances of PCUT to ensure the safety of the procedure.

Nevertheless, there is a strong variability between the pigs as each one has an intrinsic echogenicity, and the image contrast depends on echogenicity. The cavitation cloud is not always fully visible, and its precise boundaries remain subjective and operator dependent. We can expect the same behaviour on human patients.

Please find in Figure 10 conventional B-Mode images of a healthy aortic valve while histotripsy *in vivo* on a pig. We can observe in a) the opened aortic valve before cavitation nucleation, the following frame b) where the cavitation begins to grow and c) a frame showing cavitation over the valve. As we can appreciate, the cardiac tissues and the bubble cloud present roughly the same grey levels, so the contrast of ultrasound imaging does not allow to differentiate them. As a consequence, the cavitation cloud boundaries remain hard to delimitate.

Therefore, first a cavitation detection method, and second a cavitation imaging method would be interesting tools to make the procedure even safer, giving the physicians an "ON/OFF" indicator of cavitation and a complete mapping of the bubble cloud.

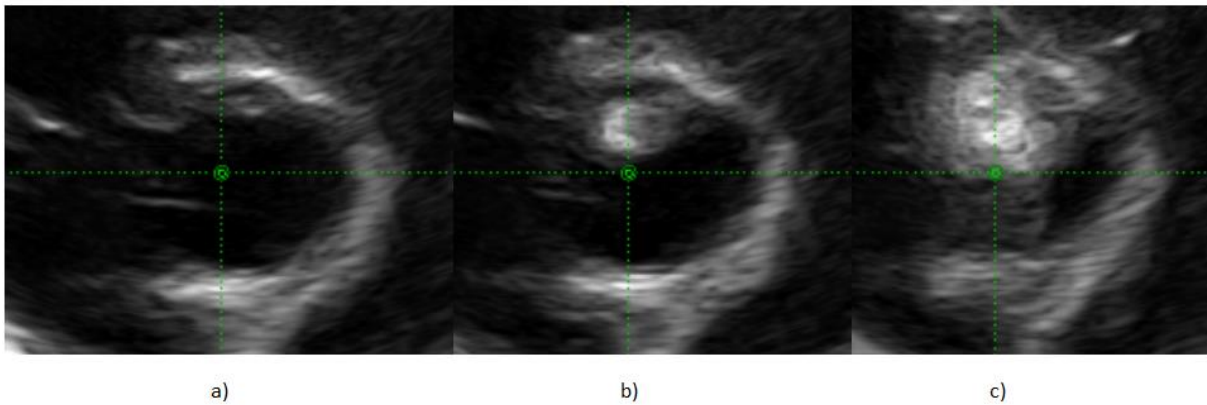


Figure 10 - Conventional B-Mode imaging while histotripsy *in vivo* in a healthy aortic valve, on the pig
a) Moment before the cavitation nucleation
b) Following frame, where the cavitation cloud begins to grow
c) Cavitation over the healthy valve
The green dot lines join at the therapeutic target spot

1.4.4 Valvosoft®

Cardiawave's device, the Valvosoft® platform, is an ultrasound image guided medical device delivering high intensity focused ultrasound for histotripsy. The contact between the device and the patient is ensured through a biocompatible acoustic conductive pouch filled with degassed water, and the whole system is guided by a robotic arm.

Furthermore, Valvosoft® includes a user-friendly human-machine interface (HMI) for the patient management and the therapy planification, and the whole system is optimized to work in a clinical environment.

There are two ultrasound systems: one for imaging and one for therapy. The imaging system is composed of an embedded original equipment manufacturer (OEM) that allows classic B-Mode cardiac performances. The therapeutic ultrasound generation chain is composed of:

- A signal generator;
- An amplifier;
- Impedances matching;
- A multi-element acoustic transducer with a spherical shape. The transducer design allows a therapeutic focal spot steering along its central axis, and it has a central hole for the imaging probe to be put through (Figure 61 a)).

Chapter I – State of art

Both imaging and therapy transducers are embedded inside an applicator. The applicator includes a mechatronic system that moves the transducer along the imaging plane (the imaging probe does not move) so that the therapeutic focal spot can be steered in two dimensions and enables Valvosoft® to focus cavitation on an entire 2D plane (Figure 61 b)). The whole applicator is to be paired with the patient's skin through the acoustic conductive pouch filled with degassed water. The complete system is presented in Figure 11.

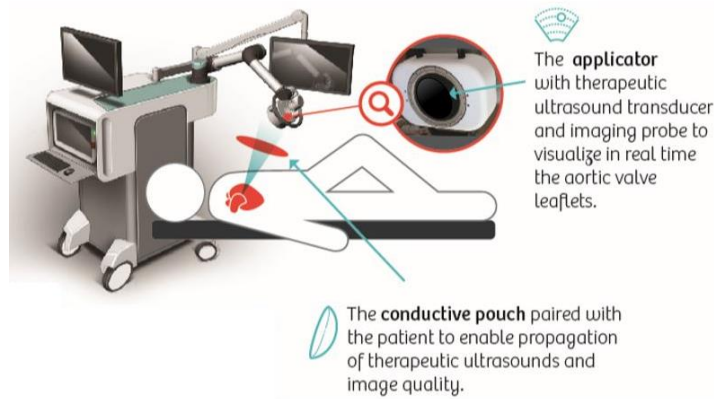


Figure 11 - Valvosoft platform [16]

For cavitation generation, the emission frequency is comprised between 700 kHz and 1.25 MHz, the pulse repetition frequency is comprised between 100 and 300 Hz and the in-situ focal pressure is estimated between -15 and -19 MPa. Besides, we measured a mean loss through the ribs of $59\% \pm 9\%$.

Bibliography

1. Wan, Mingxi, Yi Feng, and Gail ter Haar, eds. *Cavitation in Biomedicine: Principles and Techniques*. Springer Netherlands, 2015.
2. Brennen, Christopher E. *Cavitation and Bubble Dynamics*. Oxford University Press, 1995.
3. Leong, Thomas, Muthupandian Ashokkumar, and Sandra Kentish. “THE FUNDAMENTALS OF POWER ULTRASOUND – A REVIEW.” *Acoustics Australia*, n.d., 10.
4. Bakhtiari-Nejad, Marjan, and Shima Shahab. “Effects of Nonlinear Propagation of Focused Ultrasound on the Stable Cavitation of a Single Bubble.” *Acoustics* 1, no. 1 (June 2019): 14–34.
5. Khokhlova, Vera A., J. Brian Fowlkes, William W. Roberts, George R. Schade, Zhen Xu, Tatiana D. Khokhlova, Timothy L. Hall, Adam D. Maxwell, Yak-Nam Wang, and Charles A. Cain. “Histotripsy Methods in Mechanical Disintegration of Tissue: Towards Clinical Applications.” *International Journal of Hyperthermia* 31, no. 2 (February 17, 2015): 145–62.
6. Khokhlova, Vera, Ari Partanen, Adam Maxwell, Tatiana Khokhlova, Wayne Kreider, Michael Bailey, Navid Farr, Yak-Nam Wang, George Schade, and Oleg Sapozhnikov. “Boiling Histotripsy Method to Mechanically Fractionate Tissue Volumes in Ex Vivo Bovine Liver Using a Clinical MR-Guided HIFU System.” *Journal of Therapeutic Ultrasound* 3, no. Suppl 1 (June 30, 2015): O88.
7. Xu, Zhen, Gabe Owens, David Gordon, Charles Cain, and Achi Ludomirsky. “Non-Invasive Creation of an Atrial Septal Defect by Histotripsy in a Canine Model.” *Circulation* 121, no. 6 (February 16, 2010): 742–49.
8. Vlaisavljevich, Eli, Kuang-Wei Lin, Matthew Warnez, Rahul Singh, Lauren Mancia, Andrew J. Putnam, Eric Johnsen, Charles Cain, and Zhen Xu. “Effects of Tissue Stiffness, Ultrasound Frequency, and Pressure on Histotripsy-Induced Cavitation Bubble Behavior.” *Physics in Medicine and Biology* 60, no. 6 (March 21, 2015): 2271–92.
9. Bani, Daniele, Alessandro Quattrini Li, Giancarlo Freschi, and Giulia Lo Russo. “Histological and Ultrastructural Effects of Ultrasound-Induced Cavitation on Human Skin Adipose Tissue.” *Plastic and Reconstructive Surgery Global Open* 1, no. 6 (October 7, 2013).

10. Maxwell, Adam D., Charles A. Cain, Alexander P. Duryea, Lingqian Yuan, Hitinder S. Gurm, and Zhen Xu. “Noninvasive Thrombolysis Using Pulsed Ultrasound Cavitation Therapy – Histotripsy.” *Ultrasound in Medicine & Biology* 35, no. 12 (December 2009): 1982–94.
11. Faggiano, Pompilio, Francesco Antonini-Canterin, Ferdinando Baldessin, Roberto Lorusso, Antonio D’Aloia, and Livio Dei Cas. “Epidemiology and Cardiovascular Risk Factors of Aortic Stenosis.” *Cardiovascular Ultrasound* 4 (July 1, 2006): 27.
12. Xiong, Tian-Yuan, Yan-Biao Liao, Zhen-Gang Zhao, Yuan-Ning Xu, Xin Wei, Zhi-Liang Zuo, Yi-Jian Li, et al. “Causes of Death Following Transcatheter Aortic Valve Replacement: A Systematic Review and Meta-Analysis.” *Journal of the American Heart Association: Cardiovascular and Cerebrovascular Disease* 4, no. 9 (September 21, 2015)
13. “Aortic Valve Stenosis: Evaluation and Management of Patients with Discordant Gra.” <https://www.escardio.org/Journals/E-Journal-of-Cardiology-Practice/Volume-15/Aortic-valve-stenosis-evaluation-and-management-of-patients-with-discordant-grading>.
14. Villemain, Olivier, Justine Robin, Alain Bel, Wojciech Kwiecinski, Patrick Bruneval, Bastien Arnal, Mathieu Rémond, Mickael Tanter, Emmanuel Messas, and Mathieu Pernot. “Pulsed Cavitation Ultrasound Softening: A New Noninvasive Therapeutic Approach for Calcified Bioprosthetic Valve Stenosis.” *JACC: Basic to Translational Science* 2, no. 4 (August 1, 2017): 372–83.
15. Escoffre, Jean-Michel and Bouakaz, Ayache, eds. *Therapeutic ultrasound: volume 880*. Springer Netherlands, 2014.
16. www.cardiawave.com
17. <http://www.gwheartandvascular.org/education/anatomy-and-function-of-the-heart-valves/>
18. Nishimura, Rick. “Aortic valve disease”. *Circulation* 13 August 2002: 770-772
19. Rajamannan, Nalini M., Frank J. Evans, Elena Aikawa, K. Jane Grande-Allen, Linda L. Demer, Donald D. Heistad, Craig A. Simmons, et al. “Calcific Aortic Valve Disease: Not Simply a Degenerative Process: A Review and Agenda for Research From the National Heart and Lung and Blood Institute Aortic Stenosis Working Group Executive Summary: Calcific Aortic Valve Disease – 2011 Update.” *Circulation* 124, no. 16 (October 18, 2011): 1783–91. <https://doi.org/10.1161/CIRCULATIONAHA.110.006767>.

20. Cachard, C., Basset, O. et Delachartre, P. Ultrasons, imagerie, échographie médicale.
21. Tanter, Mickael, and Mathias Fink. “Ultrafast Imaging in Biomedical Ultrasound.” *IEEE Transactions on Ultrasonics, Ferroelectrics, and Frequency Control* 61, no. 1 (January 2014): 102–19. <https://doi.org/10.1109/TUFFC.2014.2882>.
22. Ng, Alexander, and Justiaan Swanevelder. “Resolution in Ultrasound Imaging.” *Continuing Education in Anaesthesia, Critical Care and Pain* 11, no. 5 (October 1, 2011): 186–92. <https://doi.org/10.1093/bjaceaccp/mkr030>
23. Mathieu Pernot. Nouvelles techniques de thérapie ultrasonore et de monitoring. Physique [physics]. Université Paris-Diderot - Paris VII, 2004.
24. Song, Jae Hee, Yangmo Yoo, Tai-Kyong Song, and Jin Ho Chang. “Real-Time Monitoring of HIFU Treatment Using Pulse Inversion.” *Physics in Medicine and Biology* 58, no. 15 (August 7, 2013): 5333–50. <https://doi.org/10.1088/0031-9155/58/15/5333>.
25. Bastien Arnal. Elastographie pour le suivi des thérapies par ultrasons focalisés et nouveau concept de cavité à retournement temporel pour l’histotripsie. Acoustique [physics.class-ph]. Université ParisDiderot - Paris VII, 2013.
26. Grondin, Julien, Thomas Payen, Shutao Wang, and Elisa E. Konofagou. “Real-Time Monitoring of High Intensity Focused Ultrasound (HIFU) Ablation of In Vitro Canine Livers Using Harmonic Motion Imaging for Focused Ultrasound (HMIFU).” *Journal of Visualized Experiments*, no. 105 (November 3, 2015). <https://doi.org/10.3791/53050>.
27. Lizzi, F.L., Coleman, D., Driller, J., Franzen, L. A. and Leopold, M. “Effects of pulsed ultrasound on ocular tissue”. *Ultrasound Med Biol*, 7(3): 245-50 (1981)
28. “MRT Zum Monitoring Bei Hochintensivem Fokussiertem Ultraschall | SpringerLink”. <https://link.springer.com/article/10.1007%2Fs00117-012-2463-4>.
29. Tempany, Clare M. C., Nathan J. McDannold, Kullervo Hynynen, and Ferenc A. Jolesz. “Focused Ultrasound Surgery in Oncology: Overview and Principles.” *Radiology* 259, no. 1 (April 2011): 39–56. <https://doi.org/10.1148/radiol.11100155>.
30. Junuzovic, Dzelaludin, Jelena Prstojevic, Munira Hasanbegovic, and Zahid Lepara. “Evaluation of Extracorporeal Shock Wave Lithotripsy (ESWL): Efficacy in Treatment of Urinary System Stones.” *Acta Informatica Medica* 22, no. 5 (2014): 309. <https://doi.org/10.5455/aim.2014.22.309-314>.

31. Bercoff, J.; Tanter, M. & Fink, M. “Supersonic shear imaging: A new technique for soft tissue elasticity mapping”. *IEEE Transactions On Ultrasonics Ferroelectrics and Frequency Control* 51(4), 396--409. (2004)
32. Demene, Charlie, Thomas Deffieux, Mathieu Pernot, Bruno-Felix Osmanski, Valerie Biran, Jean-Luc Gennisson, Lim-Anna Sieu, et al. “Spatiotemporal Clutter Filtering of Ultrafast Ultrasound Data Highly Increases Doppler and FUltrasound Sensitivity.” *IEEE Transactions on Medical Imaging* 34, no. 11 (November 2015): 2271–85.

Part I:
**New imaging modality for cavitation imaging: from
2D to 3D**

Chapter II - Passive coherent cavitation imaging

Adapted from:

Daniel Suarez Escudero, Guillaume Goudot, Michael Vion, Mickael Tanter, and Mathieu Pernot. “2D and 3D Real-Time Passive Cavitation Imaging of Pulsed Cavitation Ultrasound Therapy in Moving Tissues.” *Physics in Medicine & Biology* 63, no. 23 (December 6, 2018): 235028.

2.1 Introduction

Pulsed cavitation ultrasound therapies (PCUT) are currently guided by conventional B-mode ultrasound imaging, which enables a real-time visualization and localization of the bubble cloud in the tissues by the increase of echogenicity. However, B-Mode images lack specificity and the effective visualization of the bubble cloud depends strongly on the image quality, and the low contrast of B-Mode images remains an important limitation for applications in deep organs such as the heart.

In fact, it is not often clear where the bounds of the bubble cloud are and, as bubbles are generated inside heterogeneous biological and moving tissues, their echoes are difficult to discriminate as presented on Figure 12, where cavitation is enabled in the liver but the contrast is not optimal to clearly discriminate the bubble cloud from the hepatic tissue. The visualization of the bubble cloud remains subjective and qualitative for the operator.

Furthermore, owing to the stochastic nature of cavitation, the bubble cloud position, shape and size may vary over time during therapy with the acoustic parameters such as the therapeutic ultrasound gain or the focusing depth, which increases the need of a precise monitoring method: it is essential to ensure the visualization of the cavitation cloud to monitor the procedure and ensure its safety.

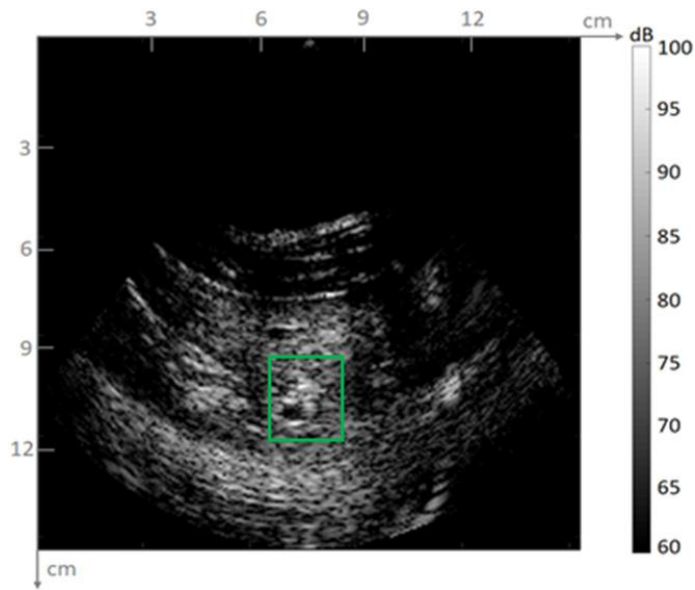


Figure 12 - In vivo B-mode image of the liver during therapeutic exposure with cavitation occurring at the focal zone. The bubble cloud is not easy to differentiate from the tissues. It is located inside the region of interest defined in the image by the green rectangle

Methods for mapping the cavitation activity have been investigated extensively over the last decade and several approaches have been proposed. Active conventional or ultrafast ultrasound imaging methods have been developed by increasing the sensitivity and specificity of ultrasound to cavitation bubbles echoes based on the non-linear [12] [15] [23] or spatiotemporal [1] behaviour of cavitation bubbles. These methods enable to increase the contrast of cavitation maps compared to conventional B-mode imaging, but cavitation maps remain altered by echoes of strong scatterers in tissues which are challenging to fully cancel, particularly when the tissues are moving rapidly.

Other approaches rely on passive imaging methods such as passive acoustic mapping (PAM) or passive cavitation imaging (PCI) [3] [4] [6] [7] [8] [9] [11]. Passive imaging methods are based on recording on an imaging probe the backscattered echoes of the bubble activity produced by a high intensity focused ultrasound beam. In most cases, these methods were developed in order to localize the cavitation activity during the emission of continuous signals or long bursts. With continuous emissions, however, the image beamforming must be performed without the knowledge of the absolute time delay between the emission of the ultrasound wave and its echoes reception on the imaging probe, resulting in a sub-optimal beamforming with low axial resolution. Moreover, these methods are based on the estimation of the backscattered intensity which is averaged incoherently at each pixel of the image during the emission. Thus, backscattered intensity is not specific to cavitation bubbles as it is also

associated with the reflections of strong tissue scatterers which can only be discriminated by the relative echo amplitudes. As a consequence, these methods are well adapted to the monitoring of cavitation in static and homogeneous tissues during long emissions, but they remain limited to localize cavitation in real-time in moving and heterogeneous tissues.

2.2 Passive coherent imaging and spatiotemporal filter

We present in this work a different approach based on passive cavitation imaging (PCI) for the real-time monitoring of PCUT in moving organs. The approach is based on the coherent pulse-echo imaging of the backscattered echoes from the high intensity pulse transmitted by a large focused transducer and received on an imaging probe embedded in the therapeutic transducer.

A spatiotemporal decomposition is used to filter out the bubble signal from the backscattered tissue echoes with high contrast, resulting on a cavitation map. The mapping of the bubble cloud can be overlaid in real-time to a classic B-Mode, which permits to localize the bubbles in relation to the anatomic image.

We performed *in vitro* and *in vivo* experiments for the evaluation and feasibility of the method.

2.2.1 Theory

Coherent passive imaging takes advantage of the fact that histotripsy pulses are very short: it is possible to precisely calculate the absolute time delays between the emission from the therapeutic ultrasound wave and the reception on the imaging transducer, this leading to an optimal coherent beamforming with a good axial resolution. Passive images will be the result of the coherent beamforming of all the echoes reflected by all the scatterers in the sonicated medium, as if it was a pulse-echo image.

- When cavitation is not enabled, the passive image will principally be the result of the beamforming of the therapeutic ultrasonic field;
- When cavitation is enabled, however, as bubbles happen to be very echogenic and strong non-linear reflectors, they are beamformed with a high contrast and result easily discriminated on the image. Nevertheless, to suppress all the possible noise and as the cavitation cloud presents a spatiotemporal behaviour different from the one of the

Chapter II – Passive coherent cavitation imaging

tissues, combining passive image acquisitions with a spatiotemporal filter allows to discriminate even better the bubble cloud, increasing the contrast.

It is to be noted that we assume that the probe is in a fixed position in relation to the transducer, and that we measured beforehand the ultrasonic time-delay δt between the imaging probe and the therapeutic transducer to be included in the beamforming algorithm. It is also to be noted that the axial resolution will depend on the length of the therapeutic burst: the longer the burst, the worst the axial resolution.

Moreover, as inertial cavitation backscattered ultrasound signal is broadband, there is no need for a specific central frequency for the imaging probe in relation to the transducer central frequency and we can use a conventional cardiac phased array (Figure 13).

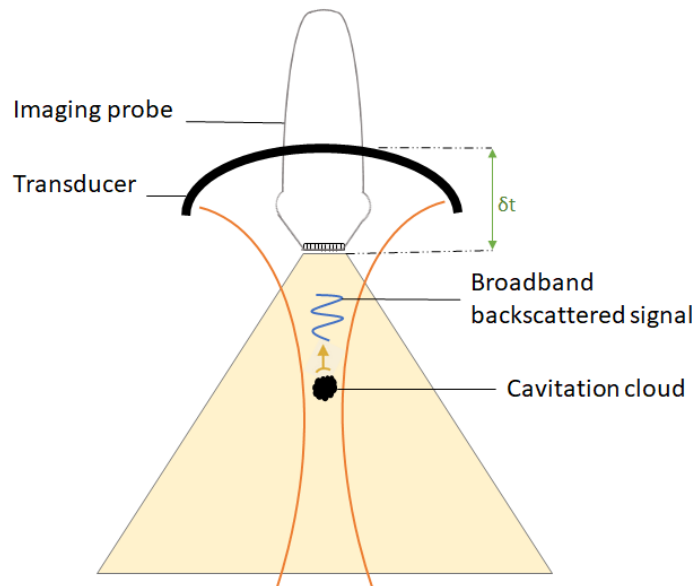


Figure 13 – Coherent passive image acquisition while cavitation

The therapeutic transducer emits focused ultrasound waves, and the backscattered echoes are acquired by the imaging probe. For the beamforming, it is necessary to include the time-delays δt between both transducers

2.2.2 Experimental setup for coherent passive feasibility

We designed a specific experimental setup to prove the feasibility and the efficacy of the passive acquisition method for histotripsy monitoring. We used a 1 MHz focused therapy transducer ($f=100$ mm, $f/D = 1$), (Imasonic[®], France) for high intensity ultrasound emissions, operated by a 2.5 kW power amplifier (RITEC[®], USA). A phased-array imaging ultrasound probe (64 elements, P4-2, Philips[®], USA) was inserted in the central hole of the transducer and

both were fixed by a 3D printed support specifically conceived for this probe. The imaging probe was connected to a programmable US scanner (Vantage 256, Verasonics®, USA). The therapy transducer driving signal was emitted by a function generator and consisted in a 1 MHz 8-cycle sine burst wave with a pulse repetition frequency (PRF) of 100 Hz (duty cycle of 0.08%). The function generator was also intended as a master clock to trigger both the US scanner and the amplifier gate input. The complete setup is described in Figure 14.

The transducer was calibrated beforehand using an in-house optical heterodyne interferometer in water [16]. The peak negative acoustic pressure was estimated between -8 MPa and -9 MPa for the *in vitro* experiments while cavitation.

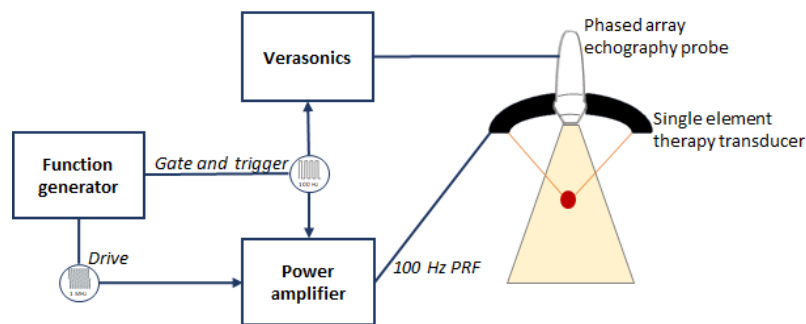


Figure 14 –Setup for real-time passive cavitation imaging. The phased array imaging probe, driven by a Verasonics system is attached to the single element therapy transducer. A function generator is used as a master clock

One passive image was acquired for each therapeutic burst (Figure 16). We programmed passive imaging events where the imaging probe operated only as a receiver. The sampling rate was set to 8 MHz and we acquired data with a 200% bandwidth using an IQ beamformer. All the 64 elements were programmed to receive data.

The vantage system and the therapy transducer were triggered simultaneously (rising edge) and the probe received data for 250 μs (see Figure 16), which is the time needed to image about 20-cm depth at $1540 \text{ m}\cdot\text{s}^{-1}$. No transmission occurs on the probe, but a burst of 8 cycles centered on 1 MHz was transmitted by the therapy transducer. The passive frame rate depends directly on the therapeutic burst emission frequency, which was 100 Hz in our case.

Passive data were beamformed as if a single divergent wave had been transmitted by the probe following a delay-and-sum beamforming, defining a synchronous transmit and receive sequence (pulse-echo). We used a CUDA optimized delay-and-sum algorithm

incorporating absolute timing information. Each frame was reconstructed in real-time after the whole 250 μ s of data was received, this covering a 90° sector, we acquired one image after each therapeutic burst and the effective frame rate was 100 Hz.

The time-delay correction allows the compensation of the spatial shift between the therapy transducer and the imaging probe. It was directly included in the beamforming algorithm and was experimentally measured prior to the experiments in a water tank by using a hydrophone placed at the focal point: it is the difference δt of the arrival time of the emissions from the two transducers when focusing on the hydrophone. We apply this delay for all the pixels by adding δt to the forward delay (see 4.6.1 *Complete ultrafast delay-and-sum beamforming*).

2.2.3 From passive images to cavitation map: the singular value decomposition filter

While histotripsy, the cavitation cloud is beamformed with high contrast in passive coherent images. However, depending on the sonicated medium, there may remain strong backscattered noise that could lead to ambiguities on the interpretation of the bubble cloud position, shape and size.

Nevertheless, cavitation clouds present a spatiotemporal behaviour different from the one of the tissues: on the one hand they are very echogenic, and on the other hand their dynamic is fast, chaotic and non-linear in relation to the one from biological tissues. It is thus possible to combine passive image acquisitions with a spatiotemporal filter allowing to suppress all the possible noise and therefore increasing the cavitation cloud contrast.

A filtering method using a Singular Value Decomposition (SVD) of ultrafast ultrasonic data in space and time has been introduced and applied to blood flow imaging [5] and was adapted to active cavitation imaging in moving organs [1]: ultrafast imaging allows to efficiently cluster tissue, blood flow or cavitation activity. It has been shown that the highest singular vectors correspond to tissue signal while blood, noise and other low spatiotemporal coherent signals are within the low singular values, and bubble cloud signals happen to be highly spatiotemporally incoherent. However, this method is highly dependent on the frame rate and is less effective in rapidly moving organs where tissue signal is also present within the low singular values.

Singular Value Decomposition is an algebraic decomposition technique of matrices. It adapts to local statistics in an image and maintains a maximum energy over a small amount of values. Briefly, it comes to factorizing a matrix $X_{m \times n}$ in the form:

$$X = U \cdot S \cdot V^* \quad (5)$$

where $U_{m \times m}$ is an orthogonal matrix, $V_{n \times n}$ is an orthogonal matrix and $S_{m \times n}$ is a diagonal matrix whose coefficients σ_i are the singular values of X . We will have:

$$\begin{pmatrix} X_{11} & \cdots & X_{1n} \\ \vdots & \ddots & \vdots \\ X_{m1} & \cdots & X_{nm} \end{pmatrix} = \begin{pmatrix} U_{11} & \cdots & U_{1m} \\ \vdots & \ddots & \vdots \\ U_{m1} & \cdots & U_{mm} \end{pmatrix} \cdot \begin{pmatrix} \sigma_1 & \cdots & 0 \\ \vdots & \ddots & \vdots \\ 0 & \cdots & \sigma_n \end{pmatrix} \cdot \begin{pmatrix} V_{11} & \cdots & V_{1n} \\ \vdots & \ddots & \vdots \\ V_{n1} & \cdots & V_{nn} \end{pmatrix}^* \quad (6)$$

Please note that V^* is the conjugate transposed of V , and that the number of non-zero singular values of S is equal to the rank of X .

Several properties are applicable to image processing. For example, low value singular values are associated with the noise of the image, and conversely most of the energy of the image is compacted in the high value singular values. This property is widely used especially for filtering and compression.

We propose to adapt the SVD spatiotemporal filter to passive cavitation imaging. As passive imaging only reconstructs the echoes of the therapeutic ultrasonic beam interactions with the medium, it avoids most of the clutter signals. Therefore, we expect this filter to be more effective in rapidly moving tissues than in the active imaging approach in [1].

The challenge of the filtering remains the choice of the right singular vectors associated.

Let us consider a set of n_t passive frames with dimensions n_x and n_z , where n_x and n_z are respectively the number of spatial samples along the x and the z directions. The whole set can be rearranged in a space-time two-dimensional matrix form $X (n_x \times n_z, n_t)$, the Casorati Matrix (Figure 15). The singular value decomposition of this matrix consists in finding singular temporal and spatial vectors, respectively regrouped in the columns of two matrices U and V (see equation (1)). As seen, U and V are unitary matrices defining respectively the temporal and spatial singular vectors, arranged from the most energetic to the least energetic.

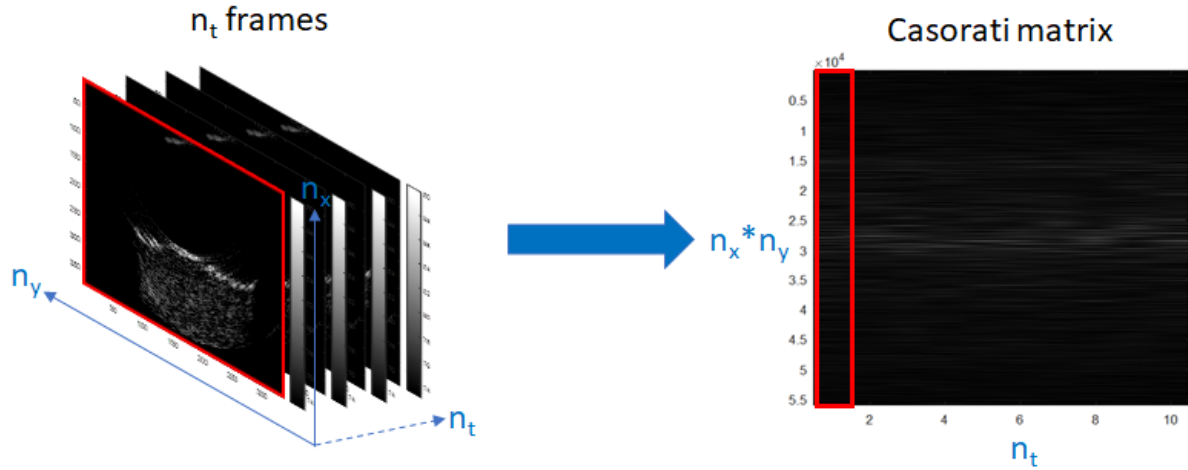


Figure 15 - Casorati matrix construction
In red is highlighted the first frame

Next to the singular value decomposition (SVD) of the matrix X , it is about to reconstruct the image using only the singular values which are relevant to the bubble cloud. We assume that the bubbles are described within a contiguous set of singular values. We then need to define the two boundary singular values p and q to finally obtain the specific bubble signals $X_{bubbles}$:

$$X_{bubbles}(n_x \times n_z, n_t) = \sum_{i=p}^q \sigma_i U_i V_i^T \quad (7)$$

This new set can be rearranged in a three-dimensional matrix form $X_{bubbles}(n_x, n_z, n_t)$, and we can compute its power integral or cavitation map (CM), which is meant to map the most energetic areas of the image:

$$CM(n_x, n_z) = \int |X_{bubbles}(n_x, n_z, n_t)|^2 dt \quad (8)$$

Thus, n_t frames will give one cavitation map, so the cavitation map will have a frame rate roughly divided by n_t compared to acquisition frame rate. Depending on the applications, it is important to optimize the number of frames to use.

Passive imaging can be combined with active ultrasound for the anatomic structures imaging during the therapeutic experiments: then, the cavitation map may be overlaid to the B-

Mode in a different color scale in real-time, this leading to a complete hybrid histotripsy monitoring sequence.

This method was patented under the following number: PCT/EP2019/063455 [27].

2.2.4 Ultrafast active acquisitions

We proposed to test different active sequences to process active cavitation imaging as it was proposed by [1]. The goal was to compare the performances to map the cavitation bubble cloud of the passive and active imaging approaches during the same experiments.

We programmed four different ultrafast sequences for active cavitation mapping on the Vantage system. For all of them, the probe's center frequency was set at 2 MHz and the Vantage system sampling rate at 8 MHz, we acquired data with a 200% bandwidth, and we used an IQ beamformer. All the 64 elements of the probe were programmed to transmit and receive data, covering a 90° sector.

The Vantage system was triggered at the falling edge, after the therapeutic burst emission. The falling edge trigger allowed us to start the acquisition at the end of the pulse, whatever its length. This prevents artefacts in the image but may reduce the frame rate, depending on the sequence. In all our active ultrafast sequences, the PRF was roughly 4000 Hz. It is necessary to have a dead time after the high intensity pulse because high intensity backscattered echoes induce strong artefacts on the active image.

The active frame rate depends on the imaging pulse repetition frequency (PRF) and on the angle compounding if any. Angle compounding increases the image contrast-to-noise ratio of the active imaging (CNR) [18].

Four active sequences were tested, acquiring N active images between two therapeutic bursts (Figure 16):

1. One ultrafast sequence with $N = 1$, where each image is the result of a single divergent wave emission (no compounding). The source was placed at 0 degrees, with a distance to the virtual apex of 16.62 wavelengths. The effective frame rate of 100 Hz. We will refer at this sequence as the “Active 100 Hz without compounding”.

2. One ultrafast sequence with $N = 11$, where each image is the result of the compounding of these 11 steered divergent wave emissions. The sources were placed starting at -0.5 degrees, with a step of 0.1 degrees and a distance to the virtual apex of 16.62 wavelengths. The effective frame rate is 100 Hz. We will refer at this sequence as the “Active 100 Hz with compounding”.

3. One ultrafast sequence with $N = 33$, where each image is the result of a single divergent wave emission (no compounding). The source was placed at 0 degrees, with a distance to the virtual apex of 16.62 wavelengths. The acquisition only stops during the therapeutic burst emissions. We will refer at this sequence as the “Active without compounding”.

4. One ultrafast sequence with $N = 33$, where each image is the result of the compounding of 11 steered divergent wave emissions. The sources were placed starting at -0.5 degrees, with a step of 0.1 degrees and a distance to the virtual apex of 16.62 wavelengths. The acquisition only stops during the therapeutic burst emissions. We will refer at this sequence as the “Active with compounding”.

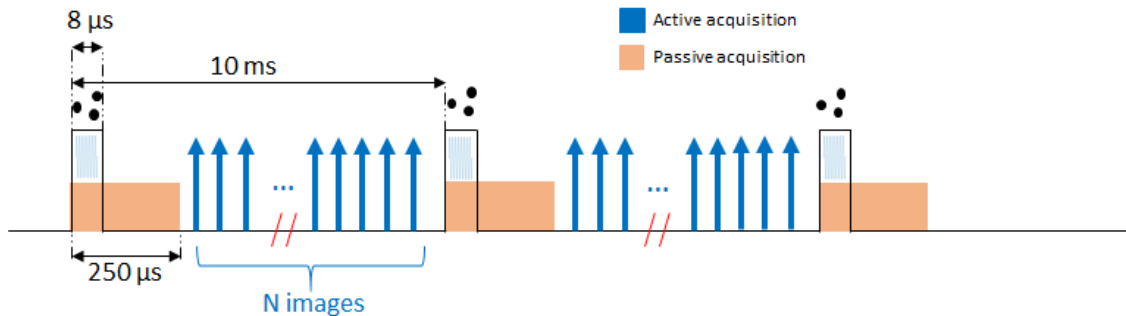


Figure 16 - Timings for the passive and active imaging sequences

Pulse repetition frequency = 100 Hz for passive acquisitions and Pulse repetition frequency = 4000 Hz for active acquisitions

There is a dead time between the passive and the active acquisition to avoid artefacts on the image

2.2.5 Cavitation map evaluation

Active and passive cavitation maps were evaluated by computing the contrast-to-noise ratio (CNR) for different sets of combinations of the parameters n_t , p and q during static and moving experiments. For each sequence we acquired 500 frames during histotripsy, and the SVD filter using different n_t , p and q combinations was applied in post-processing.

One of the secondary goals was to investigate the sensitivity of passive cavitation maps to detect cavitation *in vitro* and *in vivo*. We manually increased the signal generator emission and acquired 300 passive and 300 active frames (using the “Active 100 Hz with compounding” sequence, as we needed a good image quality) for each voltage value during pulse emission. We converted the voltage values in pressure values using the calibration curve performed in water. It should be noted that this pressure value does not take into account any attenuation factor from the tissue. We then computed the average backscattered energy at each pressure value.

For the evaluation of active and passive cavitation maps, we computed the contrast-to-noise ratio (CNR) of the cavitation bubble cloud (1), relative to the background (2) defined as:

$$CNR = \frac{\langle CM(n_x, n_z) \rangle_1 - \langle CM(n_x, n_z) \rangle_2}{\sqrt{\sigma_1 \sigma_2}} \quad (9)$$

Where $\langle \rangle_i$ stands for spatial average in region i and σ_i is the standard deviation region i . Region 1 and 2 were defined manually.

In the cavitation map, region 1 represents the bubble cloud, and we manually defined its contour. Region 2 represents the rest of the image which, in this case, represents the background noise.

2.3 Experiments and results

2.3.1 *In vitro* experiments

A phantom was prepared as in [1] with a volume of 1 liter of water and 8% of polyvinyl alcohol (PVA, Sigma-Aldrich Chemistry[®], St-Louis, MO, USA). Ultrasound scatterers were added using 1% of 20 μm diameter cellulose particles (Sigmacell cellulose, Sigma-Aldrich Chemistry[®], St-Louis, MO, USA). Tap water was heated up to 90°C using a laboratory heater and the needed volume was poured into a beaker with a magnetic stirrer. PVA was then dissolved in the water. The mixture was cooled down to 40°C, cellulose was added, and the solution was poured into a plastic square container and put in the freezer for 8 hours. The phantom was next left to defrost, then put once again in the freezer for 8 hours. At the end of the procedure, the phantom was taken out of the mold and placed in the water tank for the cavitation experiments.

Chapter II – Passive coherent cavitation imaging

The probe was attached to a two-axis stage (PI, Micos, Eschbach, Germany) and placed inside of the water tank containing the phantom (see Figure 17). Physiological motion of the liver is mainly due to breathing which induces high amplitude and rapid displacements. In [13], a maximal speed motion of the liver of roughly 6 mm/s was measured. Based on this order of magnitude, we programmed the two-axis stage with a maximal speed of 10 mm/s both for axial and lateral directions. Axial and lateral motions were induced at the same time and with the same speed.

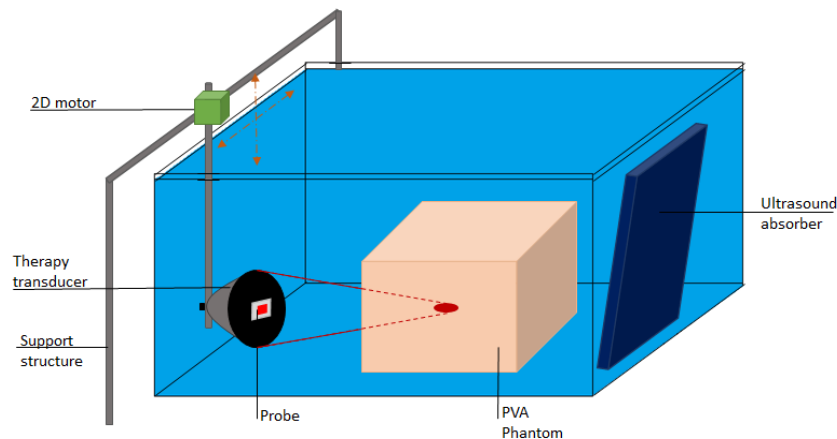


Figure 17 - Set-up for the *in vitro* experiments

Figure 18 A and Figure 18 B show an example of passive cavitation images in static tissues prior to spatiotemporal filtering, before the cavitation apparition (Figure 18 A) and while cavitation (Figure 18 B).

- Before the cavitation apparition, the image beamforms most of the therapeutic ultrasonic path when interacting with the phantom;
- While cavitation, the bubble cloud appears easily identifiable with high contrast. Nevertheless, there remain some noise and the therapeutic ultrasonic path remains visible.

In order to completely remove the contribution of tissues, SVD filtering is used in Figure 18 C and Figure 18 D.

Chapter II – Passive coherent cavitation imaging

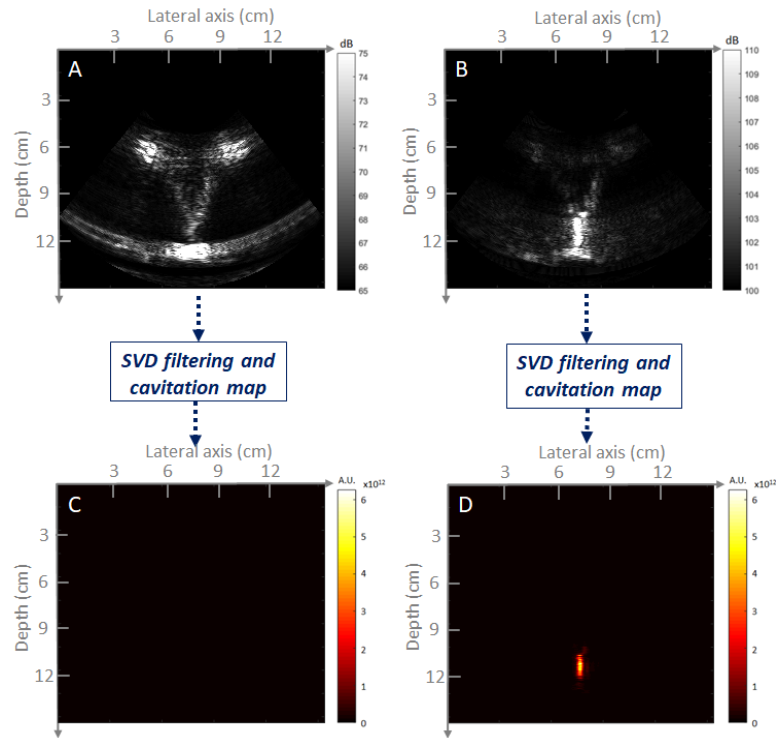


Figure 18 – A): In vitro unfiltered passive image while therapeutic pulse emission (no cavitation)

B): In vitro unfiltered passive image while therapeutic pulse emission (cavitation)

C): In vitro filtered passive image while therapeutic pulse emission (no cavitation)

D): In vitro filtered passive image while therapeutic pulse emission (cavitation)

We evaluated the CNR when the phantom was in a static condition. We fixed n_t at 6, 10 and 14 frames and we investigated the dependence of the CNR with p and q on all the active and the passive acquisitions.

In the case of both the passive and the “Active 100 Hz without compounding”, we observed that the CNR is maximal when $p = 2$ and $q = n_t$ (Figure 19 A). We suppose that the low spatiotemporal frequency noise is mostly packed in the first singular vector, and the high spatiotemporal frequencies corresponding to the bubble cloud are packed in the remaining singular vectors. We also compared the influence of n_t when $p = 2$ and $q = n_t$ (Figure 19 B), and we observed that the curve follows a logarithmic evolution and reaches a plateau globally after $n_t = 20$ for both sequences. Thus, p and q values have to be carefully chosen as it is

Chapter II – Passive coherent cavitation imaging

important to get good filtering performances by losing as little cavitation information as possible.

Secondly, considering the case where the motors are constantly moving, we fixed n_t at 6, 10 and 14, $p = 2$ and $q = n_t$, we applied the SVD filter and we computed the CNR on the cavitation maps for all the active and the passive acquisitions. We observed an important drop of CNR for all the active sequences. In contrast, the CNR remained close to its static value for the passive sequence. With motion, the CNR for the passive acquisitions appears significantly higher (10 vs 1) than the CNR achieved by all the active sequences (Figure 19 C).

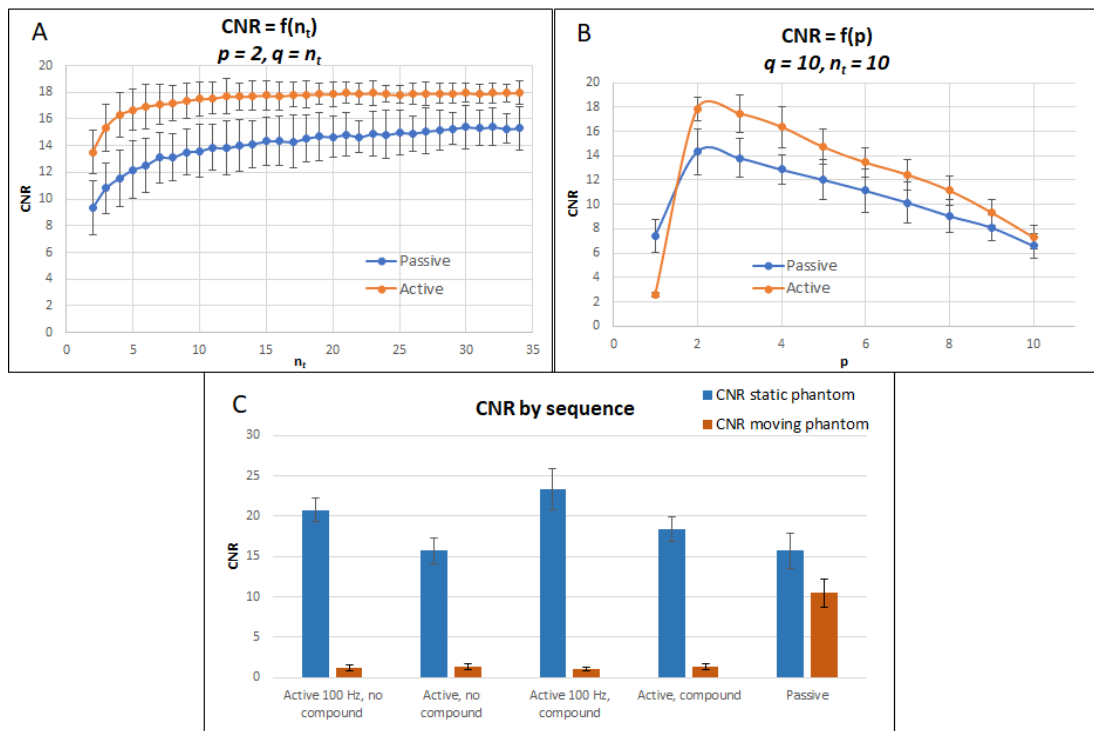


Figure 19 – 2D in vitro cavitation map Contrast-to-Noise Ratio (CNR) evaluation while cavitation

A) CNR as a function of p when $n_t=10, q=10$

B) CNR as a function of n_t when $p=2, q=n_t$

C) CNR for different active and passive sequences, when $n_t = 10, p = 2, q = n_t$

Here are presented static tissue and moving tissue conditions

Chapter II – Passive coherent cavitation imaging

Using active cavitation imaging, the SVD filtering is not as effective in the moving condition as it is in the static condition. We observed that the tissue signal is inevitably distributed over all the singular vectors and not only the first one, and that this distribution changes in time. As a consequence, the optimal SVD parameters used to reconstruct the cavitation map are also variable during time and it is not possible to fix p and q . Active cavitation imaging in the moving condition requires the constant computation of p and q as presented in [1], which is not yet optimal for real-time cavitation monitoring as the computation is time consuming. Additionally, even when updating the p and q values, the active cavitation map CNR decreases dramatically compared to static applications.

Passive imaging has the advantage to benefit from an increased spatial specificity as a reduced field is sonicated, and the backscattered echoes come from the therapeutic path only. Both in static and moving conditions, low spatiotemporal frequencies representing the tissue contribution are compacted in the first singular vector, and the bubble cloud activity contribution is roughly distributed in the remaining singular vectors (2 to n_t). This distribution is constant in time, making it more reliable to fix p and q values for a whole therapy session, this allowing a real-time cavitation monitoring.

In Figure 20 are presented the spatial singular vectors of a passive image while cavitation when $n_t = 10$.

- The first singular vector, $U = 1$, presents the therapeutic ultrasonic field and the interface between the PVA phantom and water. The bubble cloud is visible with low contrast;
- The following singular vectors, $U = 2$ to 10, present mostly the cavitation bubble cloud with high contrast.

Chapter II – Passive coherent cavitation imaging

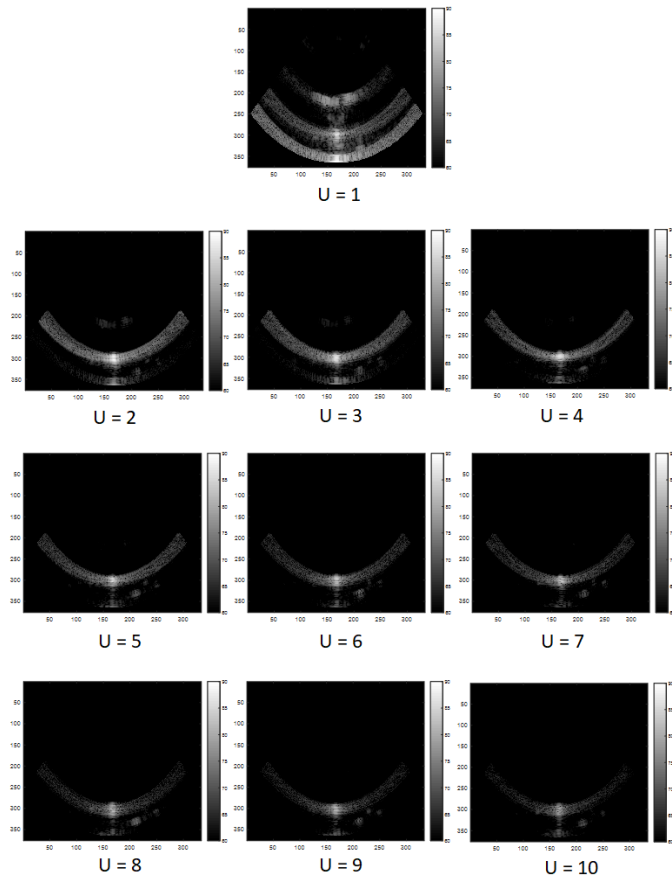


Figure 20 - Spatial singular vectors of a passive image while cavitation when $n_t = 10$

In Figure 21 are presented some examples of cavitation maps with $n_t = 10$, $p = 2$ and $q = n_t$ in static and moving conditions for the “Active 100 Hz with compounding” sequence and the passive sequence. We can observe that the cavitation map computed from the active sequence contains strong contributions from the tissue, while they are completely filtered in the passive sequence.

latex membrane. The system was positioned to target liver parenchyma by using real-time B-Mode imaging. PCUT was applied transcutaneous for 3 minutes in a fixed position under normal ventilation of the animal. For the *in vivo* experiments, SVD filter parameters were fixed to:

- $n_t = 10$ as it represents a good compromise between temporal resolution (about 100 ms at a burst repetition frequency of 100 Hz) and the CNR, as it reaches 90% of the plateau (Figure 19 B);
- $p = 2$ and $q = n_t$ as the CNR is maximal for this combination of parameters (Figure 19 A).

In Figure 22 we present an example of the results obtained *in vivo* on the porcine liver during the therapeutic procedure. The passive cavitation map was overlaid on to the B-Mode image in real-time.

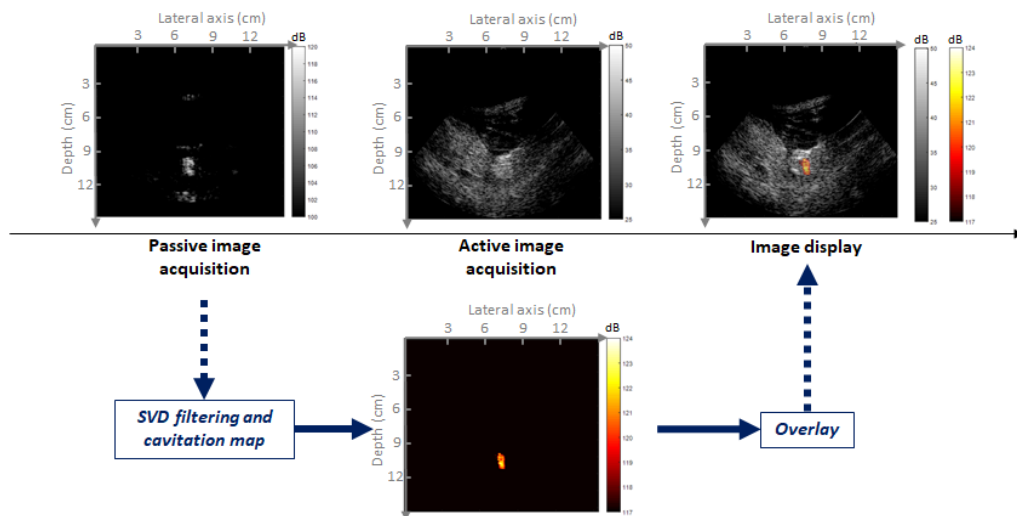


Figure 22 – Complete monitoring sequence. The passive cavitation map is overlaid onto the B-Mode image for the bubble cloud anatomic localization in real time

We quantified the average backscattered intensity inside a manually defined region of interest (ROI) around the focal spot (the ROI corresponds to the green rectangle presented in Figure 12) as a function of the decreasing estimated minimal focal pressure peak for one pig (Figure 23 A). As we acquired 300 frames per pressure value, we could average 30 cavitation maps for each level.

We observed that the backscattered power increased initially linearly with pressure. Then a sudden increase of the backscattered intensity was reached at a threshold which corresponded to the beginning of the cavitation activity. For lower pressure values, the backscattered intensity increased again with pressure but with a less clear behavior; this may be explained by the fact that there is a strong energy variability while cavitation is enabled due to the stochastic nature of the bubble cloud as it may grow, shrink, and even disappear during the ultrasound emission. This variability is represented by the error bars.

Depending on experimental conditions, in a further study it may be possible to establish a relative cavitation activity indicator or even a cavitation dose indicator based on the analysis of the cavitation map.

We compared the average backscattered intensity in the cavitation region for the B-Mode, the active cavitation maps and the passive cavitation maps for different estimated minimal focal pressure peak values (Figure 23 B). As expected, the B-Mode analysis output does not allow to precisely estimate the beginning of cavitation and does not follow the pressure decrease. In the active cavitation maps analysis output, it seems possible to detect the beginning of cavitation, but the variability represented by the error bars is too strong, especially before cavitation. Finally, passive cavitation maps allow to easily locate the beginning of cavitation, and follow the pressure decrease before and after cavitation with low variability.

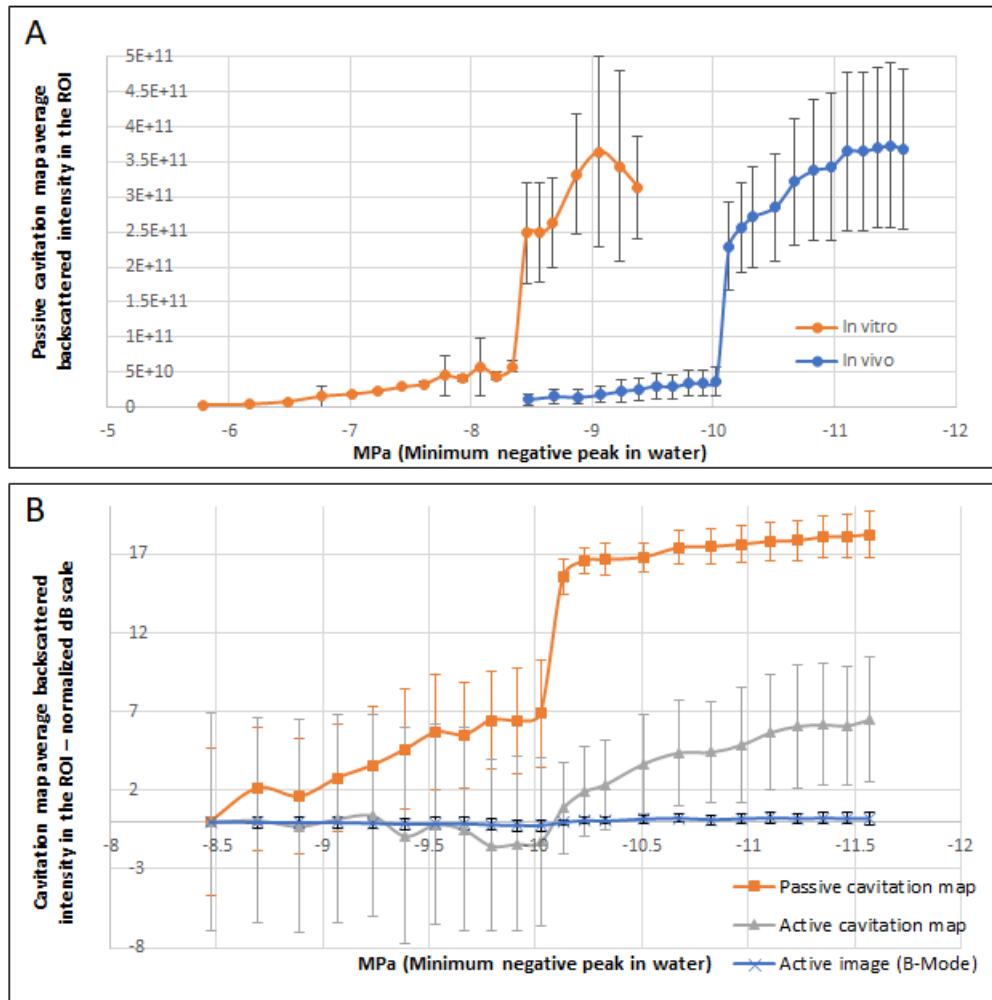


Figure 23 – A) Passive cavitation map Region of Interest (ROI) average backscattered intensity as a function of the estimated minimal focal pressure, in vitro and in vivo
 B) B-Mode, passive cavitation map and active cavitation map normalized dB Region of Interest (ROI) average backscattered intensity as a function of the estimated minimal focal pressure, in vivo
 Error bars show the standard deviation with $n = 30$

We applied the SVD filter for the active and the passive acquisitions *in vivo* while cavitation, and we computed the mean CNR on the obtained cavitation maps for each pig (Figure 24). As we acquired 300 active and passive frames, we could average 30 cavitation maps. We observed that the CNR achieved for the passive acquisitions was significantly higher than the CNR achieved by the active acquisitions for all animals (average CNR of 6.7 ± 0.9 compared to 1.9 ± 1.0 , $p < 0.05$).

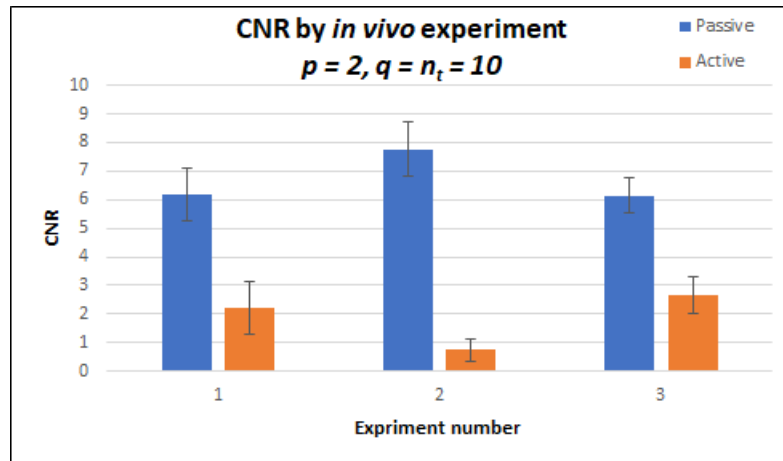


Figure 24 – Contrast-to-Noise Ratio (CNR) of the the active and the passive cavitation maps for each *in vivo* experiment, when $n_t = 10$, $p = 2$, $q = n_t$

Finally, by using the complete monitoring sequence, it is possible to synchronously acquire active and passive images and then to overlay the passive image over the active one, this allowing our goal of precisely locating the bubble cloud in the anatomic structures in real-time. Please find in Figure 25 two overlay examples on different views of the liver. It is possible to see the bubble cloud shape and size evolution.

The passive cavitation imaging behaviour was similar between different parts of the liver (with and without the ribs) and in other pigs. In another study, it could be possible to statistically measure the variability between patients.

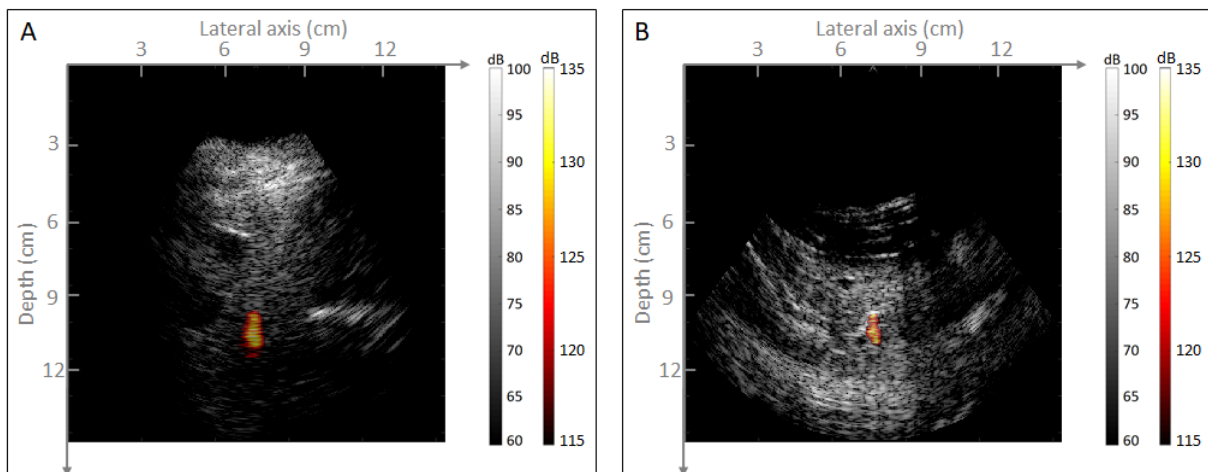


Figure 25 – Monitoring sequence. A and B: Examples of overlays of the cavitation map over the B-Mode, on two different views of the liver

2.4 Axial resolution improvement in coherent passive imaging

2.4.1 Quick Introduction

As presented in 2.2.1 *Theory*, coherent passive imaging takes advantage of the fact that histotripsy pulses are very short. Nevertheless, as for conventional ultrasound imaging, the axial resolution is inversely proportional to the pulse duration [26].

Thus, the more cycles, the longer the pulse and the worst the axial resolution: the passive imaging axial resolution is consequently dependent on the number of cycles per burst. Following the ultrasonic emission parameters and the wanted resolution, this may be critical for monitoring.

We propose an improvement of the coherent passive imaging technique that would allow a good passive imaging axial resolution independently of the number of cycles per burst. The method consists in changing the therapeutic emission sequence by adding an extra cycle after the main ultrasonic burst-wave roundtrip, and to beamform a coherent passive image based only in this last single cycle. The result is theoretically a passive cavitation image with a better resolution as it is beamformed with the smallest possible pulse length. The single cycle event may have a smaller amplitude in order not to interfere with the PCUT sequence nor add unwanted effects.

The disadvantage of the technique is that adding an extra cycle may complexify the electronics (signal generation and amplification stages), and that there is less time for B-Mode imaging between the pulses. However, most of today generators allow an arbitrary waveform generation and the B-Mode frame rate will decrease slightly but not dramatically. Moreover, a loss in the contrast-to-noise ratio is to be expected.

The implementation of this technique would be application-dependent, and following the therapeutic emission parameters and the wanted resolution, not strictly necessary.

For the method validation, we evaluated the theoretical focal spot position and size in simulations using different number of cycles per burst, next we evaluated experimentally the cavitation cloud position and size using different number of cycles per burst and finally we compared this values to the cavitation cloud position and size found using coherent passive

cavitation imaging with and without adding an extra cycle. We performed all our simulations and our *in vitro* experiments in water.

2.4.2 Focal spot size and position in simulations

First, in order to study the theoretical focal spot size and position following the number of cycles, we ran numerical simulations using K-Wave, V 1.1.1, an open-source acoustics toolbox for MATLAB© and C++ [25]. We retrieved mean properties of human tissues from the standard NF EN 60601-2-37 [24] which constitutes the basis of acoustic properties for ultrasonic phantoms and echographers.

We simulated in 2D the acoustic propagation of a histotripsy burst at low pressures in a medium containing water at 30°C, for different number of cycles and using low-pressure linear propagation models. The model consists in a simplified environment containing the therapeutic transducer without the imaging probe. We simulated a mono-element therapy transducer centered at 700 kHz, with a central hole for an imaging probe positioning and having a natural focus at 10 cm, such as the one we used for the *in vitro* experiments described in the next section. The simulation parameters are presented in Figure 26.

| OVERALL PARAMETERS | | |
|------------------------------|--------|------------------------------------|
| Speed of sound | (30°): | $c = 1509 \text{ m/s}$ |
| Density: | | $\rho = 996 \text{ kg/m}^3$ |
| Absorption: | | $\alpha = 0,002 \text{ dB/MHz/cm}$ |
| Non-linearity factor: | | $B/A = 5,2$ |
| Linear model of propagation: | | 1% of gain (170kPa) |
| Temperature: | | 30 °C |

Figure 26 - Simulation parameters for the acoustic propagation of ultrasound using different number of cycles per burst

We simulated bursts composed of 1 to 35 cycles and we measured the focal spot position and dimensions at -3 dB as advised by the standard NF EN 60601-2-37 [24]. Please find the results on Figure 27. The centroid of the focal spot remains in average around 100.2 mm with a low standard deviation of 0.019 mm, which means that the focal spot is not displaced, and its minor and major axis remain globally constant around 1.45 mm and 1.3 mm respectively, except for the one simulated with only one cycle per burst, as with more than one cycle there are wave interferences between the cycles that may interfere with the focusing capabilities.

Chapter II – Passive coherent cavitation imaging

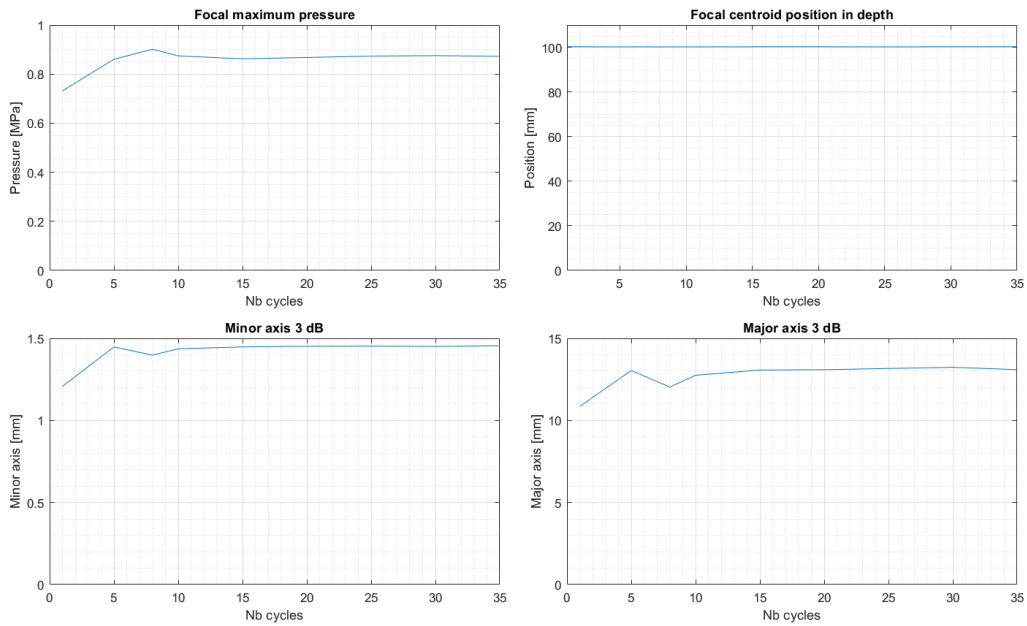


Figure 27 - For different number of cycles:
 Top left: focal spot maximal pressure
 Top right: focal spot centroid position in depth
 Bottom left: focal spot minor axis dimensions at -3 dB
 Bottom right: focal spot major axis dimensions at -3 dB

We may conclude from these results that the position of the focal spot, and consequently the position and size of the cavitation bubble cloud shall remain globally stable at the natural focus independently of the number of cycles. Please find in Figure 28 the maximum of pressure simulation results with bursts made of 1 and 35 cycles.

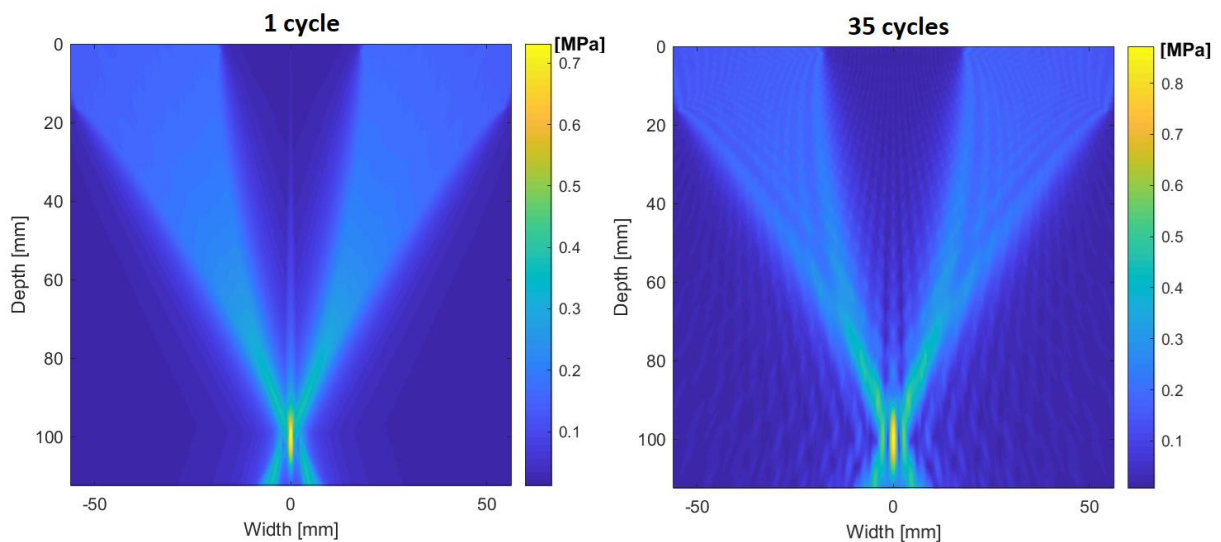


Figure 28 - Simulation results of bursts containing one cycle (left) and 35 cycles (right)

2.4.3 Cavitation cloud size and position using active imaging

We next intended to study the effective cavitation cloud size and position following the number of cycles in degassed water. We based the analysis on the segmentation of active ultrasound cavitation images, taking profit of the fact that the bubble cloud is highly echogenic and it is possible to threshold the image (with a manually set threshold).

We used a 700 kHz focused therapy transducer ($f=100$ mm), (Imasonic[®], France) for high intensity ultrasound emissions, operated by a 2.5 kW power amplifier (RITEC[®], USA). A phased-array imaging ultrasound probe (64 elements, P4-2, Philips[®], USA) was inserted in the central hole of the transducer and both were fixed by a 3D printed support specifically conceived for this probe. The imaging probe for active cavitation cloud size and position evaluation was connected to a programmable US scanner (Vantage 256, Verasonics[®], USA). The therapy transducer driving signal was emitted by a function generator and consisted in a 700 kHz sine burst wave with a pulse repetition frequency (PRF) of 100 Hz. The function generator was also intended as a master clock to trigger both the US scanner and the amplifier gate input. The complete setup is the same as described in Figure 14. As the imaging probe head is at the bottom of the transducer, it shall not interfere with the therapeutic ultrasonic emission path.

We emitted bursts composed of 10 to 40 cycles and we measured the cavitation cloud position and dimensions inside a region of interest. Please find the results on Figure 29. The centroid of the cloud remains in average around 3 cm from the top of the region of interest in depth, and the cloud length and width remain globally constant in average around 1.7 cm and 0.6 cm respectively, with a variability for the length that may be explained by the chaotic behaviour of cavitation.

Chapter II – Passive coherent cavitation imaging

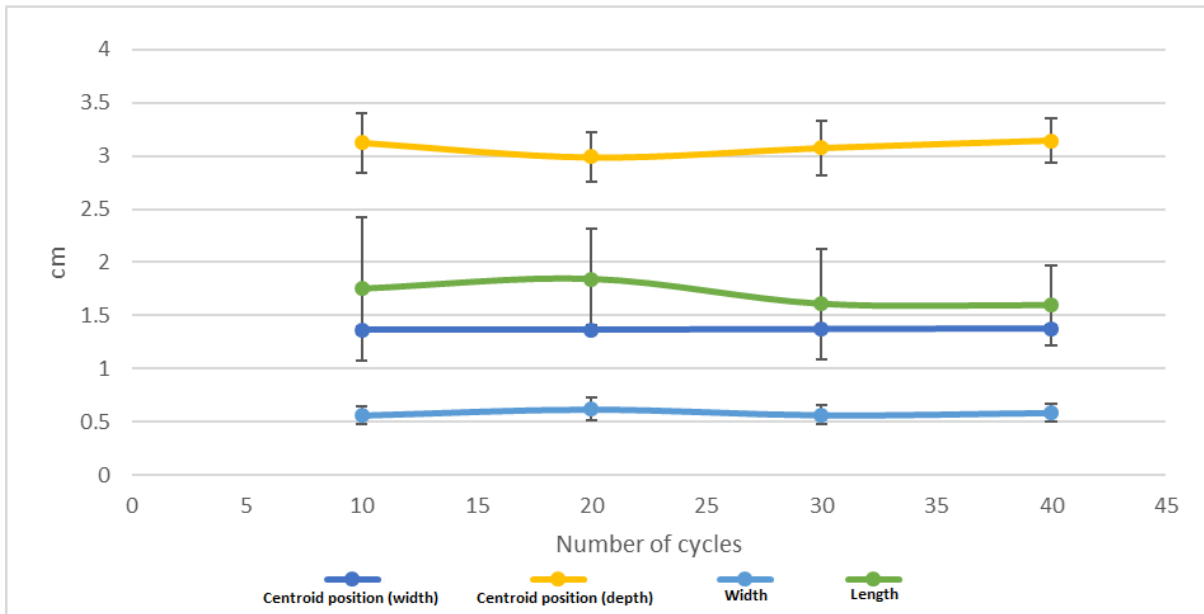


Figure 29 - Cavitation cloud size and position following different number of burst cycles
The positions are relative to a region of interest. N = 100

We experimentally confirmed that the position and size of the cavitation cloud remain globally stable independently of the number of cycles. Please find in Figure 30 examples of active acquisitions for 10, 20, 30 and 40 cycles.

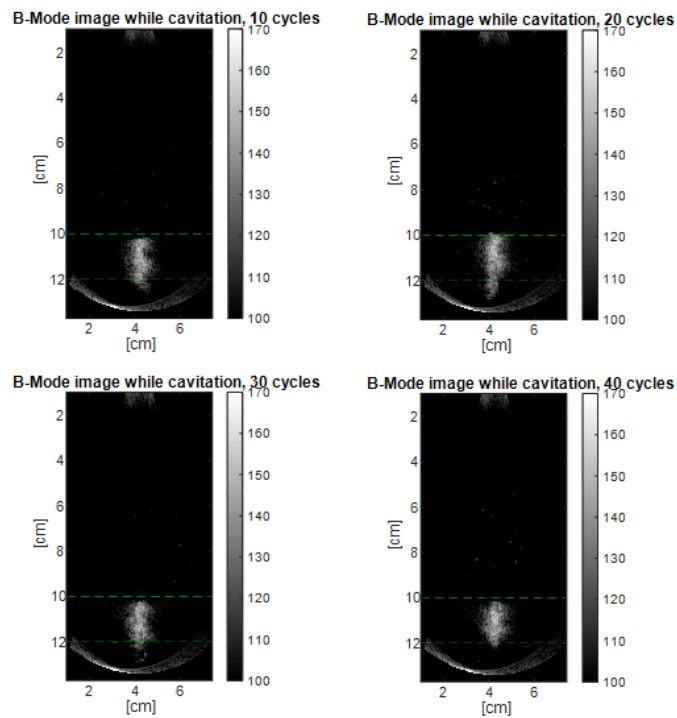


Figure 30 - Results of cavitation imaging.
Top left: 10 cycles Top right: 20 cycles
Bottom left: 30 cycles Bottom right: 40 cycles

2.4.4 Cavitation cloud size and position using coherent passive imaging

By knowing the theoretical and experimental position of cavitation, we finally proceeded to study the effective cavitation cloud size and position following the number of cycles in degassed water using coherent passive imaging. We used the same setup as described in the previous section for cavitation generation.

First, we emitted bursts composed of 5 to 35 cycles without adding an extra cycle: we can observe on Figure 31 that the cavitation cloud appears longer in depth when we increase the number of cycles, confirming that the axial resolution decreases with the number of cycles. However, this is an imaging artifact that does not reflect reality: as we saw in the previous sections, the bubble cloud size shall remain constant.

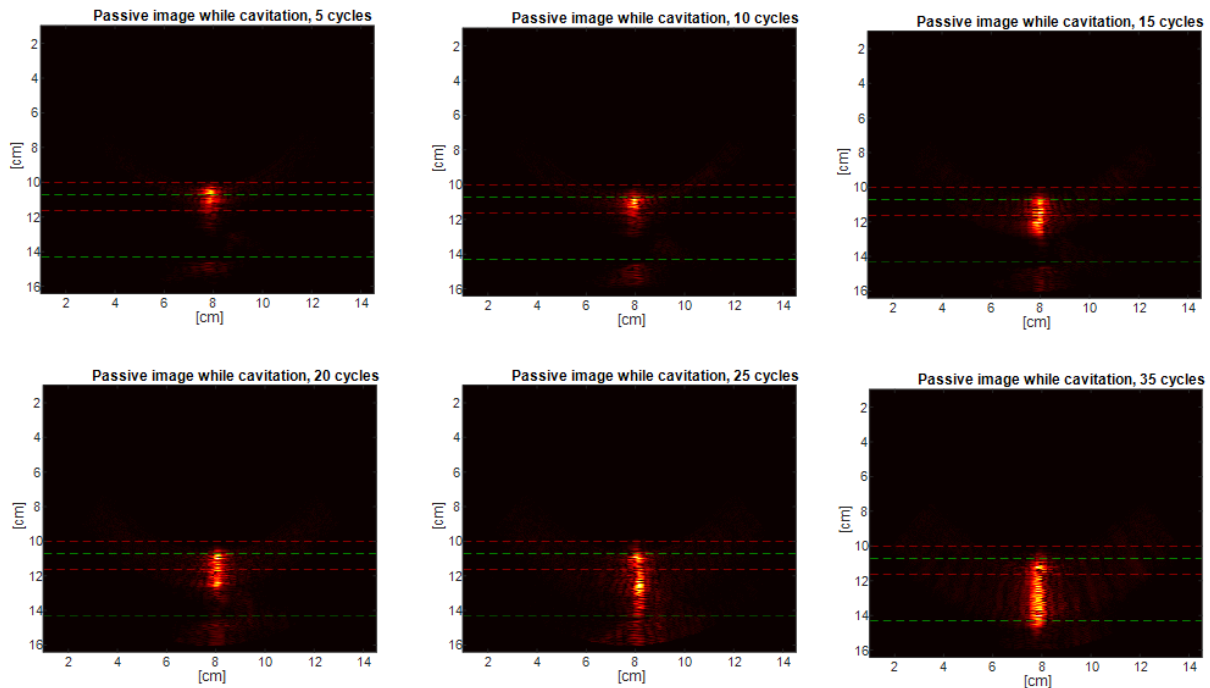


Figure 31 - Coherent passive cavitation imaging for different number of cycles per burst
 We can see that the axial resolution decreases with the number of cycles

As for active imaging, we measured the cavitation cloud position and dimensions inside a region of interest. Please find the results on Figure 32. We observe that the centroid of the cloud moves away from the imaging probe roughly from 2 to 4 cm, and the cloud length increases roughly from 2 to cm 5 cm following the number of cycles.

It is to be noted that the imaging artefact only concerns the axial resolution, and the bubble cloud width remains globally constant in average as well as its position following the

lateral resolution. Moreover, the bubble cloud width measured with passive and active imaging remain comparable between 0.5 and 1 cm.

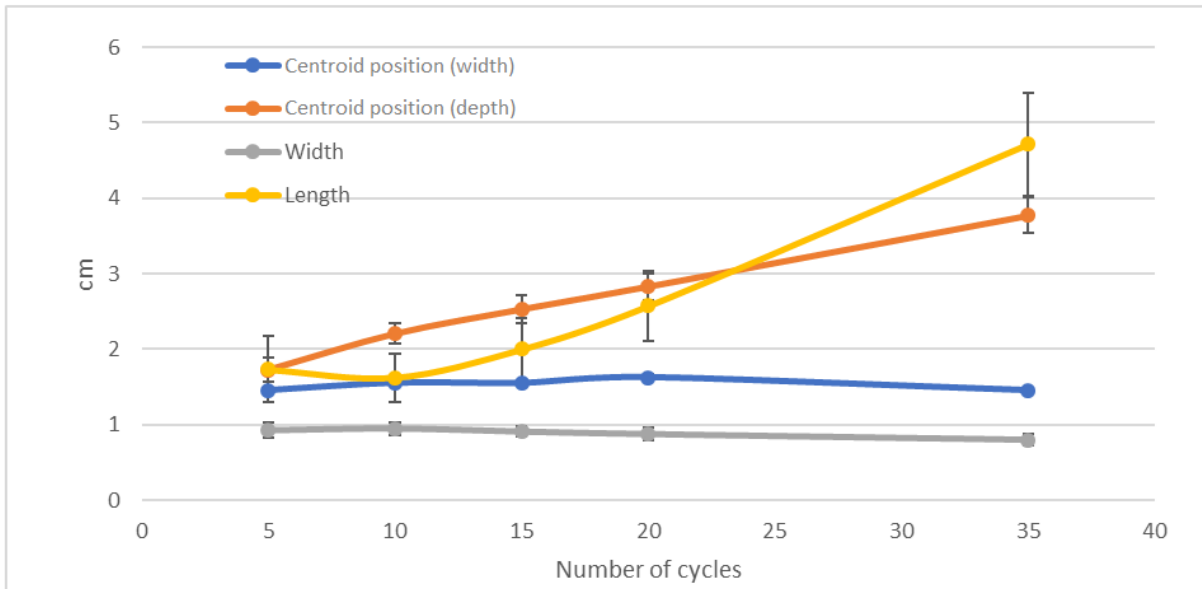


Figure 32 - Cavitation cloud size and position following different number of burst cycles. N = 100
The positions are relative to a region of interest

2.4.5 Cavitation cloud size and position using coherent passive imaging and adding an extra cycle

Secondly, we repeated the same experiment as before but adding an extra cycle 300 μs after the main histotripsy burst. The US scanner is triggered first for passive imaging using the main histotripsy burst, and secondly for passive imaging using the extra cycle so we acquire two images per burst. Please find an example of the emission timings on Figure 33.

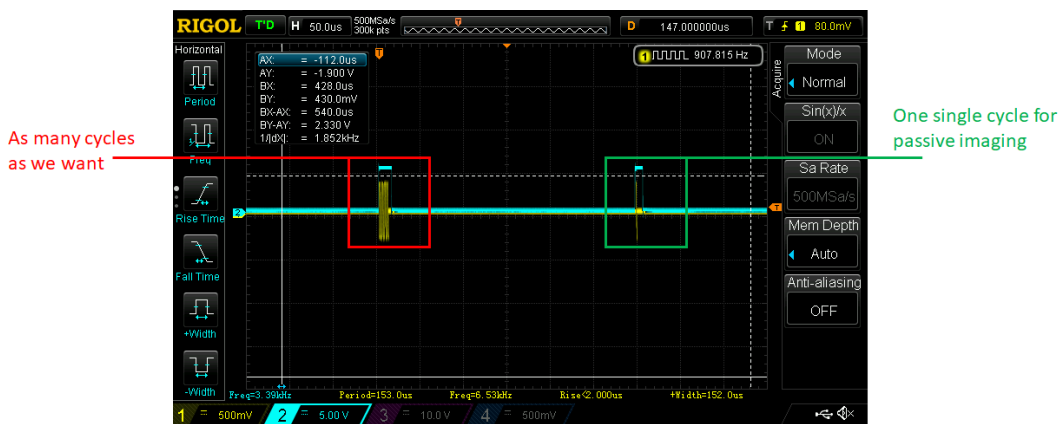


Figure 33 – Timings of the ultrasound emission sequence intended to improve coherent passive imaging resolution while histotripsy
We an extra cycle 300 μs after the main histotripsy burst

Chapter II – Passive coherent cavitation imaging

In Figure 34 we present coherent passive cavitation images of one image taken at the moment of the main burst emission (left) and one image taken at the moment of the extra cycle emission (right) with a main burst of 20 cycles. We can observe that the bubble cloud length is smaller when imaging at the time of the extra cycle for the same therapeutic emission sequence.

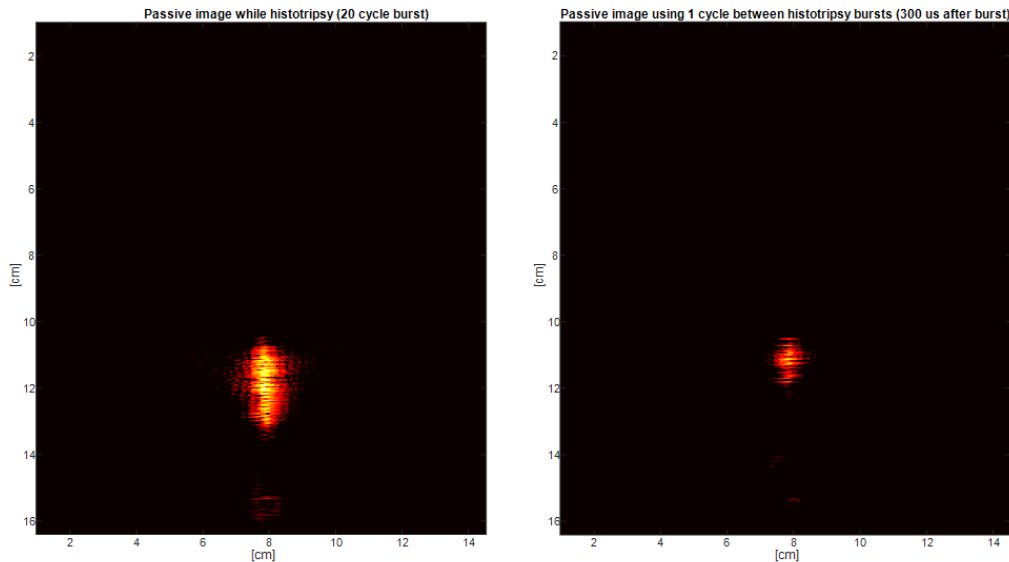


Figure 34 – Left: Passive image while cavitation, 20 cycles
Right: Passive image while cavitation, 20 cycles and an extra cycle

We measured the cavitation cloud position and dimensions inside a region of interest. Please find the results on Figure 35. We observe that the centroid of the cloud slightly moves away from the imaging probe and remains around 3.5 cm, and the cloud length slightly increases from 1 to 1.5 cm following the number of cycles. It is to be noted that cavitation remains a chaotic phenomenon, and other physical effects may occur: the ultrasound interactions with the bubble cloud may change following the acoustic emission power, the propagation media, interfaces, the extra cycle, etc.

The measured bubble cloud width and length remain comparable to the dimensions measured with active imaging: around 1 to 1.5 cm for the length and around 0.5 to 1 cm for the width: we expect intrinsic differences between the three imaging modalities results as images are not taken at the same time. Furthermore, the position along the axial and the lateral directions remain constant following the number of cycles.

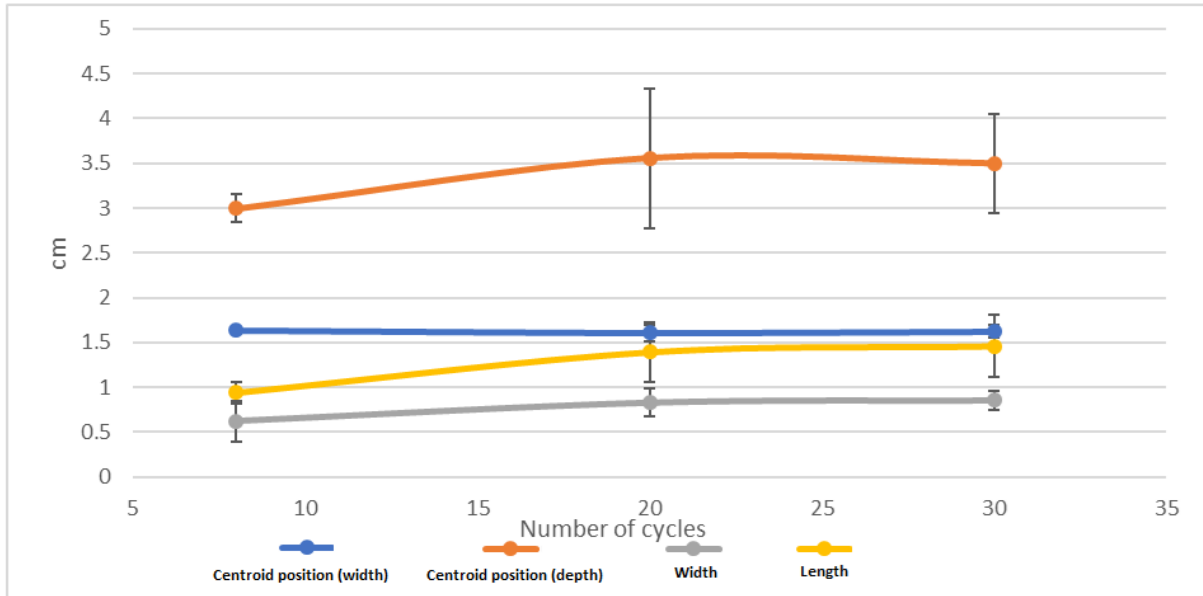


Figure 35 - Cavitation cloud size and position following different number of burst cycles and an extra cycle for passive imaging. N = 100
The positions are relative to a region of interest

Lastly, we evaluated the single-cycle cavitation map CNR and found a decrease by half, around 7 ± 0.8 , compared to the 8-cycled burst presented in 2.3.1 *In vitro experiments*. This is an expected result as there is less backscattered energy from the bubble cloud.

2.4.6 Quick conclusion and discussion

We can conclude that based on our hypothesis and on our results, adding an extra cycle exclusively for imaging allows to improve the axial resolution of coherent passive cavitation imaging despite a loss in contrast, and that we find the same behavior and bubble cloud dimensions as in active cavitation imaging in water.

It is to be noted that in the three imaging modalities (active imaging, passive imaging and passive imaging with an extra cycle), cavitation images are not taken at the same moment. Cavitation cloud dynamics are chaotic, and bubbles evolve very fast, so we can expect intrinsic differences between the three imaging modalities results.

In a future study, it would be interesting to investigate more deeply the effects of adding an extra cycle on the cavitation dynamics.

2.5 Discussion and conclusions

In this study, we proposed a real-time passive imaging method for cavitation mapping of PCUT in moving organs. Our approach relied on the acquisition of a small number of successive backscattered echoes induced by high intensity therapeutic pulses repeated at high frame rate. Thanks to a spatiotemporal filtering approach, high contrast images of cavitation bubbles were obtained. We demonstrated that this technique is highly robust to motion and we showed the *in vivo* feasibility on the liver of a porcine model.

In contrast to other passive cavitation imaging approaches developed for thermal HIFU as in [4] and [8], our method takes advantage of the short high intensity pulses emitted in PCUT. With continuous emissions or long bursts, the beamforming of the received echoes must be performed without the knowledge of the absolute time delays between the emission of the ultrasound wave and the reception on the imaging transducer, resulting in a sub-optimal beamforming as the backscattered intensity is averaged incoherently. As a consequence, the axial resolution of passive cavitation images is strongly reduced compared to what can be achieved with conventional pulse echo ultrasound imaging, and this can be an issue to precisely identify the boundary of the cavitation region [4] [7].

In PCUT applications, however, it is possible to coherently beamform a passive image from the received signals using absolute time delays by synchronizing the receiving imaging array to the therapeutic emission. Delay-and-sum parallel beamforming can be used to reconstruct the passive image. Nevertheless, a time delay correction must be included in the beamforming algorithm in order to compensate the spatial shift between the two arrays [2] [8] [9]. This time delay can be measured as in our study or simply calculated based on the geometry using time of flights or more complex propagation models [9]. It should be noted that the length of the therapeutic pulse affects directly the axial resolution, and the shorter the pulses, the better the spatial resolution. Also, our imaging probe was embedded in the therapy transducer. However, coherent beamforming may be performed using different mechanical configurations, the imaging probe being with a fixed position relative to the transducer.

Another advantage of this approach is that the absolute phase of the backscattered echoes is preserved, which allowed us to discriminate even better the cavitation bubbles echoes from strong scatterers in tissues. Spatiotemporal variations of the echo signals are indeed very different between tissues and bubbles, and the signal of cavitation bubbles is highly localized

with rapid temporal variations as opposed to the backscattered signals of tissues. Ultrafast active ultrasonic imaging using a spatiotemporal singular value decomposition (SVD) was already shown to discriminate the bubble cloud from the tissue [1]. Although this technique enabled to achieve cavitation imaging with a good contrast-to-noise ratio in static tissues, its performances were significantly reduced in moving tissues. Due to the tissue decorrelation while movement, the filtering performances decreased which could be dramatic for monitoring.

We adapted in this work the spatiotemporal filtering already developed for blood flow imaging and active cavitation imaging to passive cavitation imaging. In a static condition, the signals backscattered by the tissues were effectively filtered out using both active and passive cavitation imaging, and our results even showed that active cavitation mapping may perform better than passive cavitation mapping as the CNR reaches a plateau of 18 for active imaging and 15 for passive imaging (Figure 19 B). Active cavitation mapping presents a better image quality due to the coherent compounding, which improves the transmit focusing. In moving tissues, however, tissue signals were filtered out less efficiently from active imaging, and consequently its performance for cavitation mapping was degraded as the CNR decreased to less than 3. In contrast, passive cavitation imaging was much robust to tissue motion, the CNR being around 10 (Figure 19 C). Passive imaging has the advantage over active imaging to benefit directly of the transmitted energy of the therapeutic beam and thus to increase the spatial specificity of the received signals.

The choice of the SVD filtering parameters n_t , p and q is application and sequence dependent. We studied several combinations to investigate the three parameters in our experimental conditions, comparing active and passive, moving and static experiments. Singular value decomposition has been shown as a robust filter to discriminate cavitation bubble clouds from tissue. However, n_t , p and q have to be carefully chosen in order to lose as little cavitation information as possible with a good filtering performance, and there are limitations as the technique needs a minimum number of frames to be robust, which means that the cavitation mapping requires about 100 ms in our experimental conditions (10 acquisitions at a high-power repetition frequency of 100 Hz), and that the temporal resolution depends on the therapeutic burst emission frequency.

We tried classic high-pass filters on the Casorati matrix for cavitation information extraction, but the results were deceiving as the bubble cloud is not as well discriminated from

the tissue. The image source separation is therefore essential and the SVD remains, to our knowledge, the best filter to perform the cavitation mapping.

We also quantified the average backscattered intensity in the cavitation region as a function of the decreasing estimated minimal focal pressure (Figure 23), and we showed that passive cavitation imaging offers a higher sensitivity to the appearance of cavitation than conventional B-Mode imaging or active cavitation imaging. In clinical applications, this result may be useful to precisely locate the cavitation threshold, and to set up a safety procedure for bubble cloud generation. Therefore, this technique could enable to adjust automatically the amplitude of the therapeutic wave emission. The cavitation threshold may be reached automatically, starting from a low emission power and increasing it gradually, and the bubble cloud may be maintained with an automatic control algorithm.

A major advantage of our approach is the possibility to acquire classic B-Mode images between histotripsy pulses, and then to overlay the cavitation mapping over the anatomic structures in real-time this allowing to resolve the exact position of the bubble cloud within the treated tissue.

It is to be pointed that the proposed approach is for abdominal and cardiac applications. In fact, in static conditions or low velocity motion, active imaging could outperform passive imaging.

Lastly, we proposed an improvement of the axial resolution of the technique by adding an extra cycle after the main ultrasonic burst-wave roundtrip, and to beamform a coherent passive image based only this last single cycle emission.

Bibliography

1. Arnal, B, J Baranger, C Demene, M Tanter, and M Pernot. “In Vivo Real-Time Cavitation Imaging in Moving Organs.” *Physics in Medicine and Biology* 62, no. 3 (February 7, 2017): 843–57.
2. Bader, Kenneth B., Kevin J. Haworth, Adam D. Maxwell, and Christy K. Holland. “Post Hoc Analysis of Passive Cavitation Imaging for Classification of Histotripsy-Induced Liquefaction in Vitro.” *IEEE Transactions on Medical Imaging* 37, no. 1 (January 2018): 106–15.
3. Boulos P, Varray F, Poizat A, Azizian Kalkhoran M, Gilles B, Bera J and Cachard C. “Passive cavitation imaging using different advanced beamforming methods”. *IEEE Int. Ultrasonics Symp. (IUS)* (Tours, France, 18–21 September 2016).
4. Coviello, Christian, Richard Kozick, James Choi, Miklós Gyöngy, Carl Jensen, Penny Probert Smith, and Constantin-C. Coussios. “Passive Acoustic Mapping Utilizing Optimal Beamforming in Ultrasound Therapy Monitoring.” *The Journal of the Acoustical Society of America* 137, no. 5 (May 2015): 2573–85.
5. Demene, Charlie, Thomas Deffieux, Mathieu Pernot, Bruno-Felix Osmanski, Valerie Biran, Jean-Luc Gennisson, Lim-Anna Sieu, et al. “Spatiotemporal Clutter Filtering of Ultrafast Ultrasound Data Highly Increases Doppler and FUltrasound Sensitivity.” *IEEE Transactions on Medical Imaging* 34, no. 11 (November 2015): 2271–85.
6. Gateau, Jérôme, Jean-François Aubry, Mathieu Pernot, Mathias Fink, and Mickaël Tanter. “Combined Passive Detection and Ultrafast Active Imaging of Cavitation Events Induced by Short Pulses of High-Intensity Ultrasound.” *IEEE Transactions on Ultrasonics, Ferroelectrics and Frequency Control* 58, no. 3 (March 2011): 517–32.
7. Gyongy, M., and C.-C. Coussios. “Passive Spatial Mapping of Inertial Cavitation During HIFU Exposure.” *IEEE Transactions on Biomedical Engineering* 57, no. 1 (January 2010): 48–56.
8. Haworth, Kevin J., Kenneth B. Bader, Kyle T. Rich, Christy K. Holland, and T. Douglas Mast. “Quantitative Frequency-Domain Passive Cavitation Imaging.” *IEEE Transactions on Ultrasonics, Ferroelectrics, and Frequency Control* 64, no. 1 (January 2017): 177–91.

9. Haworth, Kevin J., T. Douglas Mast, Kirthi Radhakrishnan, Mark T. Burgess, Jonathan A. Kopechek, Shao-Ling Huang, David D. McPherson, and Christy K. Holland. “Passive Imaging with Pulsed Ultrasound Insonations.” *The Journal of the Acoustical Society of America* 132, no. 1 (July 2012): 544–53.
10. Khokhlova, VA, JB Fowlkes, WW Roberts, GR Schade, Z Xu, TD Khokhlova, TL Hall, AD Maxwell, YN Wang, and CA Cain. “Histotripsy Methods in Mechanical Disintegration of Tissue: Toward Clinical Applications.” *International Journal of Hyperthermia: The Official Journal of European Society for Hyperthermic Oncology, North American Hyperthermia Group* 31, no. 2 (March 2015): 145–62.
11. Li, Tong, Hong Chen, Tatiana Khokhlova, Yak-Nam Wang, Wayne Kreider, Xuemei He, and Joo Ha Hwang. “Passive Cavitation Detection during Pulsed HIFU Exposures of Ex Vivo Tissues and In Vivo Mouse Pancreatic Tumors.” *Ultrasound in Medicine & Biology* 40, no. 7 (July 2014): 1523–34.
12. Liu R, Hu H, Xu S, Huo R, Wang S and Wan M. “Ultrafast active cavitation imaging with enhanced cavitation to tissue ratio based on wavelet transform and pulse inversion”. *J. Acoust. Soc. Am.* (2015) 137 3099–106.
13. Marquet, F, J F Aubry, M Pernot, M Fink, and M Tanter. “Optimal Transcostal High-Intensity Focused Ultrasound with Combined Real-Time 3D Movement Tracking and Correction.” *Physics in Medicine and Biology* 56, no. 22 (November 21, 2011): 7061–80.
14. Maxwell, Adam D., Gabe Owens, Hitinder S. Gurm, Kimberly Ives, Daniel D. Myers, and Zhen Xu. “Noninvasive Treatment of Deep Venous Thrombosis Using Pulsed Ultrasound Cavitation Therapy (Histotripsy) in a Porcine Model.” *Journal of Vascular and Interventional Radiology* 22, no. 3 (March 2011): 369–77.
15. McLaughlan J, Rivens I, Leighton T and Ter Haar G. “A study of bubble activity generated in ex vivo tissue by high intensity focused ultrasound.” *Ultrasound Med. Biol.* (2010) 36 1327–44
16. Royer, D., N. Dubois, and M. Fink. “Optical Probing of Pulsed, Focused Ultrasonic Fields Using a Heterodyne Interferometer.” *Applied Physics Letters* 61, no. 2 (July 13, 1992): 153–55.
17. Schuster, Timothy G., John T. Wei, Kari Hendlin, Russell Jahnke, and William W. Roberts. “Histotripsy Treatment of Benign Prostatic Enlargement Using the Vortx R x System: Initial Human Safety and Efficacy Outcomes.” *Urology* 114 (April 2018): 184–87.

18. Tanter, Mickael, and Mathias Fink. “Ultrafast Imaging in Biomedical Ultrasound.” *IEEE Transactions on Ultrasonics, Ferroelectrics, and Frequency Control* 61, no. 1 (January 2014): 102–19.
19. Villemain, Olivier, Justine Robin, Alain Bel, Wojciech Kwiecinski, Patrick Bruneval, Bastien Arnal, Mathieu Rémond, Mickael Tanter, Emmanuel Messas, and Mathieu Pernot. “Pulsed Cavitation Ultrasound Softening.” *JACC: Basic to Translational Science* 2, no. 4 (August 2017): 372–83.
20. Vlaisavljevich, Eli, Gabe Owens, Jonathan Lundt, Dejan Teofilovic, Kimberly Ives, Alexander Duryea, Jim Bertolina, Theodore H. Welling, and Zhen Xu. “Non-Invasive Liver Ablation Using Histotripsy: Preclinical Safety Study in an In Vivo Porcine Model.” *Ultrasound in Medicine & Biology* 43, no. 6 (2017): 1237–51.
21. Xu, Z., G. Owens, D. Gordon, C. Cain, and A. Ludomirsky. “Noninvasive Creation of an Atrial Septal Defect by Histotripsy in a Canine Model.” *Circulation* 121, no. 6 (February 16, 2010): 742–49.
22. Zhen Xu, M. Raghavan, T.L. Hall, Ching-Wei Chang, M.-A. Mycek, J.B. Fowlkes, and C.A. Cain. “High Speed Imaging of Bubble Clouds Generated in Pulsed Ultrasound Cavitation Therapy - Histotripsy.” *IEEE Transactions on Ultrasonics, Ferroelectrics and Frequency Control* 54, no. 10 (October 2007): 2091–2101.
23. Chen, Wen-Shiang, Andrew A. Brayman, Thomas J. Matula, Lawrence A. Crum, and Morton W. Miller. “The Pulse Length-Dependence of Inertial Cavitation Dose and Hemolysis.” *Ultrasound in Medicine & Biology* 29, no. 5 (May 2003): 739–48.
24. NF EN 60601-2-37/A1 :2015-11:2008-04. Medical electrical equipment - Part 2-37: Particular requirements for the basic safety and essential performance of ultrasonic medical diagnostic and monitoring (IEC 60601-2-37:2007)
25. <http://www.k-wave.org>
26. Ng, Alexander, and Justiaan Swanevelder. “Resolution in Ultrasound Imaging.” *Continuing Education in Anaesthesia, Critical Care and Pain* 11, no. 5 (October 1, 2011): 186–92. <https://doi.org/10.1093/bjaceaccp/mkr030>
27. PCT/EP2019/063455 : Appareil de traitement par ultrasons comportant des moyens d'imagerie des bulles de cavitation / Ultrasonic treatment apparatus comprising means for imaging cavitation bubbles

Chapter III - From 2D to 3D cavitation imaging

Special thanks to Victor Finel, who taught me the secrets of the 3D machine.

Some of the results were presented in a proceedings paper of the 2019 International Ultrasonic Symposium (Glasgow): “Real-time monitoring of pulsed cavitation ultrasound therapy using coherent passive cavitation imaging: perspectives for volumetric imaging”.

3.1 Introduction

Histotripsy is currently guided mostly by ultrasound imaging, which allows a visualization of the anatomic structures and the bubble cloud inside a two-dimensional imaging plane. For now, 2D cavitation imaging allows to beamform a 2D slice of the bubble cloud, which leads to an overview of its size, shape and location.

From a technical point of view, conventional B-Mode imaging imposes the cavitation cloud to be inside the imaging plane. There is an engineering challenge to precisely interlock the imaging probe and the therapy transducer, and to maintain the position during the whole procedure. A misalignment between both transducers could lead to a misfire and cavitation would be nucleated outside the imaging plane. Moreover, independently from the pure mechanical alignment, in very complex and aberrating mediums, ultrasound beams could be distorted and nucleation could also happen out-of-plane.

In these cases, the non-visualization of the bubble cloud could result in a critical security risk for the patient as the physician would not have information about the cavitation's absence cause (cavitation threshold not reached, mechanical misalignment, aberration...).

Furthermore, in water and in simple and homogenic mediums, the cavitation cloud is mainly symmetrical with an oval or circular shape, and 2D imaging gives enough information of the cloud dynamics, shape and position. However, in more complex mediums (c.f. *in vivo*) and in mediums presenting strong interfaces (c.f. the ribs, calcifications), the bubble cloud shape and size may vary in random asymmetrical ways, as presented in Figure 36 showing histotripsy *in vitro* over a bioprosthetic aortic valve.

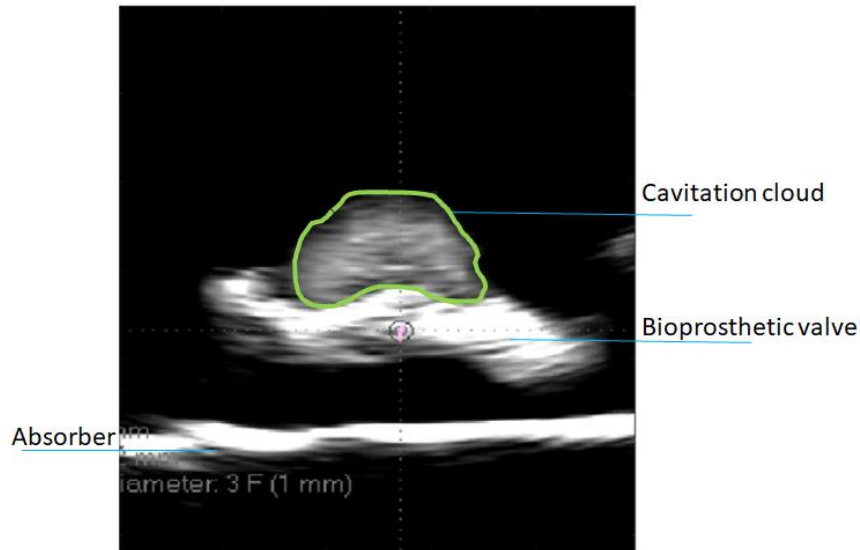


Figure 36 – B-Mode image of histotripsy over a bioprosthetic valve
The bubble cloud, outlined in green, presents an asymmetrical shape

Cavitation is a three-dimensional phenomenon, and a 2D monitoring is limited in the way that we can only supervise a slice of the cloud, ignoring its full shape and thus the possible target tissues around a three-dimensional volume surrounding the focal spot.

We propose to explore the next step of histotripsy monitoring, consisting in the development of a 3D imaging method allowing to image the entire anatomic sonicated volume. 3D imaging would allow to image the whole cavitation cloud, even if it is located outside the central axis of the therapeutic transducer. For this purpose, using a customized 1024 ultrasound system coupled to a matrix probe, we tested the feasibility of our complete 2D cavitation monitoring sequence *in vitro* now in 3D, including passive coherent cavitation imaging and active B-Mode imaging.

To this day, ultrasound 3D systems used in clinics are still limited in frame rate and image quality [5][6], and ultrasound systems allowing a good frame rate and image quality are rather closed, expensive or for now reserved to the research world.

3.2 3D passive coherent imaging and spatiotemporal filter

3.2.1 Experimental setup

Coherent passive imaging is based on the acquisition of the therapeutic emission backscattered echoes by an imaging probe. Yet, the therapeutic emission is in fact a three-

dimensional cone, and by using a matrix probe it is possible to beamform a volumetric image of this ultrasound field. The 2D method described in *Chapter II - Passive coherent cavitation imaging* is therefore theoretically extendable to 3D by using a system capable to acquire all the elements of the matrix probe at once (or at least in a way allowing to beamform a coherent image [1]).

We used a customized, programmable, 1024-channel ultrasound system composed of 4 synchronized Vantage systems set up to drive a 32x32 matrix array centered at 3 MHz (Vermon©, France). The 1024 independent channels could be used simultaneously in transmission and reception. The probe was inserted in the central hole of the transducer and was fixed by a specially conceived 3D printed support. We used the same set up as for 2D cavitation detection in *Chapter II - Passive coherent cavitation imaging* and we performed the same *in vitro* analysis (Figure 17).

For B-Mode acquisitions, we compounded 16 steered divergent waves to form a volume per therapeutic burst with a PRF of 1000 Hz. The sources were placed forming a virtual array behind the probe as described by [1] starting at $(x, y) = (-1.3, -1.3)$ mm, with a step of 0.7 mm in both directions and with a distance to the virtual apex of 5 mm. The effective B-Mode volume rate was around 60 Hz.

For passive acquisitions, as in 2D imaging, volumes were beamformed as if a single wave had been transmitted by the probe, following a delay-and-sum beamforming. We used a CUDA optimized delay-and-sum algorithm incorporating absolute timing information and each volume was reconstructed in real-time after 250 μ s of data was received. We needed one histotripsy pulse per volume and the effective frame rate was 100 Hz.

The time-delay correction allowing the compensation of the spatial shift between the therapy transducer and the imaging probe was directly included in the beamforming algorithm. The time-delay was experimentally measured prior to the experiment in a water tank using a hydrophone placed at the focal point. The time delay was the difference of the arrival time of the signals emitted by the therapeutic transducer and by the imaging probe when focusing on the hydrophone.

3.2.2 Results

We computed the contrast-to-noise ratio (CNR) as presented in 2.2.5 *Cavitation map evaluation* for different sets of combinations of the parameters n_t , p and q during static and moving experiments. For each sequence we acquired 200 volumes during histotripsy, and we applied in post-processing the SVD filter using different n_t , p and q combinations.

As shown on Figure 38, the bubble cloud was imaged successfully in 3D *in vitro*. In order to compare 2D and 3D passive cavitation imaging performances, we evaluated the CNR of the 3D passive acquisitions in static and moving conditions. As for 2D acquisitions, we fixed n_t at 6, 10 and 14 frames and we investigated the dependence of the CNR with p and q .

The CNR was found slightly lower in 3D than in 2D (Figure 37 B, Figure 19 B), which can be explained by the smaller aperture of the matrix probe. We observed that the CNR is maximal roughly when $p = 3$ and $q = n_t$ (Figure 37 A). Compared to 2D results, the dependence with p was however less marked. We also compared the influence of n_t when $p = 2$ and $q = n_t$ (Figure 37 B), and we observed that the curve follows a logarithmic evolution and reaches a plateau globally after $n_t = 15$ volumes.

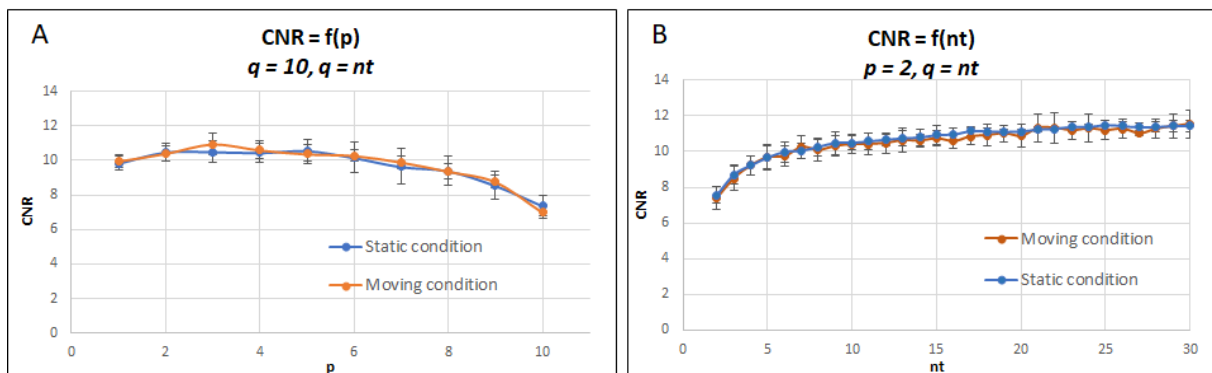


Figure 37 - 3D *in vitro* passive cavitation map Contrast-to-Noise Ratio (CNR) evaluation while cavitation

A) CNR as a function of p when $n_t=10$, $q=10$

B) CNR as a function of n_t when $p=2$, $q=n_t$

The behavior of the CNR following p , q and n_t remains similar between 2D and 3D acquisitions, and the SVD performances allow to compute a volumetric cavitation map with no contribution from the tissue. Moreover, in contrast with the 2D results, there was no significant CNR decrease between static and moving experiments in 3D. This result highlights the

robustness of 3D imaging compared to 2D imaging which suffers of decorrelation effect along the elevation direction.

Please find an example of a passive 3D cavitation map over the B-Mode with $n_t = 10$, $p = 2$ and $q = n_t$ presented with two orthogonal planes of the volume and a 3D volume rendering in Figure 38.

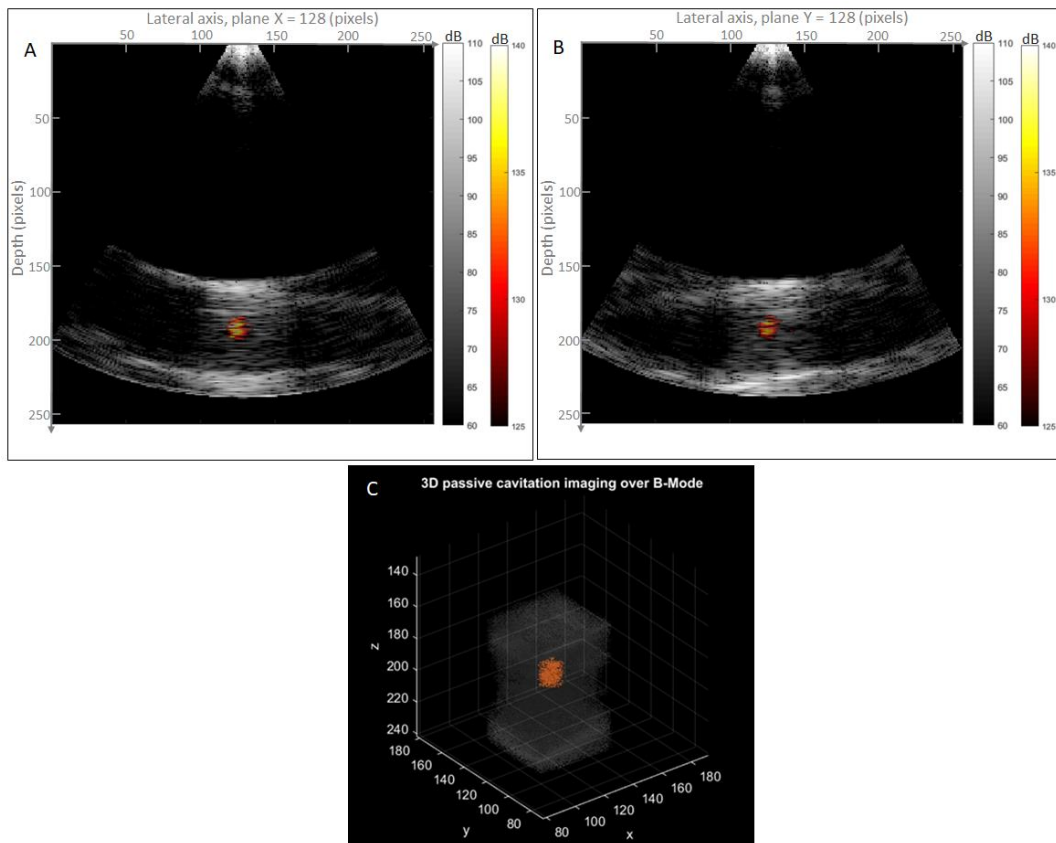


Figure 38 - 3D passive cavitation map over volumetric B-Mode

A: Plane X = 128/256. B: Plane Y = 128/256. C: 3D rendering

The voxel size is 0.7 mm x 0.7 mm x 0.7 mm

3.3 Measurement of ultrasonic attenuation through a swine thorax

3.3.1 Objective and methods

In the previous section, we proved the feasibility of 3D passive cavitation imaging *in vitro* in a tissue mimicking phantom. Next, we intended to get closer to the *in vivo* preclinical

procedure by putting *ex vivo* ribs between the transducer and the focus. Ribs, skin and fatty tissues add attenuation to the medium, and may induce a therapeutic beam aberration.

Furthermore, as ribs are highly absorptive, skin burns and subcostal oedema have been reported in clinical HIFU liver ablation cases [11]. In histotripsy, nevertheless, as the emission duty cycle is very small, the heating effects are minimized along the propagation path [12]. Respiration-induced motion also significantly compromises the treatment precision and efficacy, which enhances the need for an accurate real-time monitoring.

First, attenuation is a critical parameter to the procedure efficacy as the focal pressure should be sufficient to enable bubble nucleation for inertial cavitation. We started by measuring the global ultrasonic attenuation of the ribs (without the skin) and of thoracic tissues (ribs and skin) of a swine model (~55kg).

Thoracic tissues were explanted from a swine model after sacrifice. The skin was removed, and the sample was placed in the freezer 2 hours after explantation. The day before the measurement, the sample was unfrozen in the fridge for 24 hours. The sample was placed in saline water and degassed for 1 hour. The sample and saline water was placed in a sealed plastic bag under vacuum. Thoracic tissues were then explanted with the skin intact from 3 other and the preparation was similar to the one described above.

We used a 700 MHz focused therapy transducer ($f=100$ mm, $f/D = 1$), (Imasonic[®], France) operated by a 2.5 kW power amplifier (RITEC[®], USA) driven in turn by a function generator. A hydrophone (Onda[®], HNC 400) connected to an amplifier and a scope was used to measure the pressure at the focus. The hydrophone was moved by a 3D step motor stage, was placed at the focus of the transducer and the pressure was measured with and without the thoracic tissue inserted between the transducer and the hydrophone. We drove measures at emission frequencies of 700 and 800 kHz. Please find in Figure 39 a photo of the setup.

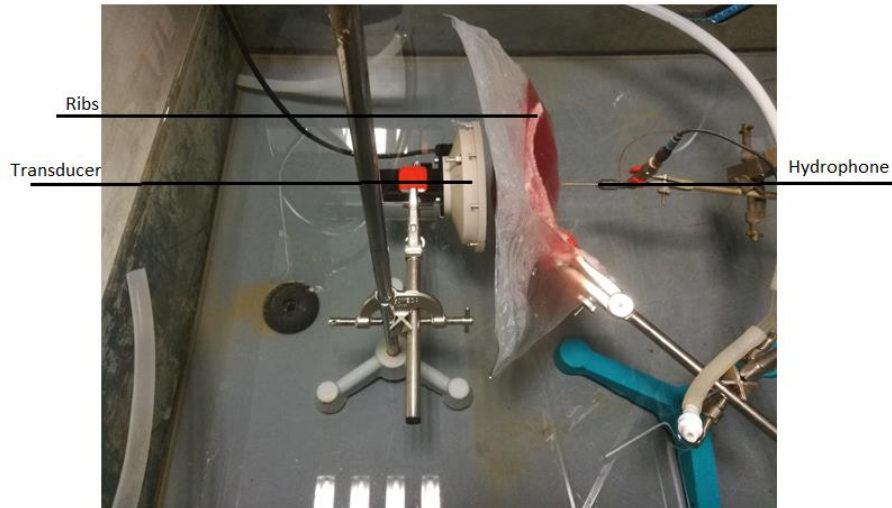


Figure 39 - Setup for ultrasonic attenuation measurement through the ribs of a swine model

The attenuation coefficient of the ribs was computed by removing the measured attenuation of the plastic bag and using the estimated attenuation of the soft tissues ($\alpha=0.5\text{dB/cm/MHz}$). Next, the pressure measured at the hydrophone was corrected by the transmission coefficient of soft tissues:

$$t_{\text{tissue}} = 10^{-\alpha \cdot h \cdot f} \quad (10)$$

3.3.2 Results

Please find in Table 1 the attenuation measurement results at an emission frequency of 700 kHz.

Table 1 - Attenuation measurements to the ribs of 4 swine. Emission frequency: 700 kHz, N = 5

| | Attenuation (%) | Corrected attenuation (%) | Average thickness (mm) |
|--------------------------|-------------------|---------------------------|------------------------|
| Swine 1 (no skin) | 52.37 ± 10.83 | 46.89 ± 12.07 | 27 |
| Swine 2 | 56.69 ± 9.77 | 49.53 ± 11.39 | 38 |
| Swine 3 | 83.97 ± 8.48 | 80.07 ± 10.54 | 54 |
| Swine 4 | 62.27 ± 15.12 | 55.13 ± 17.98 | 43 |

At 700 kHz, the mean total attenuation was estimated at $52 \pm 11\%$ without the skin and at $67 \pm 14\%$ with the skin, and the attenuation coefficient of the ribs was estimated at $\alpha_{\text{ribs}} = 58 \pm 15\%$.

Please find in Table 2 the attenuation measurement results at an emission frequency of 800 kHz.

Chapter III – From 2D to 3D cavitation imaging

Table 2 - Attenuation measurements to the ribs of 4 swine. Emission frequency: 800 kHz, N = 5

| | Attenuation (%) | Corrected attenuation (%) | Average thickness (mm) |
|--------------------------|-----------------|---------------------------|------------------------|
| Swine 1 (no skin) | 58.63 ± 9.05 | 53.15 ± 10.24 | 27 |
| Swine 2 | 63.60 ± 7.04 | 56.64 ± 8.39 | 38 |
| Swine 3 | 88.56 ± 6.64 | 85.32 ± 8.51 | 54 |
| Swine 4 | 67.17 ± 15.12 | 55.13 ± 17.98 | 43 |

At 800 kHz, the mean total attenuation was estimated at $59 \pm 9\%$ without the skin and at $73 \pm 13\%$ with the skin, and the attenuation coefficient of the ribs was estimated at $\alpha_{\text{ribs}} = 64 \pm 15\%$.

3.4 Cavitation monitoring of an aberrated beam

3.4.1 Introduction

Inertial cavitation in histotripsy is ensured by the high-intensity ultrasound emission from a transducer. Ultrasound is focused at a specific focal spot (geometrically and/or electronically) and the strong negative pressures at this spot will cause bubbles to nucleate.

However, if the propagation medium is heterogenic, and in particular if it contains strong reflectors or strong interfaces such as the ribs or fatty tissues, the therapeutic ultrasound field can be aberrated and:

- The focal spot shape can be distorted;
- The focal spot can be displaced from its intended position;
- Secondary focal spots can be created, leading to secondary cavitation clouds nucleation.

2D ultrasound monitoring is based on the imaging of the cavitation cloud inside a single plane. However, if the therapeutic emission field is aberrated:

- The cavitation cloud could be displaced outside the imaging plane;
- Secondary cavitation clouds could nucleate outside the imaging plane.

Impeding the visualization of the cloud(s). 2D imaging would not be able to ensure the procedure monitoring in these extreme cases. It should be noted that we assume that strong aberrations affect mainly the therapeutic beam due to the large aperture of the therapeutic

transducer, whereas the imaging probe has a limited dimension and is located in an intercostal space with no ribs on the ultrasound path.

The effects of aberrating mediums such as of the ribcage the skull have been widely explored on HIFU emissions [8][10], especially the decrease on the necrosis efficacy and misfiring, and aberration correction solutions using for example adaptive focusing have been proposed [7]. For histotripsy through the ribcage, some studies show that there is no strict need for aberration correction [9], and our preclinical trials as presented confirm these results as well.

We intend to study the cavitation cloud position when emitting ultrasound through an aberrating medium (here, human ribs) and to push the emission power to create secondary cavitation clouds, and to put on perspective 2D and 3D imaging modalities.

3.4.2 Setup and methods

We used a 700 kHz focused therapy transducer ($f = 100$ mm), (Imasonic[®], France) for high intensity ultrasound emissions, operated by a 2.5 kW power amplifier (RITEC[®], USA). We used a phased-array imaging ultrasound probe (64 elements, P4-2, Philips[®], USA) for 2D imaging and a 32x32 matrix array (Vermon[®], France) for 3D imaging. Both probes were inserted in the central hole of the transducer and both were fixed by specifically conceived 3D printed supports. The therapy transducer driving signal was emitted by a function generator and consisted in a 700 kHz 8-cycle sine burst wave with a pulse repetition frequency (PRF) of 100 Hz.

We placed 3 human ribs in front of the transducer to create an aberration on the therapeutic field. We did not block the imaging probes to allow a proper imaging, as shown in Figure 40. It is to be noted that this configuration is similar to the *in vivo* therapeutic procedure, where the phased array probe is placed between the intercostal spaces.

The imaging probes used for active and passive cavitation cloud size and position evaluation were connected:

- In 2D, to a programmable US scanner (Vantage 256, Verasonics[®], USA). The complete setup is the same as described in Figure 14;
- In 3D, to a customized, programmable, 1024-channel ultrasound system composed of 4 synchronized Vantage systems.

The function generator was also intended as a master clock to trigger both the US scanner and the amplifier gate input.

Finally, we based the cavitation analysis on the image processing segmentation of cavitation images, taking profit of the fact than the bubble cloud is highly echogenic and it is possible to threshold the image with a manually set threshold.



Figure 40 - Human ribs placed in front of the therapeutic transducer to create an aberration
The imaging fields in front of the probes are not aberrated,
Left: P4-2 phased array (Philips®, USA)
Right: 32x32 matrix array (Vermon©, France)

3.4.3 Back to 2D imaging

In an aberrating medium, the therapeutic focal spot could be displaced outside the imaging plane. Yet, it is to be pointed out that besides the pure acoustic propagation, there are other possible reasons why the cavitation cloud might be outside the imaging plane. For example, in our experiments, the imaging probe and the therapeutic transducer are physically fixed by a 3D printed support. Nevertheless, there might be imprecisions on the printing and/or the fixations, and both transducers may not be perfectly aligned, as shown in Figure 62. This kind of problematic will be more extensively addressed on *Chapter V - Focal spot three-dimensional position monitoring challenges*.

First, we drove cavitation experiments in degassed water. Please find on Figure 41 the result of cavitation imaging using three imaging modalities: a) conventional B-Mode, b) active cavitation imaging and c) passive cavitation imaging. We used the three imaging modalities to compare the imaging capabilities.

Chapter III – From 2D to 3D cavitation imaging

We computed the cavitation cloud centroid position in relation to the central axis of the image, which we assume corresponds in theory to the central axis of the transducer along the imaging plane. It is to be noted that this is a strong assumption, and a more complex setup using a hydrophone could be used to quantitatively measure the focal spot position (at low pressures) in relation to the imaging plane. Indeed, as pointed out previously, we may expect imprecisions due to the mechanical alignment between the imaging probe and the therapy transducer. Moreover, it is to be reminded that, in the three imaging modalities, cavitation images are not taken at the same moment: cavitation cloud dynamics are chaotic, and bubbles evolve very fast, so we can expect intrinsic differences between the modalities results. Please find in Table 3 the results.

Table 3 – Distance of the centroid of the cavitation cloud to the central axis of the image, for B-Mode, active and passive cavitation imaging. N = 100

| Imaging modality | Distance to the central axis of the image in width (cm) |
|----------------------------|---|
| B-Mode | 0.17 ± 0.022 |
| Active cavitation imaging | 0.16 ± 0.01 |
| Passive cavitation imaging | 0.1 ± 0.26 |

We found in the three modalities that the cavitation cloud centroid remains centered around the central axis of the image with a precision inferior to 2 mm. We may assume that the focal spot, which is plausibly distorted, is not dramatically displaced by the human ribs' aberration. This result is interesting as we can expect a similar behavior in the clinical procedure.

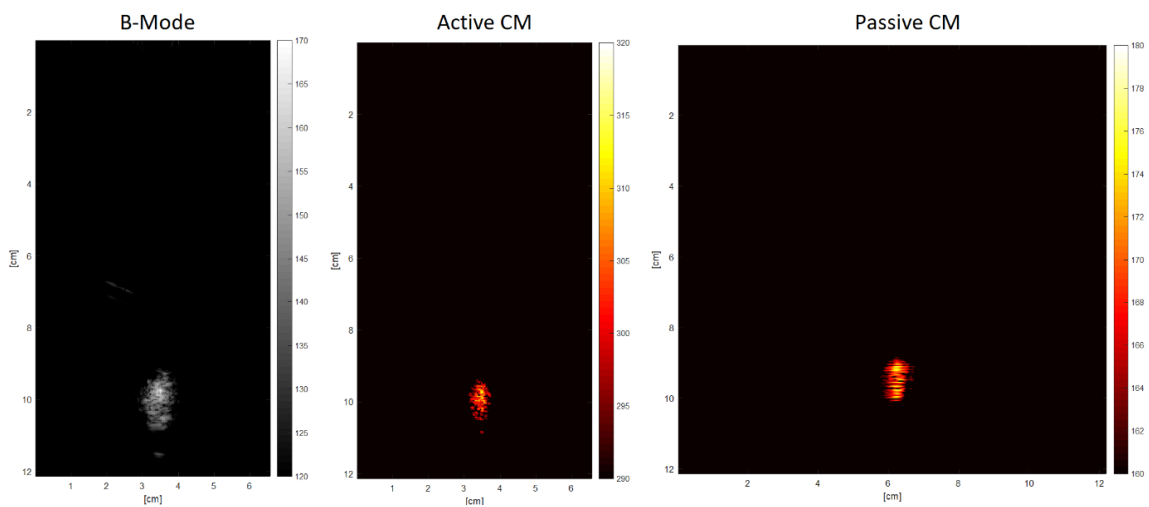


Figure 41 - Histotripsy in water while emitting trough human ribs
a) B-Mode

Chapter III – From 2D to 3D cavitation imaging

- b) Active cavitation map (CM)
- c) Passive cavitation map (CM)

Next, we drove cavitation experiments in degassed water but pushing the emission power above the natural cavitation threshold at the focus, for an estimated minimal focal pressure peak value under -18 MPa. The objective of this kind of experiment was to reach the cavitation threshold at the side lobes thus creating secondary cavitation clouds.

Please find on Figure 42 the B-Mode images of the experiment while histotripsy through the ribs, where we can observe frame by frame the nucleation of a second cavitation cloud. The estimated frame rate is 30 frames per second. The secondary cloud is quickly driven by the ultrasound path and fuses with the main cavitation cloud. As a consequence, the main cloud shape and size are altered.

Secondary cavitation clouds represent a safety risk for the patient as unwanted tissues may be targeted.

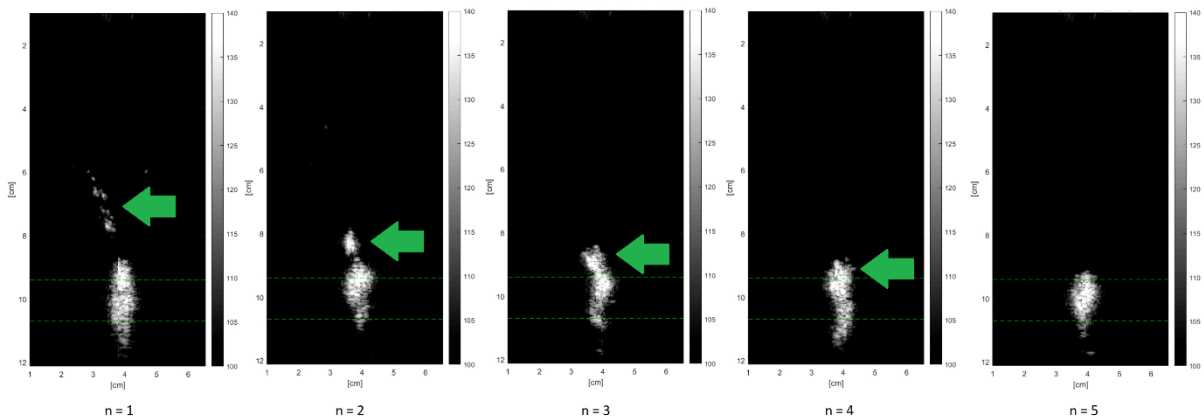


Figure 42 - B-Mode of histotripsy through human ribs in degassed water
From left to right, we can appreciate frame by frame a second cavitation cloud nucleation, pointed by the green arrow, that will join the main cavitation cloud
Estimated imaging frame rate: 20 frames per second

In this particular case, 2D cavitation allows us to visualize the second nucleated cavitation cloud and to follow its size, shape and dynamics. However, as the therapeutic emission field is tridimensional, we cannot know if there are other focus outside the plane.

Finally, this is indeed an extreme case in histotripsy, unlikely to happen in clinics as we are commonly around the cavitation threshold. Nevertheless, 3D imaging could allow us to overcome this kind of questions, as well as the mechanical fixation imprecisions, and to monitor the procedure in a whole volume with less safety risks.

3.4.4 Cavitation monitoring using 3D imaging

First of all, we drove cavitation experiments in degassed water to qualitatively study the tridimensional shape of the cavitation cloud after the ribs' aberration. We used coherent passive imaging as it has a better CNR in 3D cavitation imaging.

Please find in Figure 43 two orthogonal X and Y planes of an acquired volume while histotripsy. Please find in Table 4 the results of the width, length and cavitation cloud centroid position in relation to the central axis of the image, which we assume corresponds in theory to the central axis of the transducer.

Table 4 – Three-dimensional dimensions of the cavitation cloud and distance to the central axis of the transducer, using 3D coherent passive cavitation imaging. N = 80

| | X plane | Y plane |
|---|-----------------|-----------------|
| Width (cm) | 1.34 ± 0.1 | 1.3 ± 0.1 |
| Length (cm) | 1.6 ± 0.08 | 1.54 ± 0.13 |
| Distance to the central axis of the transducer (cm) | 0.18 ± 0.02 | 0.01 ± 0.01 |

As for 2D imaging, the cavitation cloud centroid remains centered around the central axis of the image with a precision inferior to 2 mm in the X plane and inferior to 0.2 mm in the Y plane. We may confirm, now in 3D, that the focal spot, which is plausibly distorted, is not dramatically displaced by the human ribs' aberration.

Moreover, we can observe that the bubble cloud is roughly symmetrical in the X and Y planes with a width around 1.3 cm and a length around 1.6 cm, and the shape of the cloud remains roughly spherical.

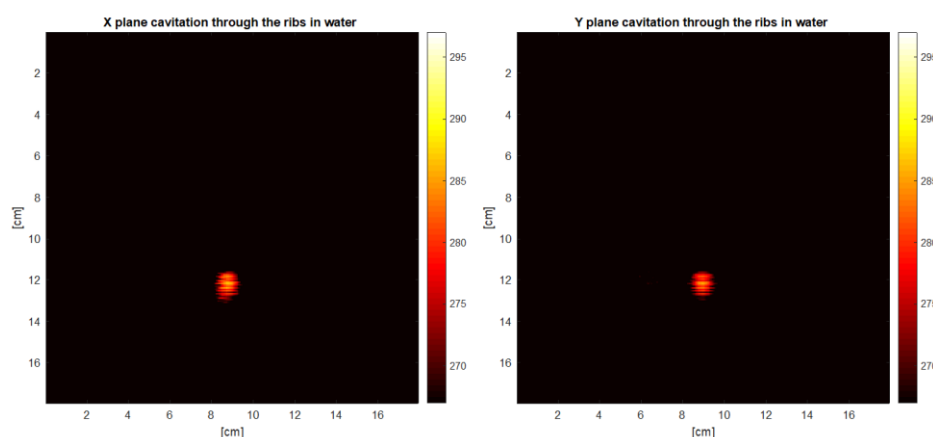


Figure 43 - 3D passive cavitation map while histotripsy through human ribs in degassed water
Left: Plane X = 128/256. Right: Plane Y = 128/256

Next, we drove cavitation experiments in degassed water and pushing the emission power above the cavitation threshold, for an estimated minimal focal pressure peak value under -18 MPa. Figure 44 shows two orthogonal X and Y planes of an acquired volume while histotripsy. In the X plane we can observe inside the blue circle a secondary cavitation cloud (as in 2D imaging), however, it is absent in the Y plane.

Indeed, the secondary cavitation cloud happens to be off center, and this outside the Y plane. We can imagine that 2D imaging would be limiting in such a case. Furthermore, the 3D rendering shows us that there is only one secondary cavitation cloud.

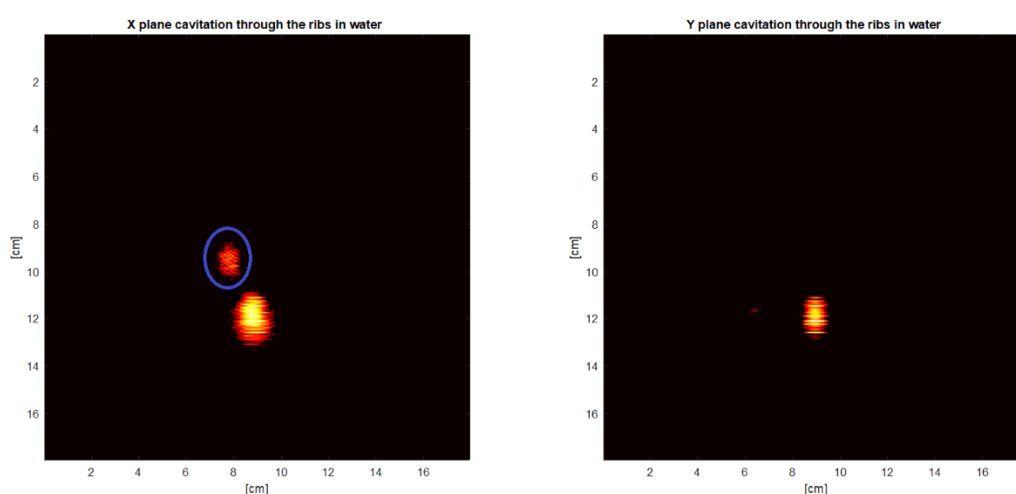


Figure 44 –3D passive cavitation map while histotripsy through human ribs in degassed water
 Left: Plane X = 128/256. We can observe inside the blue circle a second cavitation cloud
 Right: Plane Y = 128/256

We can conclude of this experience that 3D imaging allows a safer monitoring of the histotripsy procedure, by covering a whole volume where cavitation can occur.

3.4.5 Cavitation cloud three-dimensional shape

Secondly, we wanted to qualitatively study in 3D the cavitation cloud shape while histotripsy over a calcified aortic valve leaflet. In fact, as shown in Figure 36, the bubble cloud may take random asymmetrical shapes depending on the target anatomy. We drove histotripsy experiments while cavitation in degassed water and over a human calcified aortic valve leaflet, as shown in Figure 45. The goal of this experiment was to highlight the importance of knowing the whole shape of the bubble cloud, as a single imaging plane may not give enough information.

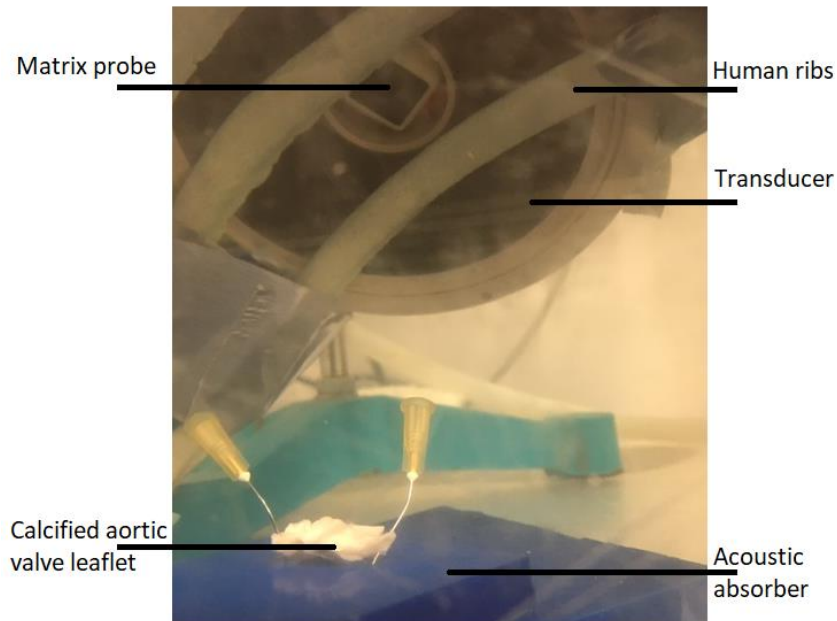


Figure 45 - Human ribs placed in front of the therapeutic transducer to create an aberration
The imaging field in front of the 32x32 matrix array (Vermon©, France) is not aberrated
The transducer is placed to generate cavitation over a human calcified aortic valve leaflet

Please find in Figure 46 a) the B-Mode of the experimental setup, showing the absorber and the leaflet, which are tilted in the imaging plane, and in Figure 46 b) and c) two orthogonal X and Y planes of an acquired volume while histotripsy over the leaflet. We expect the cavitation cloud to be asymmetrical, and the cavitation image to be tilted on at least one plane, following the leaflet's shape and positioning.

Indeed, in the X plane we can observe that the bubble cloud follows the shape of the leaflet (tilted on the imaging plane), while in the Y plane we do not find this tilt. Therefore, the shape of the cloud is here different following the visualization plane. This phenomenon is not necessarily linked to the ribs' aberration, but to the target shape.

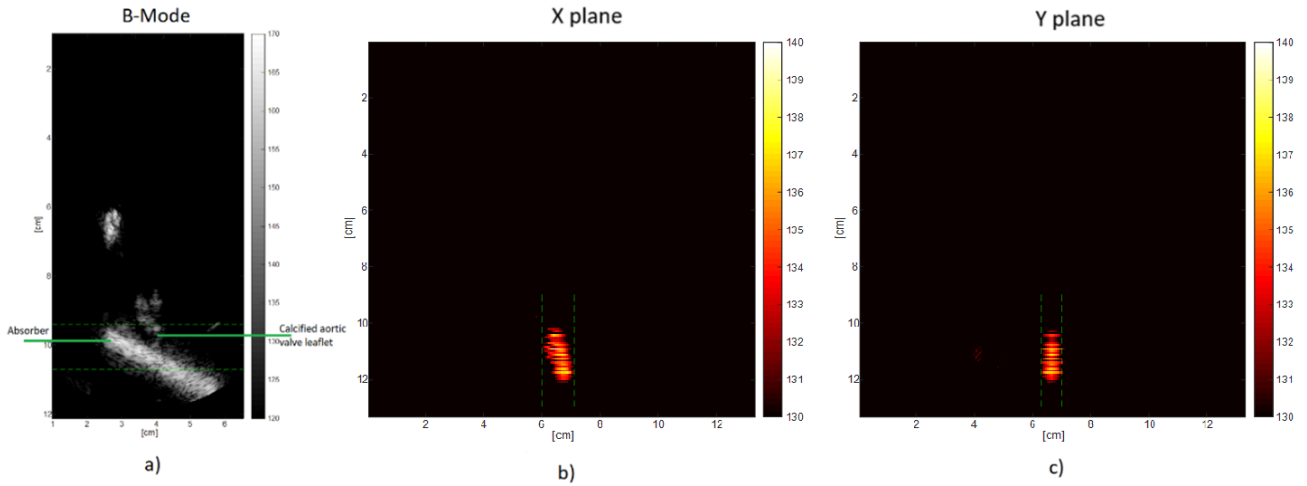


Figure 46 – Histotripsy through human ribs over a calcified human aortic valve leaflet
 a): B-Mode
 b), c): 3D passive cavitation map
 b): Plane X = 128/256. C): Plane Y = 128/256

We can conclude of this experience that 3D imaging gives full information to visualize the complete shape of the bubble cloud and thus the complete treated area, which may vary following the target shapes.

It is to be pointed out nonetheless that a 3D rendering may be hard and long to interpret during a therapeutic procedure, and in practice we commonly plot orthogonal X and Y planes. This is equivalent to a bi-plane imaging modality. Please find in Figure 47 an example of the monitoring results using one plane and using two orthogonal X and Y planes (bi-plane imaging). Two orthogonal planes may give a sufficient overview of the cloud full shape.

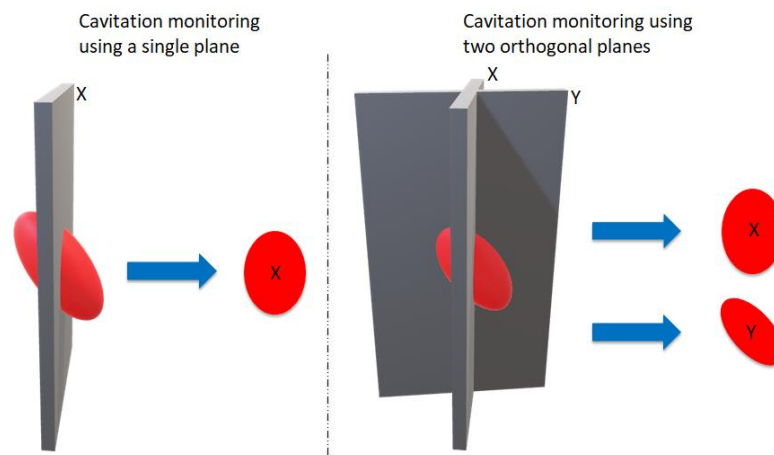


Figure 47 – Scheme: red: cavitation cloud, grey: Imaging plane
 Left: cavitation monitoring using a single plane
 Right: cavitation monitoring using two orthogonal X and Y planes
 The shape of the bubble cloud vary following the imaging plane position

3.5 Discussion and conclusion

We demonstrated the feasibility of volumetric coherent passive cavitation imaging as the algorithms are easily transposed to 3D applications. Volumetric coherent passive cavitation imaging required however more computation time and an effective volume rate of 1 volumes/s was achieved. 3D passive cavitation imaging could increase the safety of the treatment monitoring as cavitation is a tridimensional phenomenon, and the whole bubble cloud could be precisely located within a volume.

In fact, 2D imaging may be limited as the mechanical alignment of the imaging probe and the therapy transducer should be ensured, and as the emission and propagation medium characteristics may aberrate and even displace the therapeutic focal spot outside the imaging plane.

As the cavitation cloud shape may be asymmetrical, and secondary cavitation clouds may nucleate following the propagation medium properties and the target mechanical shape and characteristics, 3D cavitation imaging may overcome 2D imaging limits.

However, heavy electronics are needed for full 3D imaging, and machines providing a good rendering with a clinical frame rate are either closed, expensive or still far from a clinical application. At this day, clinical 3D cardiac imaging systems exist (General Electric©, Philips©), and cavitation imaging could be implemented in those systems.

Finally, despite its great potential, today 3D imaging is mostly seen as complementary to 2D imaging in routine practice [5]. The visualization and the interpretation of a full 3D volume while histotripsy may remain long and complicated, and ergonomic tests as well as the reaction time measure should be driven. For now, a simple bi-plane imaging would be interesting for a more complete monitoring without complexifying much more the electronics.

Bibliography

1. Provost, Jean, Clement Papadacci, Juan Esteban Arango, Marion Imbault, Mathias Fink, Jean-Luc Gennisson, Mickael Tanter, and Mathieu Pernot. “3D Ultrafast Ultrasound Imaging *in Vivo*.” *Physics in Medicine and Biology* 59, no. 19 (October 7, 2014): L1–13.
2. Flesch, M, M Pernot, J Provost, G Ferin, A Nguyen-Dinh, M Tanter, and T Deffieux. “4D *in Vivo* Ultrafast Ultrasound Imaging Using a Row-Column Addressed Matrix and Coherently-Compounded Orthogonal Plane Waves.” *Physics in Medicine and Biology* 62, no. 11 (June 7, 2017): 4571–88.
3. Sauvage, J, M Flesch, G Férin, A Nguyen-Dinh, J Porée, M Tanter, M Pernot, and T Deffieux. “A Large Aperture Row Column Addressed Probe for *in Vivo* 4D Ultrafast Doppler Ultrasound Imaging.” *Physics in Medicine & Biology* 63, no. 21 (October 24, 2018): 215012
4. Morton, CE, and Lockwood G R. “Theoretical assessment of a crossed electrode 2-D array for 3-D imaging”. *IEEE Symp. on Ultrasonics*, vol 1 pp 968–71 (2003).
5. Lang, R. M., L. P. Badano, W. Tsang, D. H. Adams, E. Agricola, T. Buck, F. F. Faletra, et al. “EAE/ASE Recommendations for Image Acquisition and Display Using Three-Dimensional Echocardiography.” *European Heart Journal - Cardiovascular Imaging* 13, no. 1 (January 1, 2012): 1–46. <https://doi.org/10.1093/ehjci/jer316>.
6. Wu, Victor Chien-Chia, and Masaaki Takeuchi. “Three-Dimensional Echocardiography: Current Status and Real-Life Applications.” *Acta Cardiol Sin*, n.d., 12. (2017)
7. Cochard, E., J. F. Aubry, M. Tanter, and C. Prada. “Adaptive Projection Method Applied to Three-Dimensional Ultrasonic Focusing and Steering through the Ribs.” *The Journal of the Acoustical Society of America* 130, no. 2 (August 2011): 716–23. <https://doi.org/10.1121/1.3607419>.
8. Li, Faqi. “Effect of Ribs in HIFU Beam Path on Formation of Coagulative Necrosis in Goat Liver.” In *AIP Conference Proceedings*, 829:477–80. Boston, Massachusetts (USA): AIP, 2006. <https://doi.org/10.1063/1.2205520>.
9. Kim, Y, E Vlaisavljevich, G E Owens, S P Allen, C A Cain, and Z Xu. “*In Vivo* Transcostal Histotripsy Therapy without Aberration Correction.” *Physics in*

Medicine and Biology 59, no. 11 (June 7, 2014): 2553–68.
<https://doi.org/10.1088/0031-9155/59/11/2553>.

10. Dervishi, E., J.-F. Aubry, J.-Y. Delattre, and A.-L. Boch. “La thérapie par ultrasons focalisés : état actuel et applications potentielles en neurochirurgie.” *Neurochirurgie* 59, no. 6 (December 2013): 201–9. <https://doi.org/10.1016/j.neuchi.2013.06.005>.
11. Jung, Seung Eun, Se Hyun Cho, Jin Hee Jang, and Joon-Yeol Han. “High-Intensity Focused Ultrasound Ablation in Hepatic and Pancreatic Cancer: Complications.” *Abdominal Imaging* 36, no. 2 (April 1, 2011): 185–95. <https://doi.org/10.1007/s00261-010-9628-2>.
12. Khokhlova, VA, JB Fowlkes, WW Roberts, GR Schade, Z Xu, TD Khokhlova, TL Hall, AD Maxwell, YN Wang, and CA Cain. “Histotripsy Methods in Mechanical Disintegration of Tissue: Toward Clinical Applications.” *International Journal of Hyperthermia : The Official Journal of European Society for Hyperthermic Oncology, North American Hyperthermia Group* 31, no. 2 (March 2015): 145–62.

Chapter IV - From 2D to bi-plane imaging

Special thanks to Jinjing Xia, who strongly contributed to the PAXY probe conception, simulations, manufacturing and testing.

4.5 Introduction

Histotripsy is a non-invasive therapeutic procedure that takes advantage of the mechanical action of inertial cavitation bubbles. As doctors do not have a direct visual feedback of the bubbles target range, ultrasound is commonly used to monitor the therapy. Monitoring requires the maximum possible information allowing to ensure the safety of the procedure. However, ultrasound B-Mode imaging only allows the visualization inside a two-dimensional plane, and the volume outside this plane remains unmonitored.

As we saw in 3.4.4 *Cavitation monitoring using 3D imaging*, 3D imaging seems promising to image the whole sonicated volume, but remains expensive or the image quality is not yet sufficient. We concluded that a good compromise between cost, image quality, frame rate and monitored volume would be a bi-plane imaging sequence.

Bi-plane imaging consists of using a probe that has at least two orthogonal piezoelectric arrays allowing to image two orthogonal planes one after the other, for a perpendicular visualization of a region of interest. The concept was introduced in the late 1980's and was widely explored in the 1990's for transoesophageal echocardiographic applications [8][9]. In fact, bi-plane imaging increases the visualization area, decreases the user's manipulations and allows to faster retrieve information for diagnosis despite a loss of half the frame rate. The design and shape as well as the acoustic performances of such probes were widely explored [10], and nowadays bi-plane probes are commonly endocavitary probes used in applications such as obstetrics, gynaecology or urology [7].

For our project, we intended to set a bi-plane probe for external cardiac applications. We considered the PAXY probe (Vermon©, France), centred at 2.8 MHz and including two sets of 64 orthogonal elements, and adapted for cardiac applications. By driving one array, the probe can perform 2D imaging like a conventional transducer, and the other array can also be driven to perform an image in the perpendicular direction. A limitation of this probe, however, is the lack of an acoustic lens that is usually present on the output of conventional probes to

focus the energy along each slice and improve the elevation resolution. Therefore, without elevation focusing, a thick 2D slice would be imaged and the resulting imaging quality would be lower than with a conventional cardiac phased array. To overcome this limitation, we propose to add a lens to restore the focusing in the two perpendicular planes. As this lens should be cylindrical in the two orthogonal directions, we propose a spherical lens.

The challenge consisted in adding a convex cylindrical acoustic lens to allow the focalization in both X and Y directions, and on the design of a proper beamforming algorithm allowing to have a sufficient frame rate for monitoring. In fact, the spherical lens imposes a beamforming correction as we need to restore a cylindrical focusing in each plane, and it has a different speed of sound than biological tissues. We designed, manufactured and tested the probe with the new lens, presented on Figure 48.

For imaging and to achieve a maximum frame rate for monitoring, we set up a delay-and-sum beamforming algorithm using a “thin lens correction” based on ultrafast imaging. We tested the performances against a “complete” beamforming algorithm and evaluated the cavitation imaging capabilities.

It is to be noted that as it is required to beamform two images, the frame rate is divided by two compared to a conventional B-Mode imaging.



Figure 48 - PAXY probe including a convex cylindrical acoustic lens

In a further study, row-column addressed probes having also two orthogonal piezoelectric arrays but with wider elements (for a large active surface) could lead to volumetric imaging with the same electronics as for conventional bi-plane imaging [6].

4.6 Beamforming methods

4.6.1 Complete ultrafast delay-and-sum beamforming

Basic ultrafast ultrasound imaging on cardiac arrays is founded on the emission of one divergent wave (or more for compounding), the reception of all the backscattered echoes by all the piezoelectric elements at the same time and finally the delay-and-sum beamforming of the image [1][2].

A divergent wave is theoretically emitted from a virtual source S behind the piezoelectric array, and the wave virtually propagates in the medium. In practice, the piezoelectric elements start the ultrasound emission following the delay law resulting from the virtual source position.

The complete delay-and-sum beamforming is based on the computation of the delays between the first ultrasound emission and the reception of the echoes from each point in the imaging plane grid.

More in detail, for each grid point, the delay may be divided in:

- The forward delay (FD), which is the delay between the first ultrasonic emission on the array and the grid point;
- The backward delay (BD), which is the delay between the grid point and each one of the elements.

Thus, for each grid point, we have one FD and as many BD as piezoelectric elements. The signals from each piezoelectric element are next added in phase and assigned to a pixel value. Please find a scheme of the beamforming actors in Figure 49.

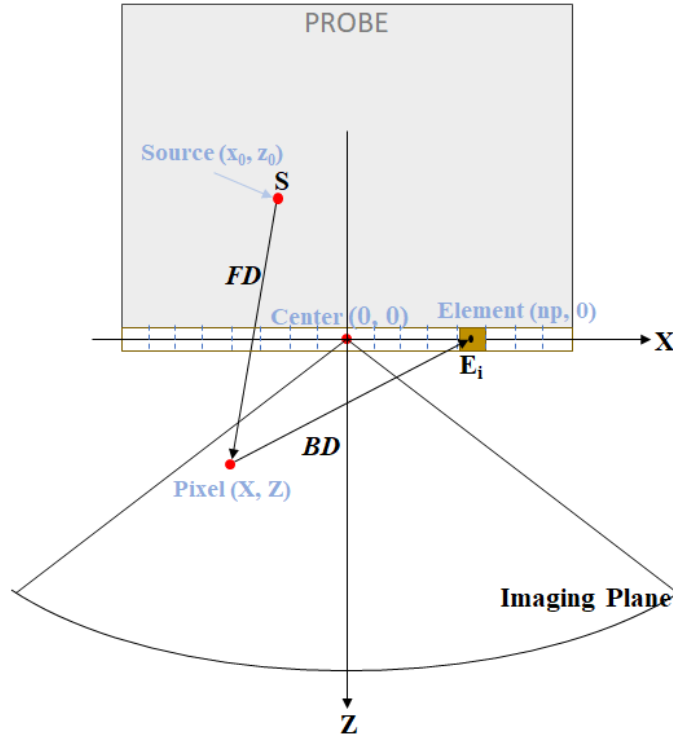


Figure 49 - Complete image beamforming (with no acoustic lens)

We have:

$$FD = \frac{d(S, Pixel) - z_0}{c_0}$$

$$BD = \frac{d(Pixel, E_i)}{c_0}$$

Where c_0 represents the speed of sound in the medium (i.e. 1540 m/s in human tissues) and E_i represents an element of the piezoelectric array. It is to be noted that z_0 represents the shortest distance between the source S and the piezoelectric array, and therefore z_0/c_0 represents the delay from the first ultrasound emission.

4.6.2 Complete delay-and-sum beamforming with an acoustic spherical lens

Now, let us add the spherical convex acoustic lens on the scheme as shown in Figure 50. The lens is characterized by a radius R and a maximum thickness h . It is made of silicon and its speed of sound is $c_1 = 1015$ m/s. A first approximation consists in ignoring the refraction between the lens and the sonicated medium.

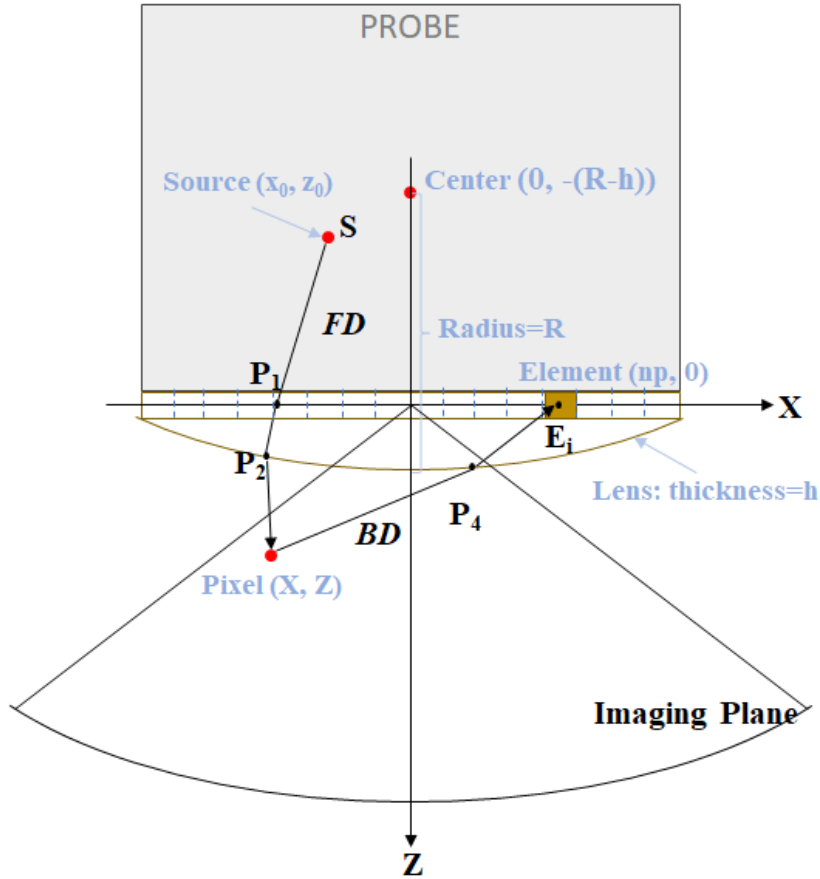


Figure 50 - Complete imaging beamforming with an acoustic lens

If we effectively ignore the refractive index, we have:

$$FD = \frac{d(S, P_1)}{c_0} + \frac{d(P_1, P_2)}{c_1} + \frac{d(P_2, Pixel)}{c_0} - \frac{z_0}{c_0}$$

$$BD = \frac{d(Pixel, P_4)}{c_0} + \frac{d(P_4, E_i)}{c_1}$$

For each grid point, it is necessary to compute the position of P_2 for the FD and the position of each P_4 for each BD following the lens geometry. We implemented the full computation of FD and BD for each pixel of the image and optimized the beamforming in CUDA. However, these additional computations make the beamforming slow at around **7 frames/second**, which is not optimal for the heart monitoring.

Following our specific constraints in cardiac imaging, we intended to develop a beamforming method allowing a compromise between image quality and frame rate such as the thin lens approximation algorithm.

4.6.3 Thin lens approximation for delay-and-sum beamforming

At an emission frequency of 2.8 MHz, the ultrasound wavelength in biological tissues is around 0.55 mm. As the lens thickness (maximum thickness $h = 0.6$ mm) is in average small in relation to this wavelength, we implemented a beamforming algorithm using a thin lens approximation paradigm [4] for improving the frame rate. It consists in assuming that the lens has a constant thickness $h[np]$ in front of each piezoelectric element. Thus, we do not have to compute for each grid point the P_2 and P_4 positions, but we use constant values (Figure 51). This kind of correction, usually assumed in optics, may induce errors in the short field but is consistent in the far field. We are close to the assumption limit, but we intended to test the beamforming capabilities and the image quality.

Moreover, in order to achieve a slightly higher frame rate, this beamforming algorithm may include another approximation by ignoring the FD correction, as if there was no lens. In practice, we compute the FD and the BD as if there was no lens, and we simply add a constant delay $\delta[np]$ for each BD:

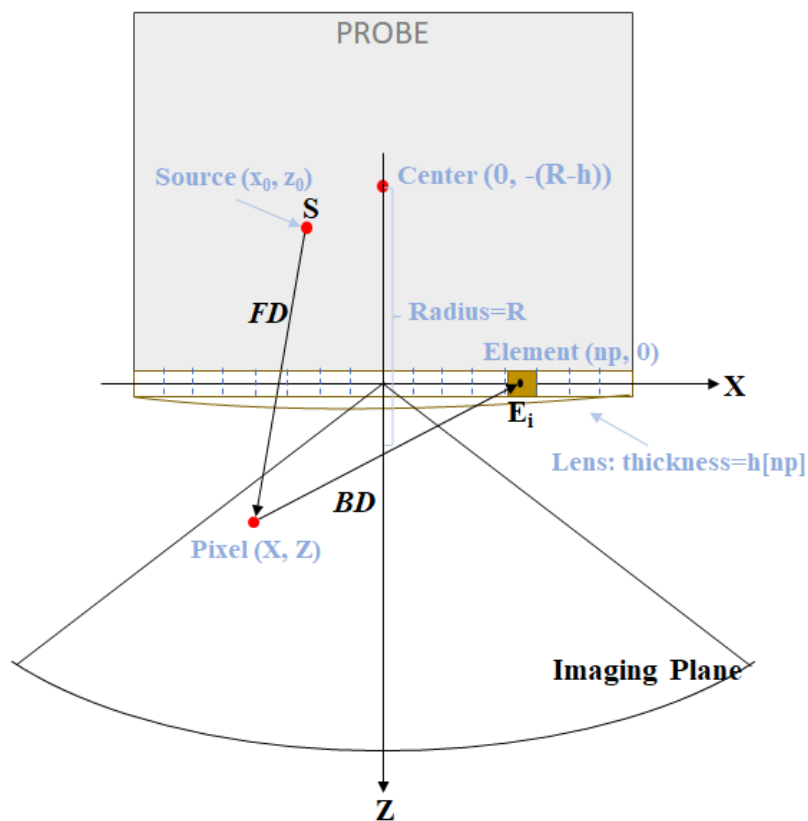


Figure 51 - Thin lens approximation imaging beamforming with an acoustic lens
The FD is not corrected

We have:

$$FD = \frac{d(S, Pixel) - z_0}{c_0}$$

$$BD = \frac{d(Pixel, E_i)}{c_0} - \frac{h[np]}{c_0} + \frac{h[np]}{c_1}$$

Finally, if we put $-\frac{h[np]}{c_0} + \frac{h[np]}{c_1} = \delta[np]$ we have:

$$BD = \frac{d(Pixel, E_i)}{c_0} + \delta[np]$$

We implemented the thin-lens approximation based computation of FD and BD for each pixel of the image. We precalculated the constant delays $\delta[np]$ and optimized our beamforming in CUDA, incorporating the delays. Using this approximation, we achieve a frame rate of around **20 frames/second**.

4.6.4 Beyond the thin lens approximation for delay-and-sum beamforming

Furthermore, it would be possible to correct the FD without adding any extra computations. If we admit that the lens induces an aberration to the emitted ultrasound wave, we can use an aberration correction technique such as time reversal to find the non-aberrated virtual source S' , as if there were no lens [3]. For beamforming, we then compute the FD as if there was no lens with the new source S' (Figure 52).

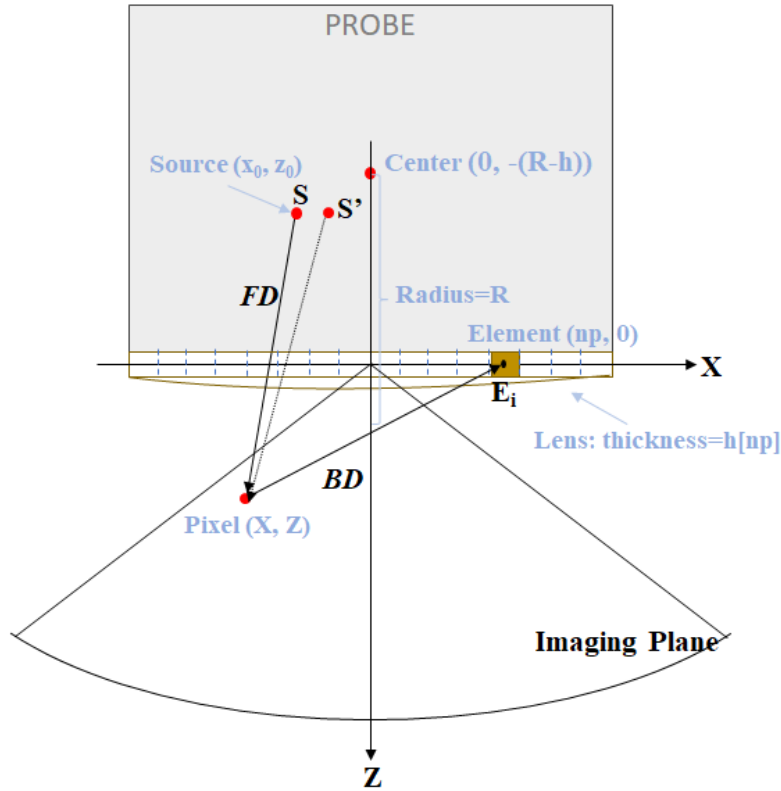


Figure 52 - Thin lens approximation imaging beamforming with an acoustic lens
The FD is corrected

We have:

$$FD = \frac{d(S', Pixel) - z_0}{c_0}$$

$$BD = \frac{d(Pixel, E_i)}{c_0} + \delta[np]$$

For the corrected virtual source position computation, we ran numerical simulations using K-Wave, V 1.1.1 [5]. We simulated the acoustic propagation in a medium containing tissue and using a low-pressure linear propagation model. The model consists on a simplified environment containing the array of piezoelectric elements, the acoustic lens and an array on sensors after the lens. The computation of S' is based on the:

- Simulation of the ultrasound propagation from a given source through the lens;
- Reception of the data in an array of sensors disposed after the lens;
- Backpropagation of the received data without the lens;
- Computation of the maximum of pressure point coordinates.

The backpropagation will reach a maximal focalisation in S' . An example with three sources (blue) and their corresponding corrected position (yellow) is shown in Figure 53.

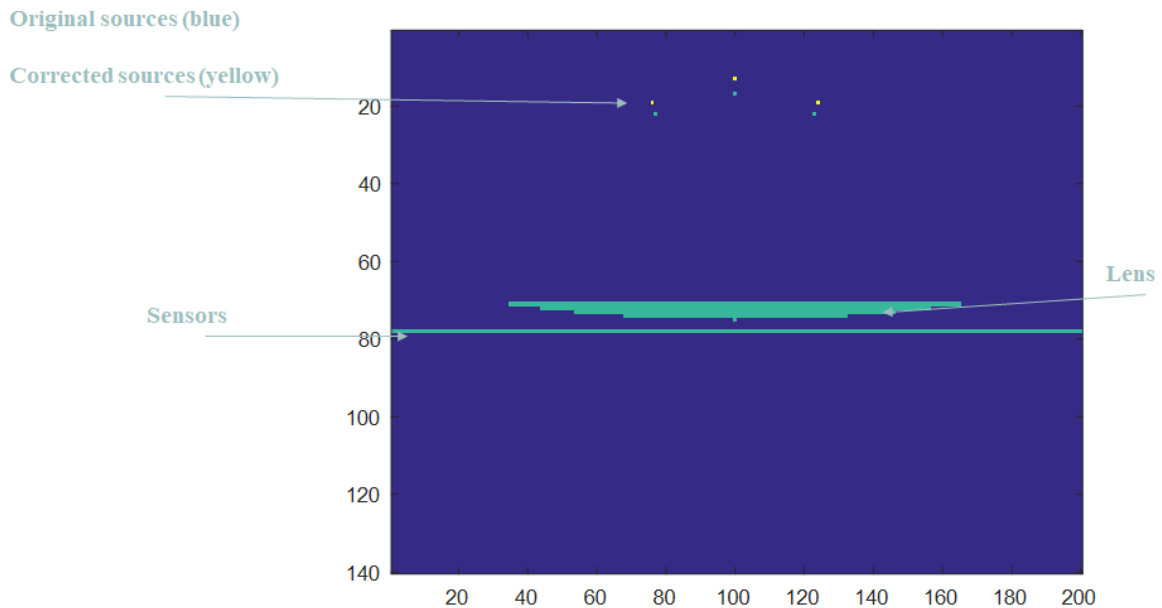


Figure 53 – K-wave simulation environment for the source position correction using time reversal
Sensors pitch: 0.15 mm

Thus, we included the precalculated new sources position in our CUDA optimized beamforming, for the same frame rate around **20 frames/second**.

4.6.5 Evaluation of the errors in emission, on simulations

We intended to evaluate the propagation delay lag induced by the lens using the same simulation environment and medium. For this purpose, we acquired the received ultrasound emissions in a sensor array placed 1 and 20 cm after the lens:

- Without any correction (Figure 54, blue line);
- With the thin lens beamforming with source correction (Figure 54, red line);
- With the complete beamforming without approximations (Figure 54, green line).

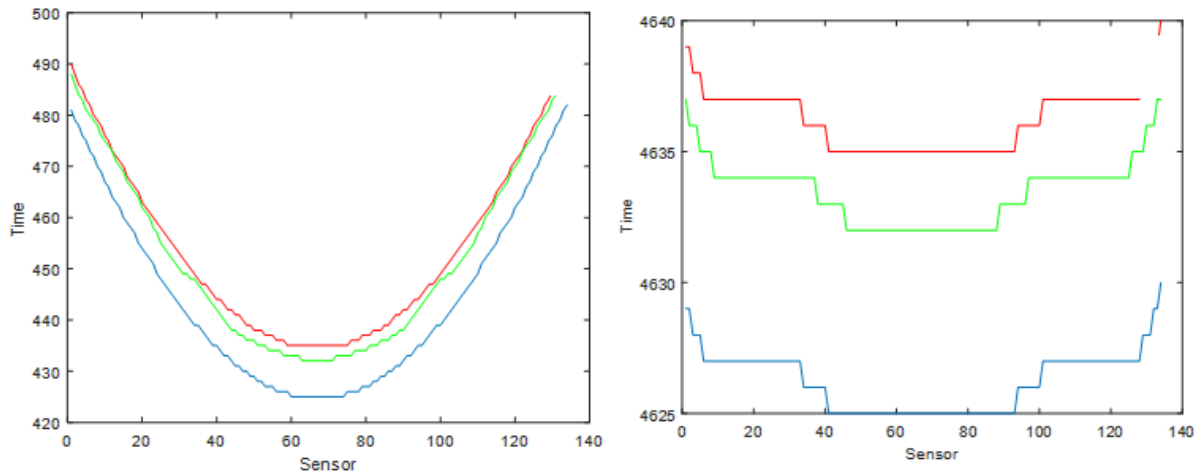


Figure 54 - Received emissions on the array after the lens. Time is in ns
 Left: The sensor array is placed 1 cm after the lens
 Right: The sensor array is placed 20 cm after the lens
 Blue: Without any correction
 Red: Thin lens beamforming with source correction
 Green: Complete beamforming without approximations

We quantified the maximal relative error without the lens correction and with the lens and source correction, in relation to the complete beamforming. With the lens and source correction, we find an absolute error of **2 ns** in both the near field and the far field. Please find the results on Table 5:

Table 5 - Maximal absolute error without the lens correction and with the lens and source correction, in relation to the complete beamforming, when the sensor array is placed 1 and 20 cm after the lens

| Maximal absolute error (ns) | |
|---|---|
| No correction at 1 cm | 7 |
| No correction at 20 cm | 8 |
| Thin lens and source correction at 1 cm | 2 |
| Thin lens and source correction at 20 cm | 2 |

4.7 Beamforming results

4.7.1 Material and methods

We connected the probe to a programmable US scanner (Vantage 256, Verasonics[®], USA). We set the probe's center frequency at 2.8 MHz, we acquired data with a 200% bandwidth, and we used an IQ beamformer. All the 64 elements of each piezoelectric network

of the probe (128 in total, successively 64 then 64) were programmed to transmit and receive data, covering a 90° sector for each plane.

We set an ultrafast sequence based on the compounding of 13 steered divergent wave emissions for each plane. The sources were placed starting at -0.44 degrees, with a step of 0.1 degrees and a distance to the virtual apex of 14.55 wavelengths.

We tested the imaging performances on a CIRS® (USA) cardiac phantom.

4.7.2 Frame rate

First, we saw an improvement of the frame rate from **7 frames/second** using the complete beamforming algorithm to **20 frames/second** using the thin lens approximation beamforming.

4.7.3 Thin less approximation errors

Please find on Figure 55 the bi-plane B-Mode (X and Y orthogonal planes) of the imaging phantom using the complete and the thin lens with source correction beamformings.

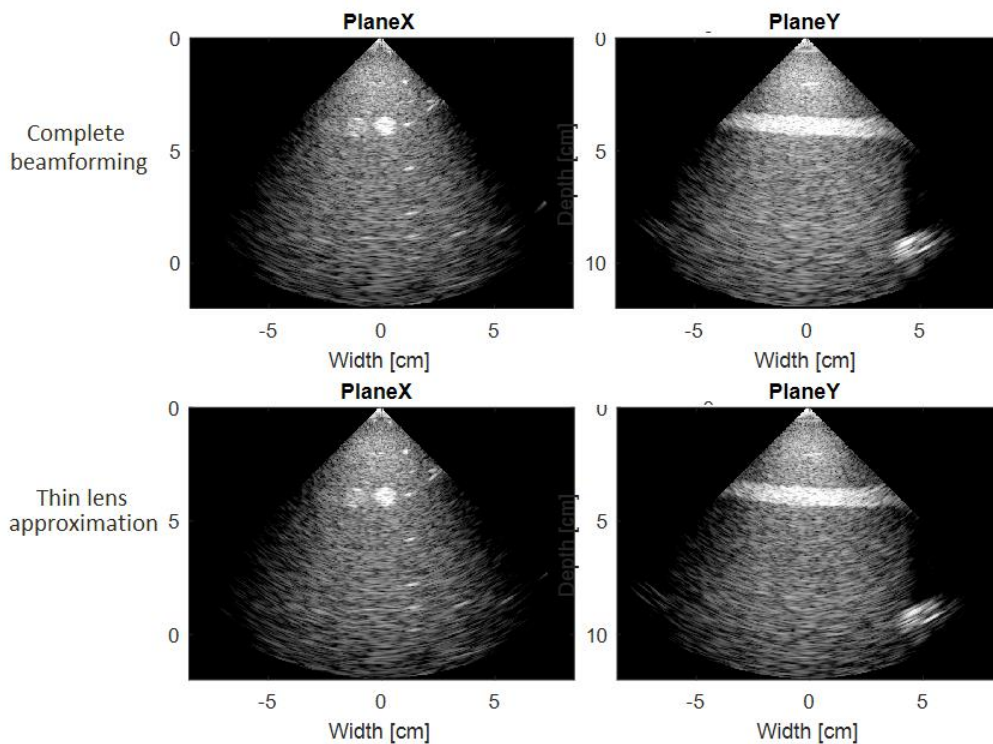


Figure 55 - Bi-plane B-Mode X and Y orthogonal planes of an imaging phantom using the PAXY (Vermon®, France) probe with a dynamic range of 50 dB

Chapter IV – From 2D to bi-plane imaging

Up: Complete beamforming
 Down: Thin lens approximation with source correction beamforming

We first evaluated the loss in dB on the X plane of the images using both algorithms. We chose 6 echogenic points on the image (Figure 56), and computed the absolute errors of the maximum gray level in dB between the image beamformed using the approximation and the image using the complete beamforming. Please find the results on Table 6.

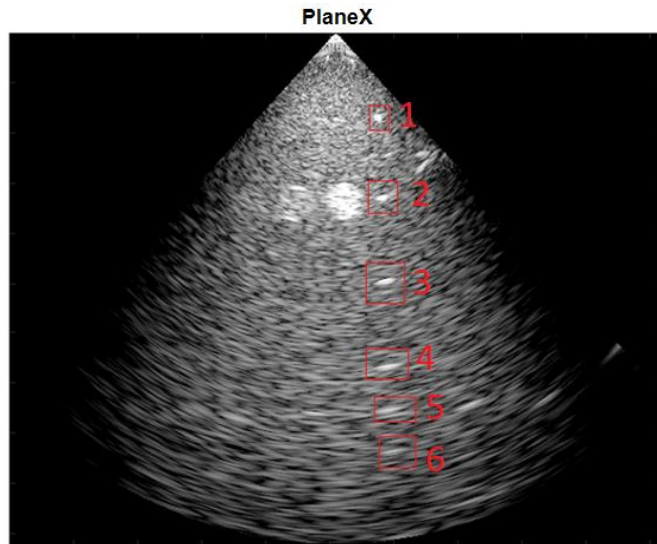


Figure 56 - 6 points used to evaluate the dB loss between the complete beamforming and the thin lens approximation beamforming

Table 6 - Maximum grey level for each point in dB for the complete and the thin lens approximation beamformings and absolute error for each considered point

| Point | Grey level for complete beamforming (dB, normalized) | Grey level for thin lens approximation beamforming (dB, normalized) | Absolute error (dB) |
|-------|--|---|---------------------|
| 1 | 0 | 0 | 0 |
| 2 | -4.8 | -4.2 | 0.6 |
| 3 | -8 | -10.3 | 2.3 |
| 4 | -10.9 | -13.3 | 2.4 |
| 5 | -15.1 | -16.8 | 1.7 |
| 6 | -20.8 | -21.7 | 0.9 |

We find a maximal loss of 2.4 dB when using the thin lens approximation beamforming.

We next compared the lateral resolution on the X plane of the images between the complete and the thin lens with source correction beamformings. We took the same 6 echogenic

points presented in Figure 56 and measured the width of each point at -3 dB. Please find the results on Table 7.

Table 7 – Lateral resolution absolute error for the complete and the thin lens approximation beamformings for each considered point

| Point | Absolute error (cm) |
|-------|---------------------|
| 1 | 0.08 |
| 2 | 0.04 |
| 3 | 0.04 |
| 4 | 0.04 |
| 5 | 0 |
| 6 | 0 |

We find a maximal loss in lateral resolution of 0.8 millimetres. Moreover, the loss decreases with depth and is null on the last two points, in fact, the thin lens correction usually induces errors in the short field but is has very little effect in the far field.

The acceptability or not of the previously presented errors will depend on the target application constraints, by evaluating the priority between frame rate and image quality.

4.7.4 Lateral resolution loss between the P4-2 (Philips©, USA) probe and the PAXY probe (Vermon©, France)

Finally, we compared the lateral resolution between our bi-plane cardiac probe and a clinical conventional cardiac probe. We used the same ultrafast sequence for both probes, by changing only the central frequency to 2.5 MHz for the P4-2 probe. Please find on Figure 57 B-Mode images of an imaging phantom using the PAXY probe including the thin lens beamforming and using the P4-2 probe.

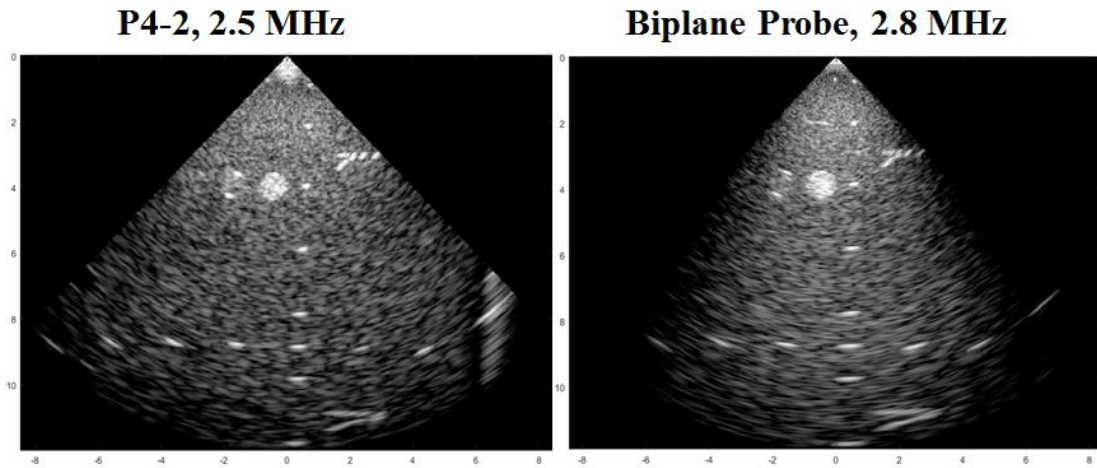


Figure 57 – B-Mode of an imaging phantom with a dynamic range of 50 dB using:

Left: The P4-2 probe (Philips©, USA)

Right: The PAXY probe (Vermon©, France) (thin lens approximation with source correction beamforming)

We chose the same 6 echogenic points as in Figure 56 in an imaging phantom and measured the width of each point at -3 dB. Please find the results on Table 8.

Table 8 – Lateral resolution absolute error using the PAXY and the P4-2 probes on a phantom for each considered point

| Point | Absolute error (cm) |
|-------|---------------------|
| 1 | 0.04 |
| 2 | 0.04 |
| 3 | 0.12 |
| 4 | 0.12 |
| 5 | 0.16 |
| 6 | 0.2 |

We find a maximal loss of 2 millimetres using the PAXY probe compared to the P4-2 probe. Moreover, the error increases with depth. As expected, the PAXY probe has a slight loss on lateral resolution due to our beamforming assumptions, to conception and design differences and to the fact that our probe is not yet fully optimized.

4.8 Bi-plane coherent passive cavitation imaging using the PAXY (Vermon©, France) probe

As discussed before, bi-plane histotripsy monitoring would allow to visualize the cavitation cloud in two orthogonal imaging planes, and to provide a good idea of its three-dimensional shape and surrounding target tissues.

Chapter IV – From 2D to bi-plane imaging

We tested the PAXY (Vermon©, France) probe for passive cavitation imaging. We used the same setup and timings as in 2.2.2 *Experimental setup for coherent passive feasibility* for cavitation generation and image acquisition, and generated the bubble cloud inside a PVA gel in static and moving conditions. The main difference with the conventional 2D acquisitions consists in the data reception, as for passive bi-plane imaging we receive in both orthogonal arrays at the same time. In fact, as the emitted therapeutic wave is focused in 3D, we only need one emission for both X and Y images beamforming. Thus, the timings for emission and passive reception remain the same as for conventional 2D passive imaging. Please find on Figure 58 an example of bi-plane cavitation maps while histotripsy on a PVA phantom.

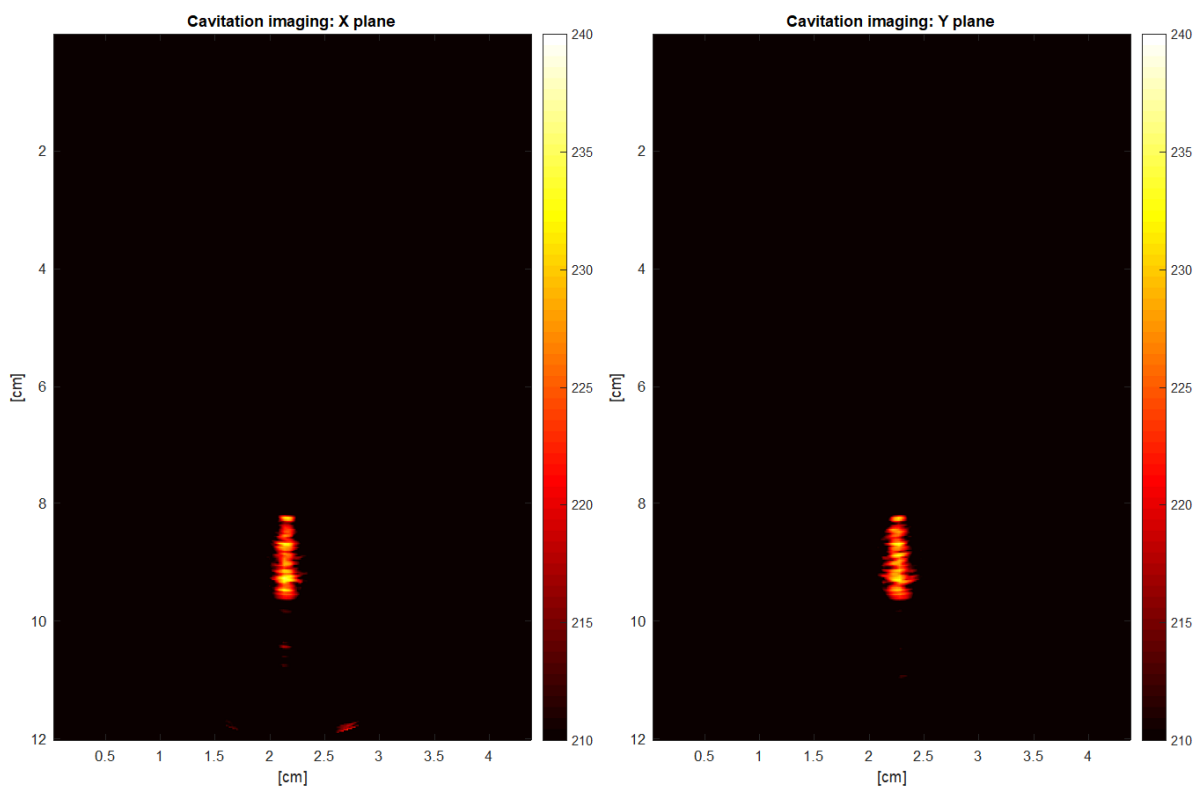


Figure 58 - Bi-plane cavitation maps while histotripsy on a PVA phantom using the PAXY probe
Left: X plane Right: Y plane

Next, we evaluated the CNR of the cavitation maps as in 2.2.5 *Cavitation map evaluation* in static and moving conditions, and found comparable values on the CNR between both probes around 14 in a static condition and around 9 in a moving condition. It is to be noted that there is moreover a slight difference between the X and Y planes of the PAXY probe, that may be the result of the mechanical design and the arrays of the probe. Please find the results on Figure 59.

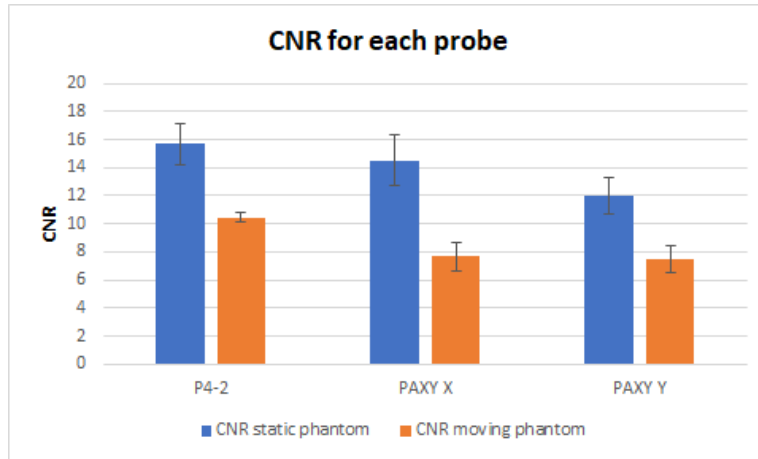


Figure 59 - CNR for cavitation maps evaluation using the P4-2 probe and the PAXY probe

Finally, we drove the same cavitation experiments in a PVA phantom but pushing the emission power above the natural focus cavitation threshold, for an estimated minimal focal pressure peak value under -18 MPa. This kind of experiment usually creates secondary cavitation clouds at the side lobes, as presented in 3.4.3 *Back to 2D imaging*. Please find in Figure 60 an example of bi-plane cavitation imaging using the PAXY probe with a secondary cavitation cloud. In the X plane we can observe inside the blue circle a secondary cavitation cloud, however, it is absent in the Y plane: the secondary cavitation cloud is off center.

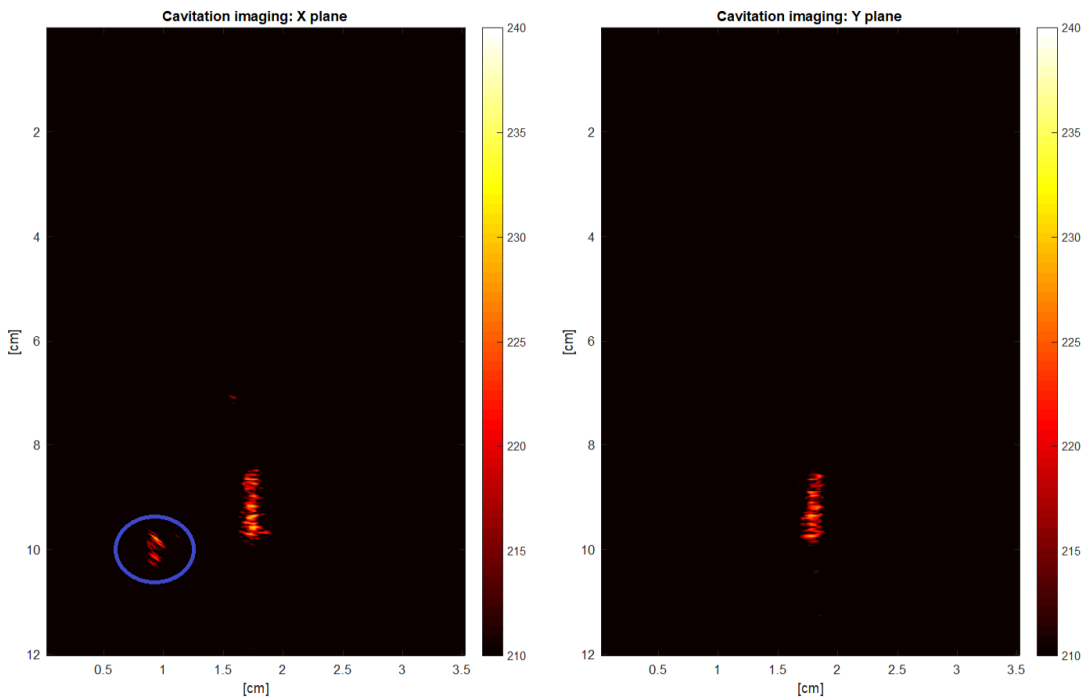


Figure 60 - Bi-plane passive cavitation map while histotripsy in a PVA phantom using the PAXY probe
 Left: X plane. We can observe inside the blue circle a second cavitation cloud
 Right: Y plane

4.9 Conclusion

Bi-plane imaging is presented as a monitoring solution between conventional B-Mode and 3D imaging. It allows to successively image two orthogonal planes with a good image quality and without the need of complex or expensive electronics.

We designed and tested a bi-plane probe adapted to cardiac imaging and including a thin lens corrections algorithm for the frame rate improvement despite a slight loss in image quality. We tested its B-Mode imaging capabilities as well as coherent passive cavitation imaging. In particular, our bi-plane probe presents a loss in lateral resolution (maximum loss of 2 mm) when compared to a clinical conventional cardiac probe. The acceptability of this error will depend on the target application constraints.

It is to be noted that the frame rate is divided by two compared to conventional B-Mode imaging. Nevertheless, passive imaging presents an advantage as only one emission is necessary for both X and Y planes beamforming.

For now, the probe does not allow to monitor a volume, but it provides more information for monitoring and guidance than conventional B-Mode and is a good compromise between image quality, frame rate and monitored area.

Bibliography

1. Tanter, Mickael, and Mathias Fink. “Ultrafast Imaging in Biomedical Ultrasound.” *IEEE Transactions on Ultrasonics, Ferroelectrics, and Frequency Control* 61, no. 1 (January 2014): 102–19. <https://doi.org/10.1109/TUFFC.2014.2882>.
2. Cikes, Maja, Ling Tong, George R. Sutherland, and Jan D’hooge. “Ultrafast Cardiac Ultrasound Imaging: Technical Principles, Applications, and Clinical Benefits.” *JACC: Cardiovascular Imaging* 7, no. 8 (August 1, 2014): 812–23. <https://doi.org/10.1016/j.jcmg.2014.06.004>.
3. Mathias Fink. “Time Reversal of Ultrasonic Fields – Part I: Basic Principles.” *IEEE Transactions on Ultrasonics, Ferroelectrics, and Frequency Control* 39, no. 5 (September 1992): 555–566.
4. [https://phys.libretexts.org/Bookshelves/University_Physics/Book%3A_University_Physics_\(OpenStax\)/Map%3A_University_Physics_III_-_Optics_and_Modern_Physics_\(OpenStax\)/2%3A_Geometric_Optics_and_Image_Formation/2.4%3A_Thin_Lenses](https://phys.libretexts.org/Bookshelves/University_Physics/Book%3A_University_Physics_(OpenStax)/Map%3A_University_Physics_III_-_Optics_and_Modern_Physics_(OpenStax)/2%3A_Geometric_Optics_and_Image_Formation/2.4%3A_Thin_Lenses)
5. <http://www.k-wave.org>
6. Flesch, M, M Pernot, J Provost, G Ferin, A Nguyen-Dinh, M Tanter, and T Deffieux. “4D *in Vivo* Ultrafast Ultrasound Imaging Using a Row-Column Addressed Matrix and Coherently-Compounded Orthogonal Plane Waves.” *Physics in Medicine and Biology* 62, no. 11 (June 7, 2017): 4571–88. <https://doi.org/10.1088/1361-6560/aa63d9>.
7. Felix, N., D. Voisin, O. Clade, and R. Dufait. “Biplane Ultrasound Arrays with Integrated Multiplexing Solution for Enhanced Diagnostic Accuracy in Endorectal and Transvaginal Imaging.” In *IEEE Ultrasonics Symposium, 2005.*, 4:2251–54. Rotterdam, The Netherlands: IEEE, 2005. <https://doi.org/10.1109/ULTSYM.2005.1603332>.
8. Bansal, Ramesh C., Masahiro Shakudo, Pratima M. Shah, and Pravin M. Shah. “Biplane Transesophageal Echocardiography: Technique, Image Orientation, and Preliminary Experience in 131 Patients.” *Journal of the American Society of Echocardiography* 3, no. 5 (September 1, 1990): 348–66. [https://doi.org/10.1016/S0894-7317\(14\)80135-1](https://doi.org/10.1016/S0894-7317(14)80135-1).

Chapter IV – From 2D to bi-plane imaging

9. Tardif, J. C., M. A. Vannan, and N. G. Pandian. “Biplane and Multiplane Transesophageal Echocardiography: Methodology and Echo-Anatomic Correlations.” *American Journal of Cardiac Imaging* 9, no. 2 (April 1995): 87–99.
10. Djoa, K. K., C. T. Lancée, N. De Jong, D. T. Linker, and N. Bom. “Transesophageal Transducer Technology: An Overview.” *American Journal of Cardiac Imaging* 9, no. 2 (April 1995): 79–86.

Part II:
**Guidance and safety parameters and procedures for
the therapy**

Chapter V - Focal spot three-dimensional position monitoring challenges

Special thanks to Wojciech Kwiecinski and Ana Fouquier, who I had the chance to work with in this project.

5.1 Introduction

Valvosoft® is a medical device designed to deliver high intensity short pulses for histotripsy over the calcified aortic valve. The therapeutic procedure is guided by ultrasound and it includes a therapeutic transducer and an imaging probe, both embedded in an applicator designed to be in contact with the patient's skin through an acoustic interface filled with degassed water (Figure 61).

Ultrasound is a cheap and practical imaging modality allowing to easily visualize the inner tissues of a patient, non-invasively and in real-time. Specific ultrasound guidance modalities were initially developed for HIFU applications to evaluate to temperature evaluation of the tissues [8][9][11] or the mechanical properties of the medium to locate the created lesion [10]. Next, in PCUT applications, ultrasound imaging was a practical choice as the echogenicity of the bubble cloud permits its B-Mode visualization [16]. Moreover, PCUT B-Mode monitoring may be combined with specific imaging modalities such as cavitation imaging or elastography [10] if required.

Now, cardiac imaging is challenging and requires the imaging probe to be positioned in a specific position in the intercostal space. The Valvosoft® system was designed to optimize the imaging quality and to ensure that the imaging probe is correctly placed in a fixed location, but at the same time to allow the displacement of the therapeutic beam in order to cover the entire aortic valve surface.

Next, diverse designs of therapeutic transducers have been explored since the appearance of therapeutic ultrasound, and the chosen dimensions, global geometry and number of elements depend on the target organ as well as on the ultrasonic path challenges (ribs, skull) [8][12]. For example, transrectal transducers need to be small enough for anatomical reasons, thus they cannot have a high number of elements for electronic focusing and should be geometrically focused; at the same time, the active surface should be sufficient to allow an

efficient therapeutic emission [13]. In extracorporeal applications such as brain or cardiac therapies, spherical transducers are commonly used as they allow either a pure geometrical focusing [11][16][17], as well as an electronic steering of the focal spot for multi-element transducers [12]. In the latter case, the electronic steering capabilities will depend on the number and the size of the elements. It is to be noted that the more elements, the more complex the driving electronics. Moreover, the array distribution will define specific patterns of the sidelobes distribution and level, to be considered [12]. In particular, annular arrays suppress the level of sidelobes below a given requirement with a minimum number of channels. In this optic, annular array transducers are a feasible solution for cardiac clinical and engineering requirements as they allow an electronic dynamic focusing in the depth direction with few elements [17][18][19].

Valvosoft's® therapeutic transducer was conceived following an annular multi-element configuration that effectively allows an electronic steering of the focal spot along its central axis at the aortic valve common depths, and it has a central hole intended for the positioning of the imaging probe. There are nevertheless some other practical mechanical issues with this configuration that have an impact on the procedure safety.

First, both transducers are not mechanically at the same axial position: in order to always be in contact with the patient, the imaging probe is advanced compared to the therapeutic transducer. Thus, ultrasound emissions travel different paths, and in particular the therapeutic emission travels through degassed water (Figure 61). As water has a different speed of sound than human tissues, the therapeutic emission travels through two different mediums, the tissue and water, which has an influence on the focalization quality. One of the first issues was to evaluate the speed of sound to be used for the therapeutic delay-law computation, ensuring the focalization at the wanted position. We propose here a feasibility study of the therapeutic delay-law to be programmed on the system.

Chapter V– Focal spot three-dimensional position monitoring challenges

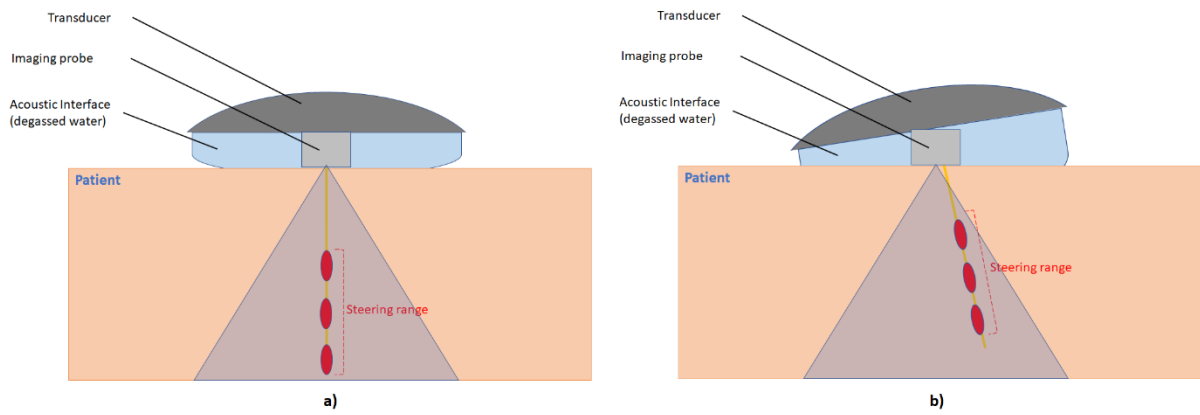


Figure 61 – Electronic steering along the central axis of the transducer

Left: The transducer is not tilted

Right: The transducer is tilted while the probe remains static, thanks to the mechatronic system. The steering range is displaced along a 2D plane

Secondly, the applicator contains a mechatronic system that allows a two-dimensional steering of the therapeutic focal spot along the imaging plane. However, as the imaging probe and the therapy transducer are not inherently solidary devices, there might be pure mechanical misalignments between both transducers, and the therapeutic focal spot might be driven outside the imaging plane. For cavitation monitoring, the imaging plane shall always include the therapeutic focal spot (and more precisely, the cavitation cloud) in the whole area of treatment. In fact, a mechanical misalignment between the two transducers might have as a consequence a “false negative” monitoring, where there is cavitation nucleation outside the imaging plane, “invisible” for the user. For safety reasons, an alignment verification must be driven before each clinical procedure. We propose here a practical method to check if the system is correctly aligned before each procedure for a correct clinical monitoring.

Furthermore, histotripsy generates a cavitation bubble cloud in a precise focal spot. However, as cavitation has a mechanical destructive action on targets, it is difficult to measure the acoustic properties of the focal spot such as pressure, shape, size or position while cavitation with classic systems such as hydrophones. There is no international standard for the acoustic properties' evaluation in histotripsy, and there is a need to develop evaluation acoustic methods while cavitation. One solution is to evaluate the acoustic properties of the focal spot at linear low pressures, following the same standards as for thermal therapies [1][2][3] with classic systems including a hydrophone. Nevertheless, these evaluations are not complete as the effective therapeutic effect is given by cavitation at high pressures. It is therefore necessary to couple classic evaluations with evaluations while cavitation. We propose here to use active

cavitation imaging to retrieve an analysis of the shape, size and position of the bubble cloud, and to compare it to low pressure evaluations.

5.2 Therapeutic speed of sound

5.2.1 Objective and motivations

Valvosoft's® mechatronic system is designed to include the therapeutic transducer and an imaging probe for the procedure monitoring, both embedded inside an acoustic interface filled with degassed water ensuring the correct transmission of ultrasound. The head of the imaging probe is to be directly in contact with the skin of the patient, while the therapeutic transducer is supported by the acoustic interface (Figure 61).

In practice, during therapy, both beams emitted by the therapeutic transducer and the imaging probe penetrate different tissues, which present different speeds of sound. The therapeutic ultrasound emission travels a certain amount of degassed water before the human skin, and water has a significantly different speed of sound than one accepted for human tissues imaging of 1540 m/s [2], depending moreover on its temperature.

The embedded imaging system beamforms B-Mode images using a speed of sound of 1540 m/s. The question is if the therapeutic delay-law computation for the electronic steering should be based on this same value of speed of sound, or if a correction should be included considering that the speed of sound in water at 30°C is around 1509 m/s [2], which is the mean temperature of water inside the acoustic interface. The therapeutic delay-law to be used must be computed in order to ensure a correct focalization.

It is to be noted that in practice, it is not possible to determine the exact speed of sound of every part of the sonicated medium, particularly in the human body. For this reason, the ultrasound imaging systems predefine an average speed of sound that is observed in humans and in consequence, the ultrasound images represent a “virtual reference” in which the therapeutic target must be positioned with precision.

In the “real world” the position of the therapeutic target will be different: the image dimensions will not exactly correspond to the real dimensions, and the effective therapeutic target will not be the one computed by Valvosoft® or by any system with a given delay-law.

5.2.2 Experimental setup

To evaluate the consistency of the position of the therapeutic target between the transducer and the imaging system, we prepared the Valvosoft® system in order to emit ultrasound inside a water tank at a linear low-pressure regime. Water was degassed, and we monitored the temperature and the oxygen level during the whole experiment. We used a hydrophone (Onda©) coupled with an oscilloscope (Rigol©) and a motorized 3-axis stage in order to:

- Locate the effective position of the therapeutic focal spot;
- Compare it with the hydrophone position on the B-Mode images.

We measured these two positions when the therapeutic delay-law was computed using the speed of sound in water, which depends on the water temperature, and when the therapeutic delay-law was computed using 1540 m/s as the speed of sound. The water tank was kept at low temperatures (18°C to 19°C) to present a speed of sound of 1475 m/s, which is significantly different from 1540 m/s and is close to the speed of sound of human fatty soft tissue (1465 m/s [2]). The speed of sound on the imaging system remained hardcoded at 1540 m/s;

5.2.3 Methods

For a given focal spot generated by the transducer, the effective position of this focal spot in water was determined by:

- a. Locating the maximum of generated pressure by manually scanning the ultrasonic field in three dimensions with the hydrophone using the motorized 3-axis stage,
- b. Determining the position of the focal spot in depth, from the therapeutic transducer, by measuring the time of flight of the ultrasonic emission. This time of flight was measured manually using the oscilloscope.

Based on the time of flight measurements, we computed the corresponding distance within a given medium speed of sound by using the equation (11), where d represents the distance in meters, c_{medium} represents the speed of sound of the medium in meters per second and t_{flight} represents the measured time of flight in seconds:

$$d = c_{medium} * t_{flight} \quad (11)$$

The position of the focal spot on the B-Mode was determined by measuring the position of the tip of the hydrophone directly on the image by using the imaging system proposed software tools.

We repeated the measurement for 3 focal depths: 40 mm, 85 mm and 145 mm, and for each focal depth we programmed on Valvosoft®:

- A delay-law using the speed of sound of 1475 m/s;
- A delay-law using the speed of sound of 1540 m/s, the same used by the imaging system.

It is to be noted that 40 mm and 145 mm represent the worst cases for the system configuration.

5.2.4 Results

Table 9 presents the measured positions of the focal spots for the therapeutic delay-laws computed using different speeds of sound.

Table 9 - Results of the measured positions of the focal spots with different predefined speeds of sound for the ultrasound emission delay-law. C_{water} represents the determined speed of sound in water.

| Focal depth on Valvosoft® (mm) | T° Water (°C) Acoustic Interface | C_{water} (m/s) | Speed of sound programmed on Valvosoft® (m/s) | Depth of hydrophone on the image (mm) |
|--------------------------------|----------------------------------|-------------------|---|---------------------------------------|
| 40 | 17.9 | 1475,8 | 1476 | 38.7 |
| 40 | 17.8 | 1475,4 | 1540 | 40.0 |
| 85 | 17.5 | 1474,5 | 1540 | 85.0 |
| 145 | 18.3 | 1477,0 | 1477 | 148.0 |
| 145 | 18.5 | 1477,7 | 1540 | 144.8 |

Overall observations:

- When the speed of sound programmed on Valvosoft® was set at 1540 m/s:
 - o the depth of the hydrophone on the image is equal to the focal depth computed on Valvosoft® at 40mm and 85mm;
 - o the depth of the hydrophone on the image presents an error of 0.2 mm to the focal depth computed on Valvosoft® at 145mm.

Chapter V– Focal spot three-dimensional position monitoring challenges

- When the speed of sound predefined on Valvosoft® was programmed accordingly to the speed of sound in water:
 - The depth of the hydrophone on the image presents an error of 1.3 mm to the focal depth computed on Valvosoft® at 40 mm;
 - The depth of the hydrophone on the image presents an error of 3 mm to the focal depth computed on Valvosoft® at 145 mm.

5.2.5 Conclusion

When the therapeutic and the imaging emissions are parameterized using the same speed of sound of 1540m/s:

- The therapeutic target position error on the B-Mode is much smaller than when the predefined speed of sound is 1475 m/s (respectively $\pm 0.2\text{mm}$ vs. $\pm 3\text{mm}$ according to the results);
- This result is obtained even though the real speed of sound presents a variability between the different sonicated mediums.

In conclusion, the position of the focal spot computed with Valvosoft® corresponds to the position of the focal spot on the image when both are programmed with the same speeds of sound. Therefore, Valvosoft® can rely on the distances computed by the imaging system for the therapeutic target positioning without any correction due to the speed of sound.

It is important to remember that in this case the computed focal depth does not correspond to the real focal depth: B-Mode images represent a “virtual world”.

5.3 Alignment verification protocol

5.3.1 Objectives

Valvosoft® includes a mechatronic system allowing a 2D therapy monitoring. The therapeutic transducer and the imaging probe are ideally aligned for target positioning and cavitation monitoring, meaning that the therapeutic focal spot shall be inside the imaging plane no matter the mechatronic angle tilt value nor the focal spot position along the steering range.

In an imaging system, the imaging ultrasound emission plane presents characteristics depending on the probe and the emission parameters. In particular, each system has a maximal

plane elevation, that defines a resolution in depth. Thus, a scatterer present anywhere inside this zone in elevation will be “seen” by the system the same way: we define here a resolution in elevation.

In the case of histotripsy, the therapeutic transducer and the imaging probe could be misaligned as shown in Figure 62, but if the bubble cloud remains inside the imaging plane, it will be “seen” on the B-Mode image. Nevertheless, as soon as the bubble cloud gets out of the imaging area, the monitoring will fail.

The complete quantitative alignment between both transducers is typically done at low-pressure using a hydrophone setup, which allows to find the focal spot at low pressures [1]. For safety reasons, before each clinical trial, it is necessary to verify that this alignment between both transducers remains tolerable (c.f. the misalignment value is inside a range of acceptability) for every possible target point, but hydrophone setups are usually complex for a non-trained operator and remain difficult to set in a hospital.

Some solutions such as cavitation markable phantoms have been proposed [6], but for now they only allow to evaluate the cavitation cloud position in a slice perpendicular to the central axis of the transducer, and it is not possible to evaluate the cavitation position in depth. We propose a practical qualitative in-house designed method for the alignment verification, easily set on a clinical environment.

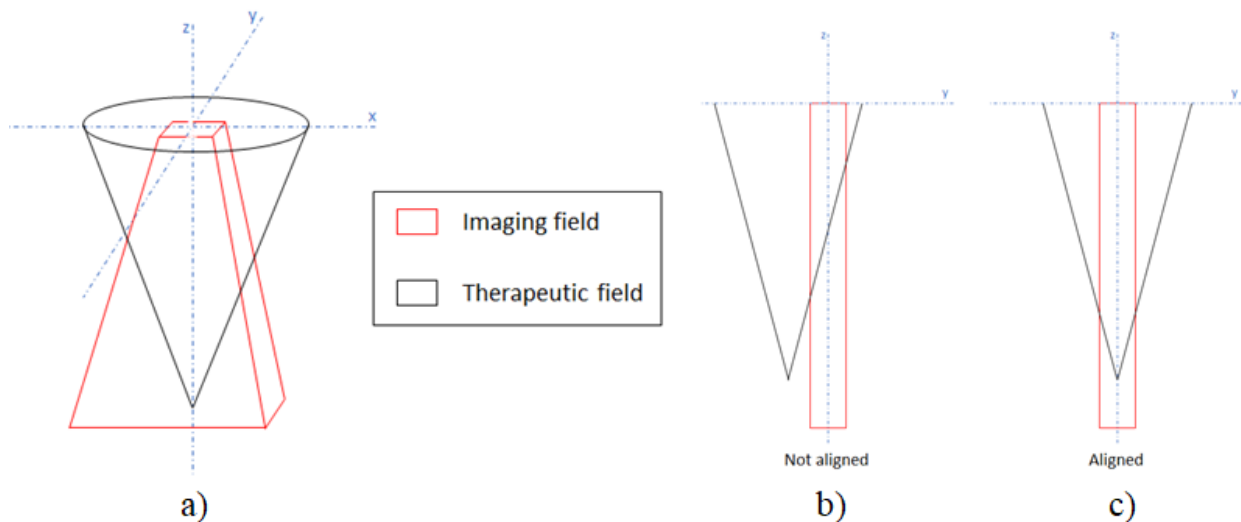


Figure 62 – a) 3D representation of both therapeutic and imaging fields volumes
 b) Representation of misaligned therapeutic and imaging planes
 c) Representation of aligned therapeutic and imaging planes

5.3.2 Plaster sticks verification protocol

One intuitive way to verify if the misalignment is acceptable for histotripsy is to define a target in a degassed water tank, visualize the target on the B-Mode and then proceed to cavitation generation in order to destroy it:

- If the target is visible on the B-Mode, it means that it is located inside the imaging plane volume;
- If the target is destroyed by cavitation, it means that it is located near the focal spot.

Then, several target points have to be treated in order to browse the entire target range inside the imaging plane. The minimal number of targets to test is 3, P1, P2 and P3, as a plane is geometrically defined by three non-aligned points, as presented in Figure 63.

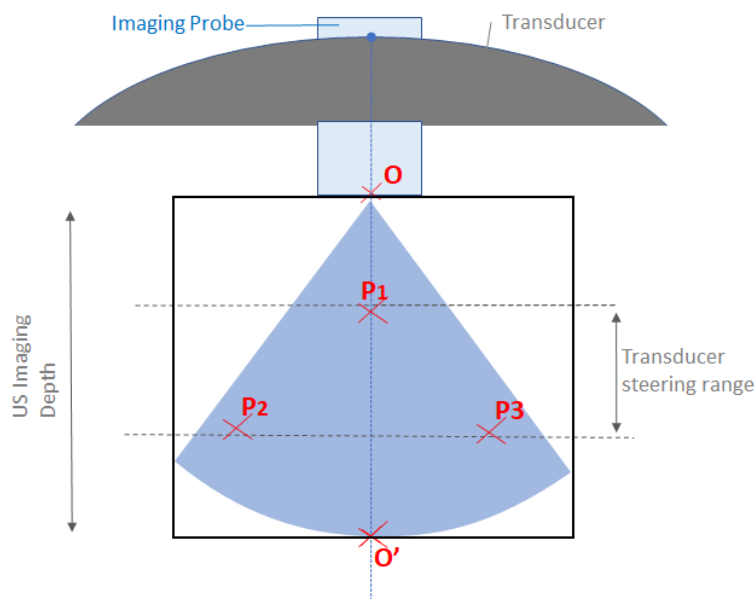


Figure 63 - Alignment protocol target points P1, P2 P3
O represents the origin of the imaging plan and O' represents the bottom
The target points are not aligned and cover the whole steering range of the transducer

Nevertheless, the problem is more complex as other phenomena join the pure mechanical cavitation effect caused by the bubble implosion. In fact, shockwaves and strong streaming (see *1.1.1 Ultrasound physics*) may also induce a mechanical effect on the target further than the acceptability range near the focal spot. Moreover, the target needs to be smaller than the accepted resolution, which in our case is the imaging plane width at the geometrical

focus (2.5 mm) as seen in Figure 64. Therefore, we needed to design a specific setup in order to get around these problems.

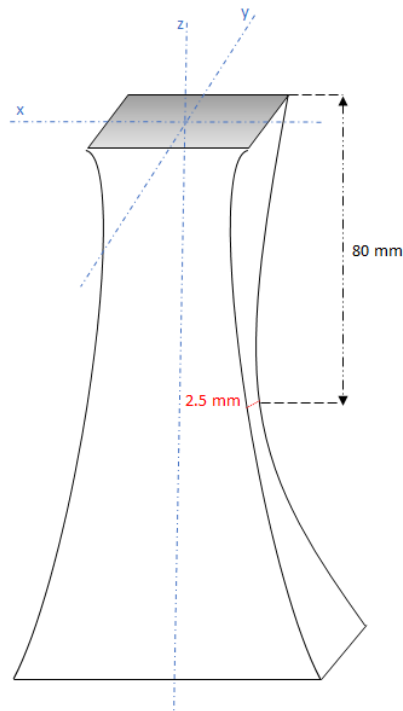


Figure 64 - Imaging plane volume

First, we chose as targets plaster sticks (1 mm thick) as they are thin, easy to produce and are easily trimmed by cavitation. The cavitation cloud implosion effect is easily identifiable as it will trim the stick, while shockwaves will “push” or induce a clean break of the stick.

Secondly, we 3D-printed a support containing a slot intended to hold the stick and having a grid of grooves intended to let the streaming flow without cumulating around the plaster stick. Please find in Figure 65 the complete setup for the alignment verification protocol.

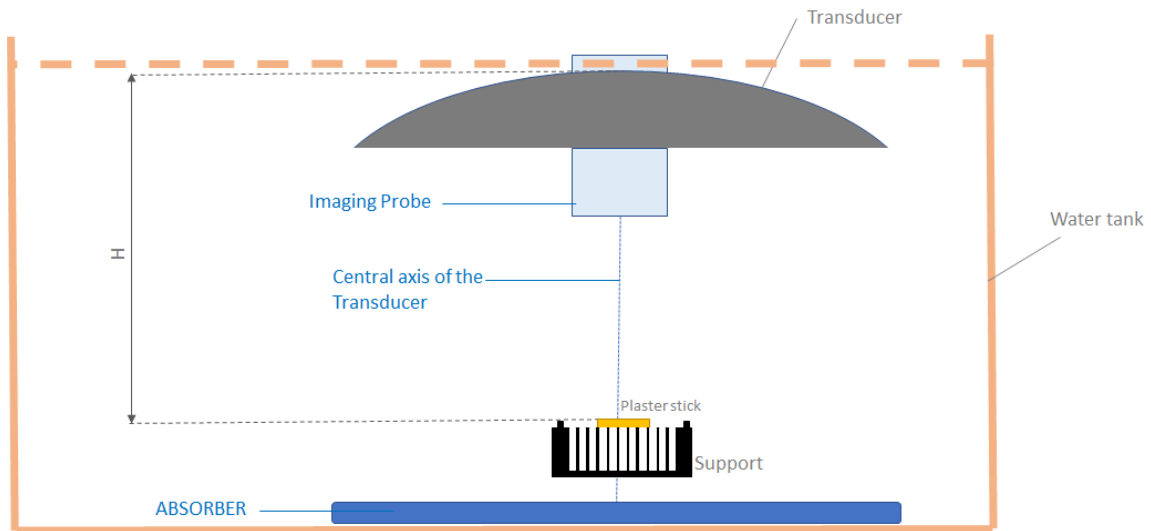


Figure 65 - Setup for the qualitative alignment verification protocol

Next, in order to validate the protocol, we first verified that both the imaging probe and the therapeutic transducer were aligned using a classic hydrophone setup. Then, we proceeded with cavitation tests over $N = 20$ plaster sticks, 10 sticks visible on the B-Mode and 10 sticks 2.5 mm away from the imaging plane, not being visible on the B-Mode.

We managed to trim all the sticks inside the imaging plane (as shown in Figure 66), while none of the sticks being just outside the imaging plane were destroyed.



Figure 66 - Result of the alignment verification protocol when both transducers are aligned

We may accept that if the target is trimmed by cavitation in the three non-aligned points P1, P2 and P3, both transducers are sufficiently aligned for a therapeutic procedure.

5.4 Focal spot and cavitation cloud behaviours

5.4.1 Objectives and motivations

Classic high intensity focused ultrasound (HIFU) technologies producing a thermal action or shockwaves are to this day already in clinics, and there exist international standards

that allow to fully characterize the systems' focal spot size, shape and position typically by using a hydrophone in a water tank [1][2][3]. Such measurements present two major limitations:

- Hydrophones are highly sensitive but present very low tolerance on the incident maximal pressure. All the measurements can thus only be performed at low pressures and therapeutic levels cannot be evaluated. This limitation can partly be bypassed by performing pressure acquisitions with equivalent setups, which can sustain higher incident pressures (e.g. an interferometer setup). However, no such setup can sustain cavitation, which represents the effective therapeutic location of histotripsy, and no such setup can be performed in another medium than water.
- Measurements in water, with or without hydrophone, provide only partial information on the pressure distribution and the focal spot position at high pressure regimes. Ultrasonic attenuation plays a major role on the pressure distribution as well as on the focal spot position generated by HIFU systems, but, particularly at the ultrasonic frequencies of Valvosoft®, water does not attenuate ultrasound whereas tissues do. The precise location of the focal spot generated by the system at the therapeutic target cannot thus be evaluated by such measurements.

It is possible to adapt the hydrophone procedures described on the standards to low pressure measurements, allowing to characterize the focal spot position, shape and size at linear regimes, but these evaluations are not complete as the behavior at high pressures is non-linear and while cavitation, ultrasound behaves differently:

- There is a strong influence of the harmonics on the focalization quality [7];
- The bubble cloud behaves as an ultrasonic reflector: while cavitation, the incident waves are reflected on the remaining bubbles: the positive pressure becomes negative and creates a whole cavitation cloud (a cloud of numerous bubbles) [7];
- The amplitude of the positive pressure is much higher than the negative one. The effective position of the cavitation cloud is a mixture of those two distributions and remains difficult to predict.

To our knowledge, there is to this day no standards allowing to characterize a histotripsy system. Inertial cavitation has a mechanical destructive action on targets, and hydrophones are not adapted for this use. It is mandatory to couple low pressure with high pressure assessments: there is a need to develop evaluation acoustic methods while cavitation.

Our main goal was to prove that the maximal cavitation cloud dimension produced by Valvosoft® is smaller than 3 cm, the mean diameter of an aortic valve.

We propose to characterize the position and the dimensions of both the focal spot (low pressure) and the cavitation cloud (high pressure) that are produced by the Valvosoft® system through simulations and active cavitation imaging respectively.

5.4.2 Numerical simulations

The main goal of the simulations was to evaluate the focal spot position and dimensions in water at 30 °C, which is Valvosoft® regulation temperature inside the acoustic interface, and in a propagation model close to the human body. As a secondary goal, we wanted to quantify the effect of the therapeutic transducer's mechatronic steering on the focal spot dimensions, in a propagation model close to the human body.

We ran numerical simulations using K-Wave, V 1.1.1 [5]. We retrieved mean properties of human tissues from the standard NF EN 60601-2-37 [4] which constitutes the basis of acoustic properties for ultrasonic phantoms and echographers.

We first simulated the acoustic propagation in a medium containing only water at 30°C, for different therapeutic targets and using both low-pressure linear propagation and high-pressure non-linear propagation models. The model consists in a simplified environment containing the therapeutic transducer and the imaging probe, see Figure 67. For simplification reasons, the acoustic interface was not introduced in the model. Its impact has been determined as negligible in a few assessment simulations.

Chapter V– Focal spot three-dimensional position monitoring challenges

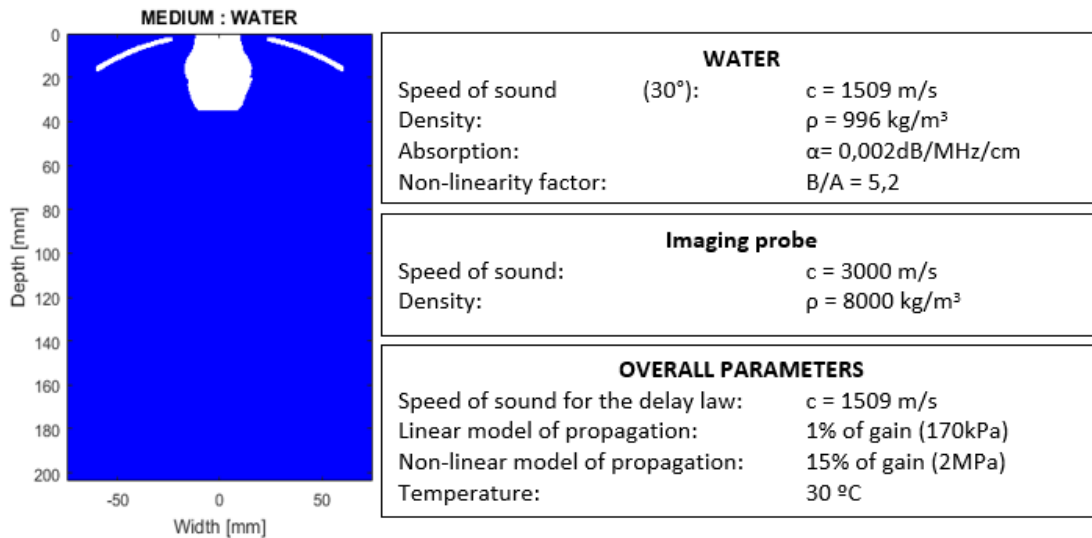


Figure 67 - Scheme of the simulation environment. Blue: water; White: imaging probe and therapeutic transducer

Source for absorption value: [4]. The imaging probe acts as a reflector.

Secondly, we simulated the acoustic propagation in a medium containing water at 30°C and tissue in order to simulate the acoustic interface, for different therapeutic targets using a low-pressure linear propagation model. The interface between the therapeutic transducer and tissue is considered perfect: it is entirely filled with water; no air was added on the edges nor coupling gel with has been put between water and tissue. We repeated the simulation when the therapeutic transducer was 10° tilted, see Figure 68.

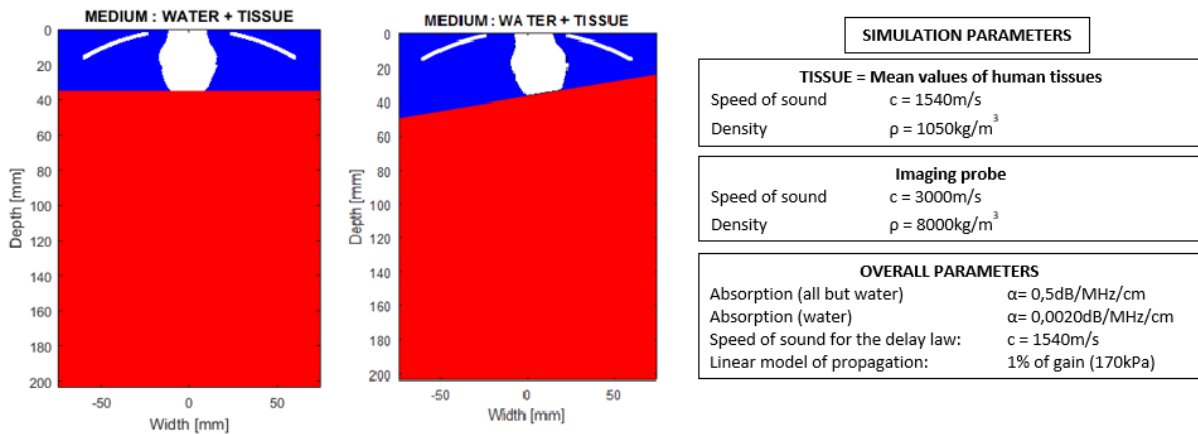


Figure 68 - Scheme of the simulation environment. Blue: water; Red: tissue; White: imaging probe and therapeutic transducer.

Left: no tilt. Right: 10° tilt

Source for tissue and absorption: [4]. The imaging probe acts as a reflector.

5.4.3 Active cavitation imaging analysis

In order to characterize the cavitation cloud size and position behaviour in water, we used an active cavitation imaging analysis. We generated cavitation in a water tank at different depths when no obstacle was set and when a human tissue mimicking phantom (here, Zerdine®) was placed between the therapeutic transducer and the focal spot (Figure 69 a) and b)). As water and tissue do not present the same acoustic properties, we wanted to study cavitation with an acoustic medium as close to the human body as possible. Valvosoft® allows a mechanical tilt of the therapeutic transducer, permitting to generate cavitation in a 2D plane (maximum tilt of 10°, see Figure 69 b) and c)). We also intended to characterize cavitation with this mechanical tilt.

We placed the therapeutic transducer in order to generate cavitation in a degassed water tank. Water was maintained degassed under 1.5 mg/L of oxygen and the water tank temperature was measured but not regulated: its temperature was stable around 22°C with an augmentation of 1.4°C between the beginning and the end of the experiments. Temperature was regulated inside the acoustic interface at 30°C. The phantom was hold by a wide support that did not interfere with the ultrasound emission. We placed ultrasound absorbers at the bottom of the water tank to avoid reflections that would interfere with the acoustic emission or produce artefacts on the image.

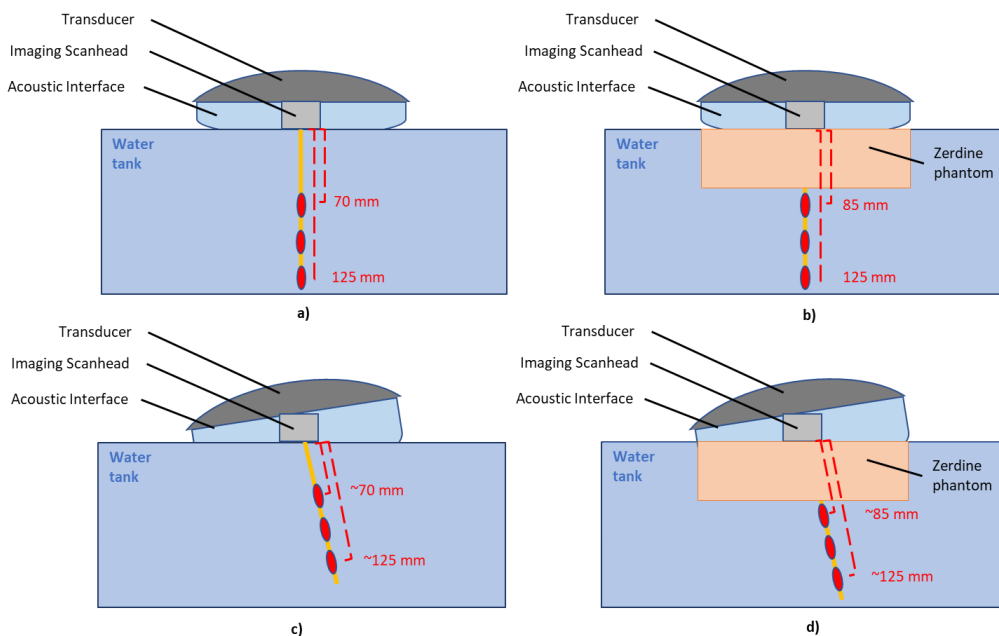


Figure 69 - a) Setup without the Zerdine with no tilt b) Setup with the Zerdine with no tilt c) Setup without the Zerdine with a transducer tilt of 10° d) Setup with the Zerdine with a Transducer tilt of 10°

The cavitation cloud was monitored directly with the B-Mode and the cavitation cloud tracking functionality performed a segmentation of the cloud on each image. The dimensions and position of the cloud were registered in real-time. It is to be noted that no significant image distortion and thus no significant measurement bias on the image is introduced by the presence of the acoustic interface membrane.

The active cavitation cloud segmentation consisted in a pure image processing technique, taking profit of the fact than the bubble cloud is highly echogenic, and it is possible to threshold the image (with a manually set threshold) to obtain a proper segmentation for each frame. Figure 70 presents an example of acquired echographic images in water and through the Zerdine during the experiments and the corresponding segmented cavitation surfaces. All the image properties (pixel-size, dimensions, positions) were retrieved and processed.

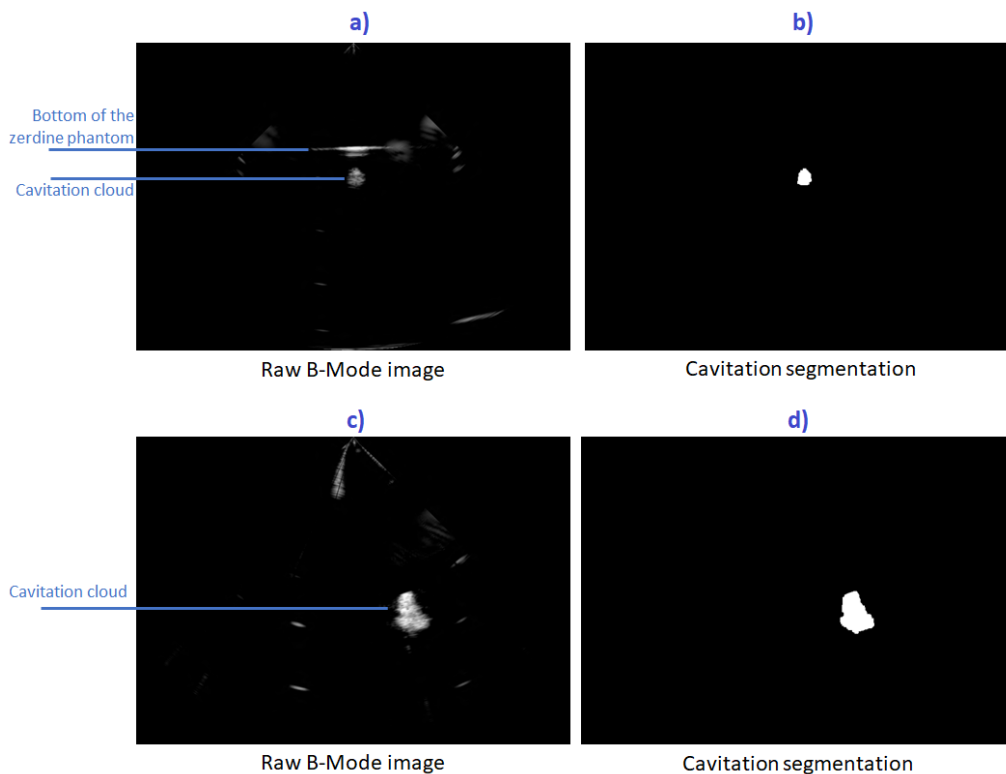


Figure 70 - a) Raw B-Mode image acquired by Valvosoft® during the cavitation experiment, through Zerdine®, at a therapeutic target depth of 85mm with no tilt and b) corresponding cavitation cloud segmentation
 c) Raw B-Mode image acquired by Valvosoft during the cavitation experiment, through water, at a therapeutic target depth of 85mm with a 10° Transducer tilt and d) corresponding cavitation cloud segmentation
 To be noted that the imaging depths are different for a) and for c)

5.4.4 Expected results and hypothesis

The cavitation cloud size and position remain difficult to fully predict as ultrasound propagation is sensitive to parameters that are hard to completely regulate such as temperature or the oxygen level, and to parameters that are hard to measure such as the heterogeneities of the medium or the wave propagation aberrations (refraction, ...). In fact, in complex mediums, strong interfaces may produce attenuations, changes of direction, phase shifts, etc.

Moreover, as we saw in *1.1.3 Inertial cavitation and bubbles behaviour*, ultrasound contains harmonics, of which non-linear effects may have an influence on the cavitation behaviour such as pre-cavitation (cavitation before the therapeutic target on the vertical axis). The stronger the harmonics, the stronger the non-linear effects.

Nevertheless, it remains possible to predict the cavitation cloud position and size with a certain precision. The final goal of the experiments was to evaluate this precision in a controlled environment. We tried to get as close as possible to the *in vivo* conditions, however, these conditions are difficult to reproduce accurately. As a consequence, we expected experimental imprecisions due to:

- Temperature gradient between water inside the acoustic interface, water in the water tank and the Zerdine®;
- Strong non-linear effects in water;
- Acoustic reflexions between the interfaces the acoustic interface, Zerdine® and water in the water tank;
- The fact that Valvosoft® emission delay law is calculated for a speed of sound of 1540 m/s, and water has a different speed of sound. We remind that in all our cavitation experiments, ultrasound crosses mediums with different speeds of sound.
- When the Transducer is tilted, the emitted ultrasound beam crosses different quantities of the Zerdine: the attenuation is therefore asymmetrical as well as non-linear effects at the focus.

Otherwise, some results are expected independently of the experimental conditions:

- The cavitation cloud size should increase with depth;
- The cavitation cloud size should increase with gain;
- The cavitation cloud should remain symmetrical in the lateral dimension;

- The cavitation cloud should have a slight asymmetry in the axial direction (pre-cavitation due principally to non-linear effects is expected). Moreover, this asymmetry should increase with depth.

The cavitation cloud should present a slight asymmetry in both dimensions when the transducer is tilted.

5.4.5 Results

First, concerning the simulations, the environment containing only water allow us to have an idea of the dimensions and positions of the focal spot in an ideal medium.

- As expected, the high-pressure dimensions are smaller than the low-pressure dimensions due to the non-linear effects. The focal spot location accuracy (effective vs. theoretical position) has an error smaller than 1 mm;
- The length of the focal spot at the low-pressure regime is between 6 and 23 mm and its width is between 0.75 mm and 1.5 mm at -3 dB;
- The length of the focal spot at the high-pressure regime is between 5 and 19 mm and its width is between 0.4 mm and 0.6 mm at -3 dB.

The dimensions appear slightly greater in the simulations with the environment containing tissue than in the simulations with the environment containing only water, which is expected. Simulations in tissue allow us to assess the behaviour of the cavitation cloud in a more complex environment, containing interfaces and different medium properties.

We could assess the effect of the therapeutic transducer's mechanical tilt on the focal spot dimensions. In fact, due to Valvosoft's® setup, the imaging probe interferes with the therapeutic ultrasound emission path. As a result, the dimensions of the focal spot appear smaller when the therapeutic transducer is tilted, which is an optimistic result for safety reasons. Please find in Figure 71 examples of the simulations on the medium containing tissue at different focal depths and tilt angles.

Chapter V– Focal spot three-dimensional position monitoring challenges

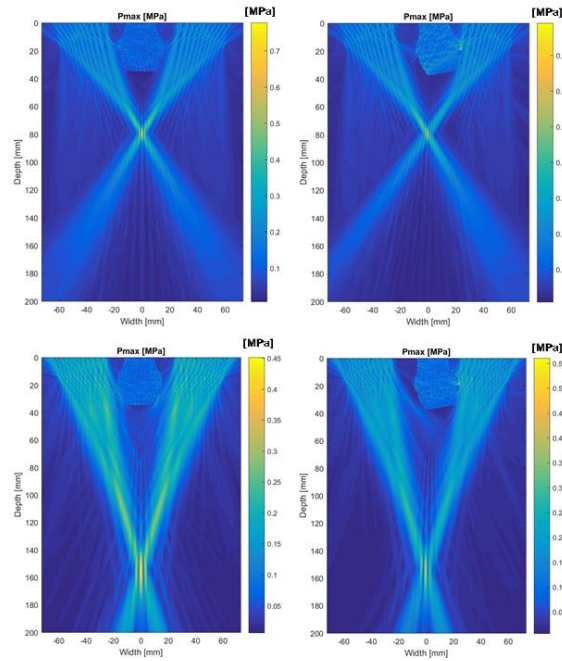


Figure 71 – Up: Simulated pressure field for a therapeutic target depth of 80 mm in mediums containing tissue without tilt (left) and with a transducer tilt of 10° (right).
Down: Simulated pressure field for a therapeutic target depth of 160 mm in mediums containing tissue without tilt (left) and with a transducer tilt of 10° (right)
The scan head is visible at the top of the map. The colorbar represents the pressure. To be noted: the colorbar scale is not the same between both images

Secondly, concerning the active cavitation imaging analysis, through Zerdine, the cavitation cloud:

- Remains globally symmetrical on its horizontal and vertical axis (which is not the case in water);
- The centroid of the segmented cloud remains close to the therapeutic target (distance < 3 mm in the vertical dimension);
- The maximum segmented cavitation surface is 2 cm².

When we raise the ultrasound gain, the behaviour of the size and position of the cavitation cloud follow expected results:

- The cavitation cloud position remains generally constant;
- The size of the cavitation cloud increases.

It is to be reminded that these results are to be considered with caution as they were performed in a medium that is very simplified compared to a human body.

5.5 Discussion and conclusions

Histotripsy is a promising therapeutic technique commonly guided by ultrasound. It is still a recent technology and, for now, there are no specific standards for the cavitation cloud position, size and shape evaluation. Moreover, each histotripsy device may have its own constraints, and specific calibration and testing protocols are to be designed following the needs of each machine to ensure a safe procedure.

Valvosoft® is an ultrasound-guided histotripsy device adapted for cardiac therapies, mechanically designed to ensure an ergonomic deployment of the procedure. In particular, it includes:

- An imaging probe embedded in the therapy transducer;
- An electronic steering for the focal spot displacement along the central axis of the transducer;
- A mechatronic tilt for the focal spot displacement;
- An acoustic membrane filled with degassed water intended to ensure the coupling between the device and the patient.

Those particular subsystems induce specific safety issues as:

- The effective focal spot (i.e. the cavitation cloud) size, shape and position vary following the target depth and the propagation medium;
- The therapeutic focal spot shall be inside the two-dimensional imaging plane during the whole therapeutic emission;
- The speed of sound in the acoustic membrane is different than the mean speed of sound in the tissues.

First, we deployed tests *in vitro* and in simulations to evaluate:

- The speed of sound to be used for the delay law calculation on the therapeutic transducer to ensure a precise targeting;
- The bubble cloud shape and behaviour in the whole steering range (electronic and mechanical) and compared them to our maximal constraints.

Chapter V– Focal spot three-dimensional position monitoring challenges

We concluded that we shall keep the same speed of sound for the therapeutic delay law as for the imaging probe (i.e. 1540 m/s). Moreover, the dimensions and position of the cavitation cloud respect our constraints for the aortic valve treatment in the whole steering range. It is to be noted that these conclusions correspond to Valvosoft's® configuration, and each histotripsy device shall evaluate its own performances.

Next, the focal spot position in relation to the imaging plane is usually measured using a hydrophone. However, hydrophone setups are complicated to be set in clinical practice, and they do not allow to evaluate the cavitation cloud position (at high pressures), which is the real histotripsy therapeutic mode of action to be tested.

Finally, we developed an intermediate setup allowing to qualitatively evaluate the cavitation cloud position in relation to the imaging plane, more friendly with a hospital environment. Nevertheless, the setup is only qualitative, and requires a water tank which still may be complex for a clinical practice. A quantitative, more precise and more hospital friendly protocol is to be designed.

Bibliography

1. IEC TS 62556:2014:2014-04. Ultrasonics – Field characterization – Specification and measurement of field parameters for high intensity therapeutic ultrasound (HITU) transducers and systems.
2. NF EN 60601-2-62:2015-09. Medical electrical equipment - Part 2-62: Particular requirements for the basic safety and essential performance of high intensity therapeutic ultrasound (HITU) equipment.
3. NF EN 62359:2011-12. Ultrasonic – Field characterization – Test methods for the determination of thermal and mechanical indices related to medical diagnostic ultrasonic fields.
4. NF EN 60601-2-37/A1 :2015-11:2008-04. Medical electrical equipment - Part 2-37: Particular requirements for the basic safety and essential performance of ultrasonic medical diagnostic and monitoring (IEC 60601-2-37:2007)
5. <http://www.k-wave.org>
6. Cain, Charles, Xu, Zhen, Maxwell, Adam, Wang, Tzu-yin Park, Simone. Gel phantoms for testing cavitation ultrasound (histotripsy) transducers. United States Patent 8539813, September 24 2013.
7. Wan, Mingxi, Yi Feng, and Gail ter Haar, eds. *Cavitation in Biomedicine: Principles and Techniques*. Springer Netherlands, 2015.
8. Mathieu Pernot. Nouvelles techniques de thérapie ultrasonore et de monitoring. Physique [physics]. Université Paris-Diderot - Paris VII, 2004.
9. Song, Jae Hee, Yangmo Yoo, Tai-Kyong Song, and Jin Ho Chang. “Real-Time Monitoring of HIFU Treatment Using Pulse Inversion.” *Physics in Medicine and Biology* 58, no. 15 (August 7, 2013): 5333–50. <https://doi.org/10.1088/0031-9155/58/15/5333>.
10. Bastien Arnal. Elastographie pour le suivi des thérapies par ultrasons focalisés et nouveau concept de cavité à retournement temporel pour l’histotripsy. Acoustique [physics.class-ph]. Université ParisDiderot - Paris VII, 2013.
11. Grondin, Julien, Thomas Payen, Shutao Wang, and Elisa E. Konofagou. “Real-Time Monitoring of High Intensity Focused Ultrasound (HIFU) Ablation of In Vitro Canine Livers Using Harmonic Motion Imaging for Focused Ultrasound (HMIFU).” *Journal of Visualized Experiments*, no. 105 (November 3, 2015). <https://doi.org/10.3791/53050>.

12. Pernot, Mathieu, Jean-François Aubry, Mickaël Tanter, Jean-Louis Thomas, and Mathias Fink. “High Power Transcranial Beam Steering for Ultrasonic Brain Therapy.” *Physics in Medicine and Biology* 48, no. 16 (August 2003): 2577–89. <https://doi.org/10.1109/TMI.2010.2076829>.
13. Alkhorayef, Mohammed, Mustafa Z. Mahmoud, Khalid S. Alzimami, Abdelmoneim Sulieman, and Maram A. Fagiri. “High-Intensity Focused Ultrasound (HIFU) in Localized Prostate Cancer Treatment.” *Polish Journal of Radiology* 80 (March 13, 2015): 131–41. <https://doi.org/10.12659/PJR.892341>.
14. Arnal, B, J Baranger, C Demene, M Tanter, and M Pernot. “In Vivo Real-Time Cavitation Imaging in Moving Organs.” *Physics in Medicine and Biology* 62, no. 3 (February 7, 2017): 843–57.
15. Bader, Kenneth B., Kevin J. Haworth, Adam D. Maxwell, and Christy K. Holland. “Post Hoc Analysis of Passive Cavitation Imaging for Classification of Histotripsy-Induced Liquefaction in Vitro.” *IEEE Transactions on Medical Imaging* 37, no. 1 (January 2018): 106–15.
16. Khokhlova, VA, JB Fowlkes, WW Roberts, GR Schade, Z Xu, TD Khokhlova, TL Hall, AD Maxwell, YN Wang, and CA Cain. “Histotripsy Methods in Mechanical Disintegration of Tissue: Toward Clinical Applications.” *International Journal of Hyperthermia: The Official Journal of European Society for Hyperthermic Oncology, North American Hyperthermia Group* 31, no. 2 (March 2015): 145–62.
17. Zanelli, C. I., C. W. Hennige, and N. T. Sanghvi. “Design and Characterization of a 10 Cm Annular Array Transducer for High Intensity Focused Ultrasound (HIFU) Applications.” In *1994 Proceedings of IEEE Ultrasonics Symposium*, 3:1887–90 vol.3, 1994. <https://doi.org/10.1109/ULTSYM.1994.401959>.
18. Dupenloup, F., J. Y. Chapelon, D. J. Cathignol, and O. A. Sapozhnikov. “Reduction of the Grating Lobes of Annular Arrays Used in Focused Ultrasound Surgery.” *IEEE Transactions on Ultrasonics, Ferroelectrics, and Frequency Control* 43, no. 6 (November 1996): 991–98. <https://doi.org/10.1109/58.542044>.
19. Chen, Gin-Shin, Hsu Chang, Yi-Yuan Kuo, Winli Lin, Wen-Shiang Chen, and Wen-Yih Tseng. “Design and Fabrication of a Wide-Aperture HIFU Annular Array Transducer for the Treatment of Deep-Seated Tumors.” *AIP Conference Proceedings* 1359, no. 1 (September 12, 2011): 215–20. <https://doi.org/10.1063/1.3607908>.

Part III:
Thrombotripsy

Chapter VI – New transducer design and tools for the improvement of thrombotripsy

6.1 Introduction

6.1.1 Deep venous thrombosis in short

Deep venous thrombosis occurs when a thrombus (or blood clot) forms along a vein, usually in the legs of the patient. It may be non-occlusive and even asymptomatic when blood still flows in the vein, or occlusive when the thrombus impedes the blood flow leading to nearby tissues damaging, leg pain or swelling (Figure 72). The main danger that can occur is the break or the detachment of the thrombus (or a piece of thrombus), that will travel through the bloodstream and lodge in the lungs, causing a pulmonary embolism [3][4].

Today's principal solutions are anticoagulants, thrombolytics or compression stockings. These techniques either decrease the blood ability to clot, help to reduce the clot or prevent the leg swelling, but efficacy is usually hard to reach, especially in large thrombus.

When the thrombus are very large, other invasive solutions exist such as thrombectomy, that consist on removing the clot from inside the vein through a surgery. Nevertheless, thrombectomies present risks such as infections, excess bleeding, vein damage or pulmonary embolism in case of failure.

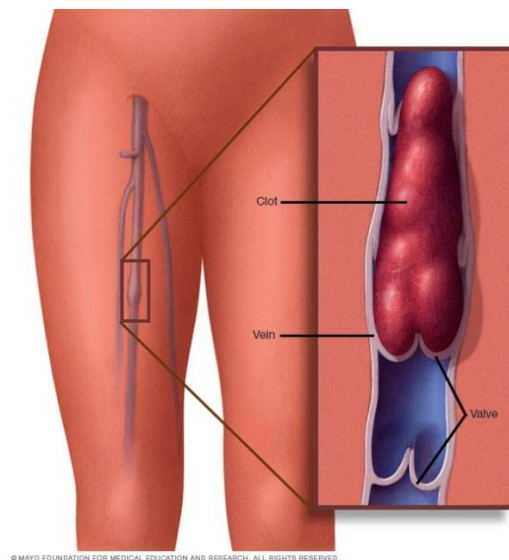


Figure 72 - Example of venous thrombosis [3]

The treatment of venous thrombosis using histotripsy, thrombotripsy, is presented as a non-invasive alternative solution that would ensure the restoring of the blood flow, without large debris release, avoiding the risks of an invasive surgery and in particular without the need of anaesthesia [1][2].

6.1.2 Thrombotripsy

Since 2009, the Department of Biomedical Engineering at the University of Michigan has been exploring non-invasive thrombolysis procedures using histotripsy, allowing to successfully recanalize thrombotic vein models and showing promising results [1]. It is based on the mechanical liquefaction of the thrombus using inertial cavitation, this creating a channel for blood flow. For efficacy, the channel shall be created along the whole thrombus to allow a full recanalization (Figure 73). The approach has evolved since then and, more recently, a new approach called “microtipsy” using single-cycle pulses at a therapeutic emission frequency of 1 MHz has been tested *in vitro* [12] and *in vivo* [13]. This approach allows to better control cavitation and to minimize the vein walls collateral damage.

In parallel, Physics for Medicine Paris, in partnership with the European Hospital Georges Pompidou and Cardiawave SA, is exploring a robotically assisted approach of the histotripsy deep venous thrombosis treatment. It has been proved effective on a swine model [2] using a 6-axis robotic arm to automatically move the transducer along the thrombus trajectory. The procedure is ultrasound guided and target positions along the thrombus are determined manually, cavitation being centred on the vein in order to avoid damaging its walls. It is based on a 2.25 MHz mono-element transducer (Imasonic©) for therapeutic emissions and a linear probe (SL10-2, SuperSonic Imagine©) for the ultrasound-based imaging. A second *in vivo* study using a porcine model is currently running. Occlusive thrombosis is obtained and left for 7 days to obtain a stiffer clot, closer to actual clinical thrombosis. After, thrombotripsy, the pigs are left for a 14-days follow up of the procedure evolution and success.

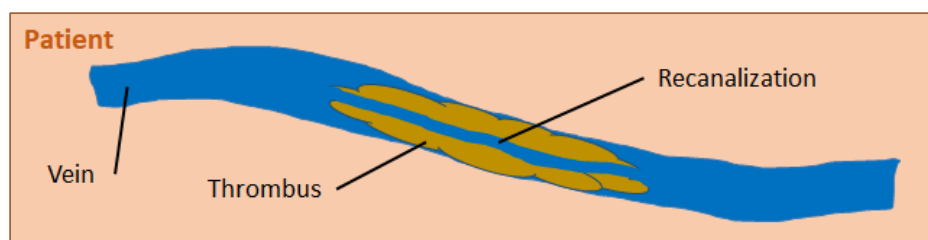


Figure 73 - Recanalization of the thrombotic vein, allowing the blood flow to go through the clot

Yet, important challenges remain as the therapeutic zone is limited by the intrinsic geometrical mono-element focal spot position, and thrombus outside this zone are difficult to be reached. The cavitation cloud position must be carefully placed to allow the creation of a single channel crossing the whole thrombus, enabling treatment efficacy and not destroying the healthy cells along the vein walls.

We propose the design of a new therapy transducer adapted to this pathology and allowing to focus high intensity ultrasound at different depths. Moreover, we wanted to optimize the central frequency to treat a larger zone and improve efficacy. The design was optimized using simulations.

Furthermore, we integrated passive cavitation imaging for accurate monitoring, and designed a specific human-machine interface (HMI) allowing to easily control the robotic arm and to get displacement and speed parameters. Those parameters are required to calculate the cavitation dose, necessary for an efficient thrombus disintegration.

6.2 New transducer design

6.2.1 Characteristics and challenges

The current therapy transducer used in the thrombotripsy project is a mono-element with a spherical shape and a central hole for the probe positioning, with a single focal spot. This system is practical for feasibility trials as the electronics needed to drive the ultrasound emission remain quite simple. Nevertheless, a single focal spot allows a very limited treatment zone, and as thrombus may reach different depths inter and intra patients following their morphology, it is necessary to design a system allowing to focus ultrasound at different depths.

A preliminary study in 30 patients at the European Hospital Georges Pompidou showed that in the targeted veins, the mean top position of the thrombus is 2.09 ± 0.7 cm and the mean bottom position of the thrombus is 4.84 ± 1.12 cm. Thus, the ideal thrombotripsy device should be able to reach a target dept comprised between 2 and 6 cm under the skin.

In order to get such a device allowing to reach multiple therapeutic focal spots, we propose the design of a multi-element annular transducer enabling an electronic steering along its central axis, ideally comprised between 2 and 6 cm above the imaging probe (Figure 74). As we saw in *5.1 Introduction*, multi-element annular transducers minimize the level of sidelobes

with a small number of channels, and they are a feasible solution for vascular applications as they allow an electronic dynamic focusing in the depth direction with few elements [7][8][9][10][11].

The further idea would be to ensure the transducer compatibility with Valvosoft®, so that the procedure is easily transposable to clinics.

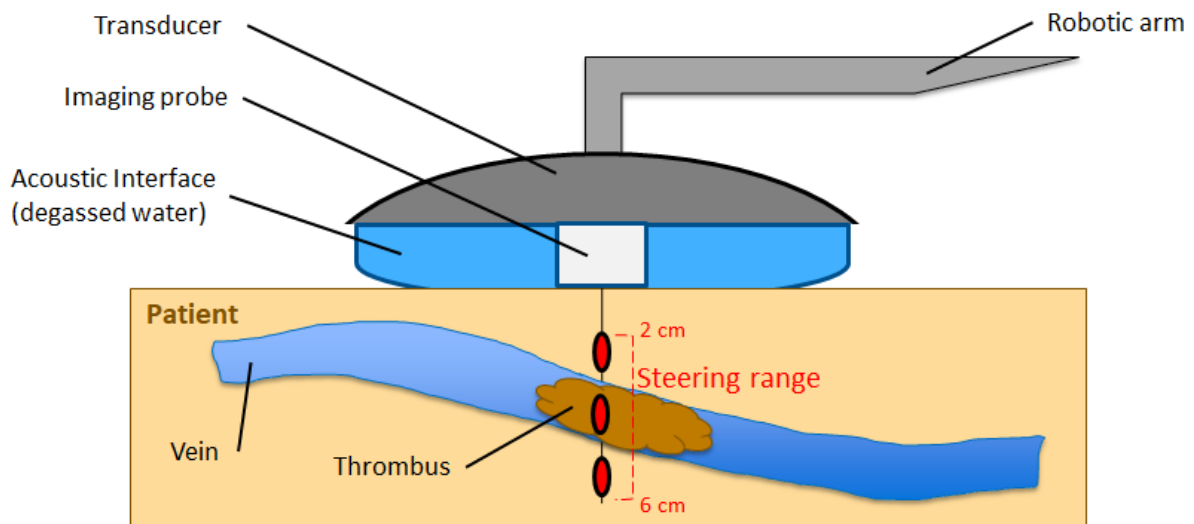


Figure 74 - Scheme presenting the thrombotripsy basic elements and the new transducer's steering range objective along its central axis

Moreover, in the first trials presented in [2] we observed that the cavitation cloud dimensions might be bigger, this allowing to dig a wider channel and to improve the recanalization efficacy without touching the vein walls.

On the one hand, for the nucleation of a bigger cavitation cloud, we aimed to design a transducer with a smaller central frequency. On the other hand, as ultrasonic absorption is inversely linked to frequency, a smaller frequency would lead to a better ultrasonic transmission through the tissues, which would also be beneficial for the procedure especially for the deep thrombus treatment.

6.2.2 Design based on simulations

The new transducer was conceived to be a multi-element annular spherical shaped transducer with a central hole for the probe positioning, and the number of piezoelectric elements was limited to 12 as we wanted to remain compatible with the electronics designed for the calcified aortic valve application.

In practice, the spherical radius of the transducer, that defines the transducer width, as well as its natural focus and the central hole diameter, were critical parameters for the steering range capabilities, as they define the piezoelectric elements' size (Figure 75). In fact, wide elements tend to be more directive, which deteriorates the steering range capabilities.

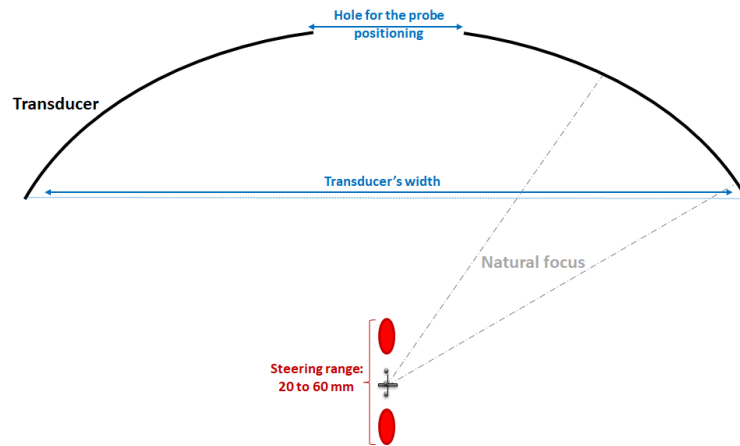


Figure 75 - Transducer's principal characteristics to be defined

First, we ran 2D numerical simulations in order to define the maximal element width (in wavelengths) we had to respect in order to enable a steering range of 4 cm. We fixed a transducer width of 110 mm, a central hole of 65 mm and a natural focus of 80 mm. We used K-Wave, V 1.1.1 [6] and we retrieved the mean properties of human tissues from the standard NF EN 60601-2-37 [5] which constitutes the basis of acoustic properties for ultrasonic phantoms and echographers.

We simulated the acoustic propagation in a medium containing tissue. We programmed one simulation for each different therapeutic target depth and using a low-pressure linear propagation model. The model consists in a simplified environment containing only the therapeutic transducer (with no imaging probe). We fixed the characteristics for the transducer and varied the transducer's number of elements as follows:

- Number of elements: 6, 8, 10, 11, 12, 14, 18, 24;
- Width: 110 mm;
- Central hole diameter: 65 mm;
- Natural focus: 80 mm;
- Central frequency: 1.6 MHz.

The steering range is composed by the depths where focalisation is possible at least at -3 dB, without side lobes outside the programmed focal depth. To evaluate the steering range:

- We considered the pressures along the central axis of the transducer for each target depth simulation;
- We normalized the whole data with the maximal pressure at the focal spots;
- We plotted the normalized pressures along the central axis of the transducer for each target depth.

Please find the results on Table 10. We may conclude that the maximal element's width to achieve a steering range of 4 cm is around **2.38 λ** .

Table 10 - Steering range capabilities following the transducer's mean pitch in millimetres and in wavelengths

| Number of elements | Mean element pitch (mm) | Number of wavelengths | Steering range (mm) |
|--------------------|-------------------------|----------------------------------|---------------------|
| 6 | 3.75 | 4.36 λ | [70-90] |
| 8 | 2.81 | 3.27 λ | [70-90] |
| 10 | 2.25 | 2.61 λ | [70-100] |
| 11 | 2.05 | 2.38 λ | [60-100] |
| 12 | 1.88 | 2.19 λ | [60-100] |
| 14 | 1.61 | 1.87 λ | [60-100] |
| 18 | 1.25 | 1.45 λ | [50-100] |
| 24 | 0.94 | 1.09 λ | [50-110] |

Next, our goal was to find the appropriate transducer characteristics to respect the steering range and to be coherent with the therapeutic procedure. In fact, a too large transducer would be problematic to match the patient's anatomic constraints, but we intended to design a wider transducer so that the active surface was more important, this facilitating the attainment of the cavitation threshold in terms of emission power.

We ran 3D numerical simulations also using K-Wave, V 1.1.1 [6]. As the imaging probe in this project is asymmetrical and it interferes with the therapeutic ultrasonic path, 2D simulations would not represent a trustful result and we were compelled to run 3D simulations. We used a low-pressure linear propagation model consisting in a simplified environment containing the therapeutic transducer and the imaging probe as shown in Figure 76.

We designed multiple transducers respecting our mechanical constraints and our need in steering range, and for each transducer we programmed one simulation for each different therapeutic target, containing the needed steering range of 2 to 6 cm under the probe.

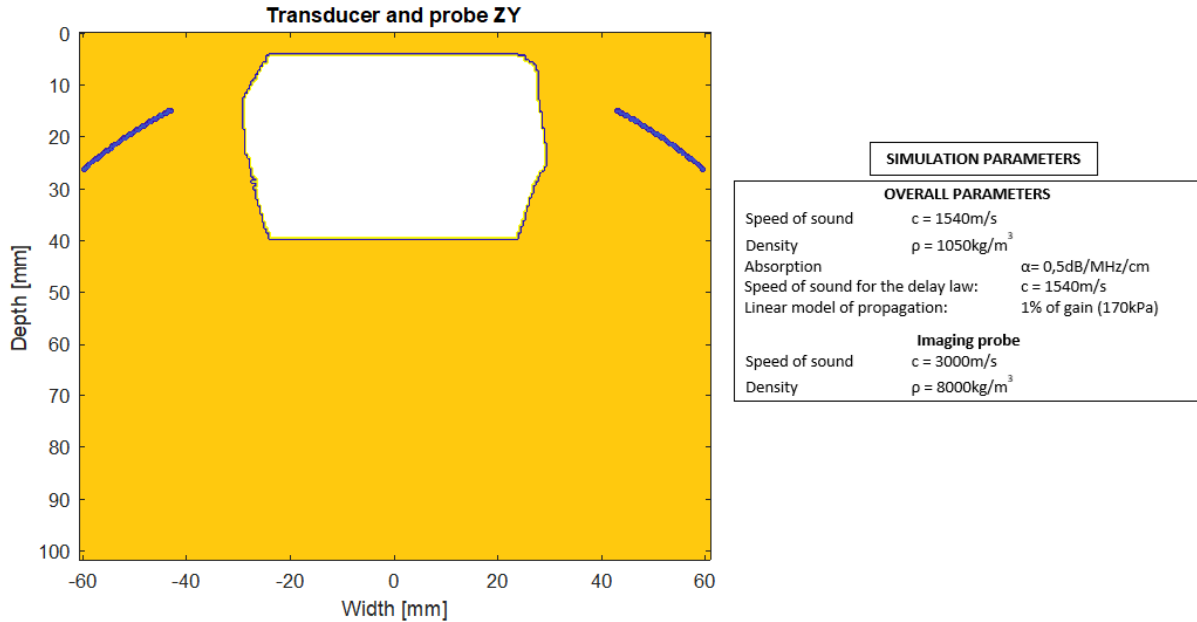


Figure 76 - Scheme of the simulation environment. White: Imaging probe (Y plane); Yellow: tissue; Blue: therapeutic transducer.
Source for tissue and absorption: [5]. The imaging probe acts as a reflector.

After several iterations considering different mechanical sizes of the transducer, we converged to a solution satisfying our constraints. Please find in Table 11 the principal characteristics of the actual mono-element and the proposed multi-element therapeutic transducers.

Table 11 - Principal characteristics of the actual mono-element and the proposed multi-element therapeutic transducers

| | Mono-element | Multi-element |
|--|--------------|---------------|
| Width (mm) | 90 | 130 |
| Natural focus (mm) | 60 | 90 |
| Central frequency (MHz) | 2.2 | 1.6 |
| Central hole (mm) | 65*29 | 85 (diameter) |
| Active surface (cm²) | 70 | 82 |

We chose a new central emission frequency of 1.6 MHz ($\lambda = 0.96$ mm). In our simulations, we found a maximal focal spot length of 6.67 mm at -3 dB at a 6 cm depth under the skin: this is the maximal reachable focal spot size. For safety reasons, the intention remains

to create a cavitation cloud with a maximal diameter inferior to 10 mm. Moreover, we gained 17% in terms of active surface. Please find in Annexe 1 the 3D rendering of both the therapeutic transducer and the imaging probe.

Please find on Figure 77 the 3D maximum of pressure simulation results for 2 cm depth above the probe and 6 cm depth above the probe. Both X and Y planes are presented for each case.

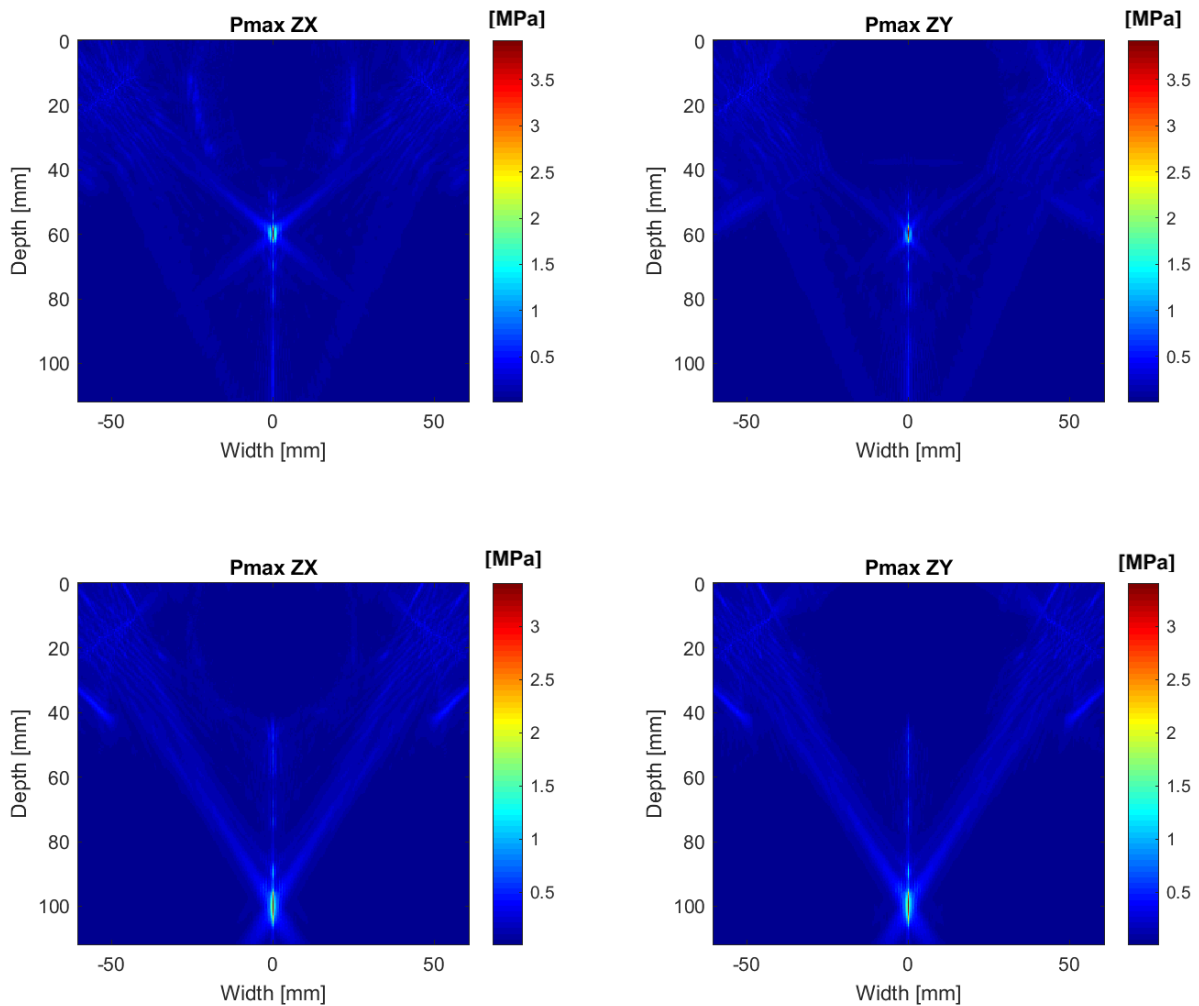


Figure 77 - Upper row: X plane (left) and Y plane (right) of the simulated pressure field for a therapeutic target depth of 20 mm under the probe
 Lower row: X plane (left) and Y plane (right) of the simulated pressure field for a therapeutic target depth of 60 mm under the probe

Please find on Figure 78 the steering range of the final solution. All depths from 2 cm to 6 cm under the imaging probe are above -3 dB (0.7079 in our normalized axis).

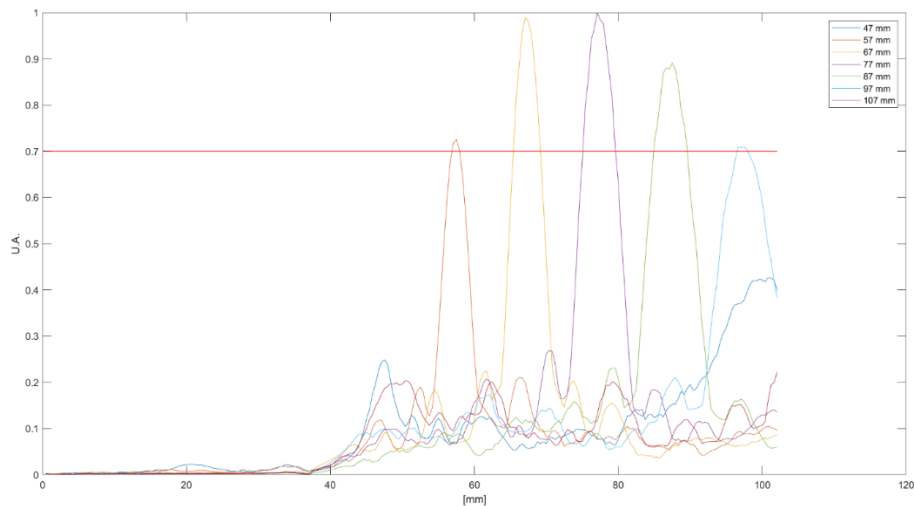


Figure 78 - Steering range of the proposed multi-element transducer

The red line at 0.7 on the y-axis represents the -3 dB focalisation limit

The effective steering range is in a range from 57 to 97 mm from the bottom of the transducer
 The head of the imaging probe is at a 37 mm depth, allowing an effective steering range from 20 to 60 mm from the skin

6.3 Device improvements, tools and further studies

The current thrombotripsy device is based on a 2.25 MHz mono-element transducer (Imasonic©) for therapeutic emissions and a linear probe (SL10-2, SuperSonic Imagine©) for ultrasound-based therapy monitoring [2]. The first improvement was the design of a new transducer for the procedure, allowing to reach multiple therapeutic depths electronically.

6.3.1 Passive cavitation imaging in thrombotripsy

Conventional B-Mode is currently used to monitor the procedure and allows a proper visualization of the cavitation cloud for superficial thrombus. However, the image quality decreases with the imaging depth, and the image contrast becomes insufficient to enable a non-operator dependant cavitation monitoring when we reach 6 cm under the skin.

The second improvement was the integration of the coherent passive cavitation imaging as presented in 2.2.1 *Theory* to the imaging sequence, to enable a more quantitative and objective visualization of the cavitation cloud position and size.

We ran a single preliminary *in vivo* experiment in a pig to investigate the feasibility of our method while thrombotripsy. The study was approved by the local ethical committee and the animal model was prepared as in [2]. The animal was fully anesthetized with isoflurane,

intubated and placed on a surgical table in dorsal decubitus position and were maintained on isoflurane (2.5 %) inhalation anesthesia for the duration of the procedure. The animal was monitored by a pulse-oximeter and an electrocardiogram monitor. For the therapeutic procedure, we used the same device as in [2].

Please find in Figure 79 a coherent cavitation map while thrombotripsy (left image) and the corresponding overlay over a B-Mode (right image). In a further study, the evaluation of the cavitation map CNR and the real-time capabilities of the sequence on a larger sample of pigs and with the new transducer at multiple target depths is to be conducted.

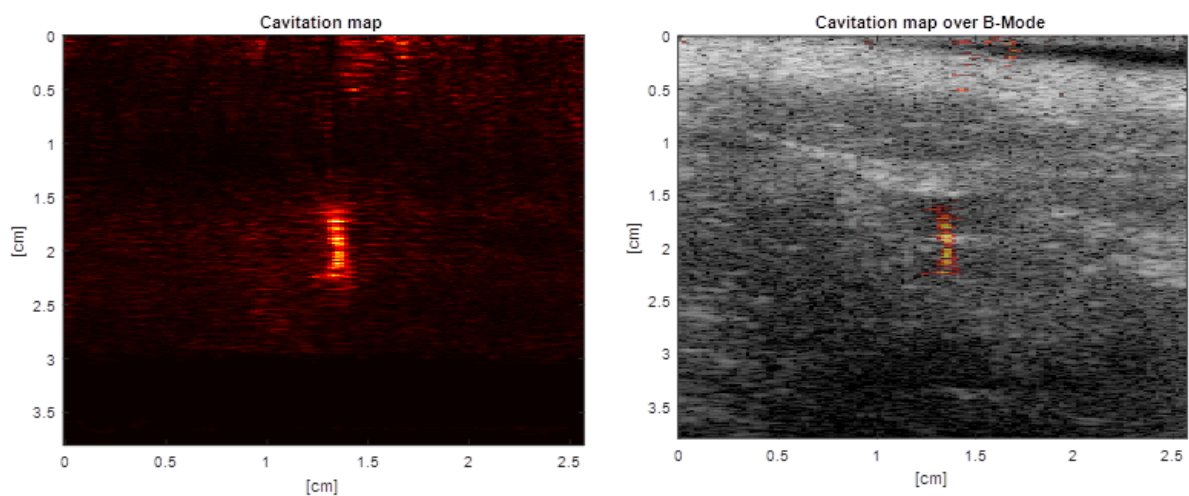


Figure 79 – Left: Cavitation cloud while thrombotripsy *in vivo*
Right: Cavitation cloud while thrombotripsy *in vivo* over B-Mode

6.3.2 Following improvements

Finally, thrombotripsy is a procedure that needs the displacement of the cavitation cloud along the clot in order to create the blood channel. For now, we program cavitation roundtrips along the clot using the robotic arm, and we conclude the procedure when we achieve recanalization.

We developed a software application using MATLAB © (Annexe 2) that allows to control the robotic arm movement positions and precision, acceleration and speed, and particularly it allows us to retrieve the trajectory positions and timings, and thus to deduce the cavitation cloud displacement characteristics. We hope to use this data in further studies to

investigate the optimal time needed per millimetre of clot to create the channel, and the cavitation dose.

Moreover, the software allows to precisely turn the probe 90 degrees in order to switch from axial to longitudinal planes of the vein and vice-versa on the image. This feature is important for the procedure guiding as:

- Axial planes allow to control that the cavitation cloud is inside the vein and does not touch the walls;
- Longitudinal planes allow to control the cavitation cloud global trajectory.

Additionally, the procedure could be greatly improved and for now unknown parameters such as the minimal cavitation exposition needed to create a channel, the cavitation cloud size, the robotic arm speed and the number of roundtrips are to be explored. Moreover, thrombus may have different mechanical characteristics, and thus the cavitation exposition time may differ following each specific patient.

In further studies, we also intend to run new *in vitro* trials to explore the acoustic parameters used for nucleation, as well to measure the cavitation time per millimetre of thrombus needed to create a channel based on our model, and to optimize the procedure time.

6.4 Discussion and conclusion

Thrombotripsy is a non-invasive solution to treat venous thrombosis, and the first feasibility results are promising. Nevertheless, challenges remain for the therapeutic procedure as we lack practical information such as the ideal cavitation cloud dimensions (and thus the therapeutic emission frequency), the effective clinical target depths or the cavitation time per millimetre of clot for recanalization.

This information will arrive through experience and new pre-clinical procedures, and the device will follow a technologic continuous improvement.

In this study, we conceived a new therapeutic transducer allowing to reach depths roughly between 2 and 6 cm under the skin, and we tested coherent passive cavitation imaging for the procedure monitoring. For now, we propose a complete device capable of treating

Chapter VI – New transducer design and tools for the procedure improvement

venous thrombosis, including a passive cavitation imaging monitoring and using a 6-axis robotic arm to automatically move the transducer along the thrombus trajectory. The system is adapted to pre-clinical trials and we hope will be easily transposable to clinics.

Other challenges remain for the improvement of the procedure, as for example it would be feasible to develop an adaptative therapeutic focusing based on an automatic image processing vein segmentation or to guide by using a bi-plane probe. The development of a specific human machine interface as well as ergonomic tools for the optimisation of the procedure are also improvement clues for the future developments of the device.

Bibliography

1. Maxwell, Adam D., Charles A. Cain, Alexander P. Duryea, Lingqian Yuan, Hitinder S. Gurm, and Zhen Xu. “Noninvasive Thrombolysis Using Pulsed Ultrasound Cavitation Therapy – Histotripsy.” *Ultrasound in Medicine & Biology* 35, no. 12 (December 2009): 1982–94.
2. Goudot, G., L. Khider, C. Del Giudice, T. Mirault, M. Vion, A. Galloula, P. Bruneval, M. Pernot, and E. Messas. “Robotic Assisted Thrombotripsy Allows High Accurate Venous Recanalization in a Porcine Model of Femoral Venous Thrombosis.” *Archives of Cardiovascular Diseases Supplements* 11, no. 1 (January 2019): 100–101.
3. <https://www.mayoclinic.org/diseases-conditions/deep-vein-thrombosis/symptoms-causes/syc-20352557>
4. <https://www.nature.com/articles/nrdp20156>
5. NF EN 60601-2-37/A1 :2015-11:2008-04. Medical electrical equipment - Part 2-37: Particular requirements for the basic safety and essential performance of ultrasonic medical diagnostic and monitoring (IEC 60601-2-37:2007)
6. <http://www.k-wave.org>
7. Pernot, Mathieu, Jean-François Aubry, Mickaël Tanter, Jean-Louis Thomas, and Mathias Fink. “High Power Transcranial Beam Steering for Ultrasonic Brain Therapy.” *Physics in Medicine and Biology* 48, no. 16 (August 2003): 2577–89. <https://doi.org/10.1109/TMI.2010.2076829>.
8. Chen, Gin-Shin, Hsu Chang, Yi-Yuan Kuo, Winli Lin, Wen-Shiang Chen, and Wen-Yih Tseng. “Design and Fabrication of a Wide-Aperture HIFU Annular Array Transducer for the Treatment of Deep-Seated Tumors.” *AIP Conference Proceedings* 1359, no. 1 (September 12, 2011): 215–20. <https://doi.org/10.1063/1.3607908>.
9. Zanelli, C. I., C. W. Hennige, and N. T. Sanghvi. “Design and Characterization of a 10 Cm Annular Array Transducer for High Intensity Focused Ultrasound (HIFU) Applications.” In *1994 Proceedings of IEEE Ultrasonics Symposium*, 3:1887–90 vol.3, 1994. <https://doi.org/10.1109/ULTSYM.1994.401959>.
10. Dupenloup, F., J. Y. Chapelon, D. J. Cathignol, and O. A. Sapozhnikov. “Reduction of the Grating Lobes of Annular Arrays Used in Focused Ultrasound Surgery.” *IEEE*

Transactions on Ultrasonics, Ferroelectrics, and Frequency Control 43, no. 6 (November 1996): 991–98. <https://doi.org/10.1109/58.542044>.

11. Chen, Gin-Shin, Hsu Chang, Yi-Yuan Kuo, Winli Lin, Wen-Shiang Chen, and Wen-Yih Tseng. “Design and Fabrication of a Wide-Aperture HIFU Annular Array Transducer for the Treatment of Deep-Seated Tumors.” *AIP Conference Proceedings* 1359, no. 1 (September 12, 2011): 215–20. <https://doi.org/10.1063/1.3607908>
12. Zhang, Xi, Gabe E. Owens, Hitinder S. Gurm, Yu Ding, Charles A. Cain, and Zhen Xu. “Non-Invasive Thrombolysis Using Histotripsy beyond the ‘Intrinsic’ Threshold (Microtripsy).” *IEEE Transactions on Ultrasonics, Ferroelectrics, and Frequency Control* 62, no. 7 (July 2015): 1342–55. <https://doi.org/10.1109/TUFFC.2015.007016>.
13. Zhang, Xi, Jonathan J. Macoskey, Kimberly Ives, Gabe E. Owens, Hitinder S. Gurm, Jiaqi Shi, Matthew Pizzuto, Charles A. Cain, and Zhen Xu. “Non-Invasive Thrombolysis Using Microtripsy in a Porcine Deep Vein Thrombosis Model.” *Ultrasound in Medicine and Biology*, 2017, 13.

General conclusion

Pulsed cavitation ultrasound therapies are promising technologies that might have a strong impact on the medical world. They are non-invasive, are very adaptable to multiple pathologies on different organs of the human body and represent less risk for the patient in comparison with the actual surgical gold standards.

A precise therapeutic focal spot positioning in relation to the target anatomic tissues and the follow-up of the cavitation cloud are crucial to ensure the safety and the efficacy of the procedure. As physicians does not have a direct visual feedback of the bubble cloud, a practical, non-invasive and real-time imaging modality would be ideal for the guiding and monitoring of the procedure.

At this day, PCUT are commonly guided and monitored by B-Mode echography, which is a non-invasive real-time imaging modality allowing to visualize the cavitation cloud in relation to the anatomy of the patient. As the bubble cloud is highly echogenic, the ultrasound imaging contrast is usually enough to allow a proper visualization of the cloud dynamics. Nevertheless, in deep or moving organs, ultrasound imaging performances decrease, and the contrast is not sufficient to ensure an objective differentiation between the bubble cloud and the tissues, compromising the evaluation of the cloud size, shape and effective position.

Furthermore, conventional B-Mode imaging allows to image a two-dimensional plane. However, the therapeutic transducer and the imaging probe are in most cases independent devices, and a mechanical misalignment between both transducers could lead the cavitation cloud out of the imaging plane, becoming “invisible” for the physician and thus a safety risk. Moreover, in heterogenic mediums such as the ribs, the skull or fatty tissues (c.f. *in vivo*), ultrasound can be aberrated and the focal spot could also be driven outside the imaging plane. As cavitation is a three-dimensional phenomenon and its position may be mechanically or acoustically out-of-plane, an adapted three-dimensional imaging technique would be ideal for the full monitoring of the procedure.

PCUT are rapidly approaching clinics, and as we get closer to the patient, we need to ensure a highly safe procedure, not to risk the patient’s life, and to ensure the maximum efficacy.

General conclusion

The goal of this thesis was to develop imaging modalities adapted to the guiding and monitoring of PCUT, in particular for cardiac applications and in particular for the treatment of calcified aortic stenosis developed by Cardiawave, Physics for medicine and the HEGP. We divided this work in three main parts: a first part concerning the development of cavitation imaging modalities as well as a global reflexion on the limitations of the current available techniques, a second part on the evaluation of the cavitation shape, position and dynamics on Cardiawave's therapy and a third part concerning the development of a novel transducer and the setup of cavitation imaging for thrombotripsy.

First, we set up a cavitation imaging modality based on existing passive acquisition techniques. By taking profit of the fact that PCUT bursts are very short, it is possible to effectively measure the propagation time of the emitted wave and thus to beamform a coherent "pulse-echo" image based on the reception by the imaging probe of the backscattered echoes from the therapeutic emissions. Both devices are synchronised. The obtained coherent passive image may next be filtered to obtain a "cavitation map" with a good contrast-to-noise ratio. Moreover, B-Mode imaging can be performed between the histotripsy pulses, and the "cavitation map" may be overlaid over the B-Mode to obtain the cavitation cloud characteristics in relation to the sonicated tissues.

Furthermore, if the pulses happen to be long (i.e. boiling histotripsy), there will be a loss in the axial resolution of the "cavitation map". We propose a solution for this problem by adding an extra therapeutic single cycle after the main burst, and to beamform the coherent passive image at this point following the same principle to obtain a "cavitation map" with a good resolution, despite a loss in contrast.

To outperform two-dimensional mechanical and acoustic limitations, we extended the modality to 3D imaging. The principle and the timings remain comparable to 2D, as well as the contrast-to-noise ratio of the resulting 3D "cavitation map". 3D imaging allows to monitor a whole sonicated volume and to evaluate the whole bubble cloud shape and position, and thus the whole treated area. As we saw, the cloud may be asymmetrical and in extreme cases secondary clouds may be nucleated off-centre, and a single imaging plane may give incomplete information. However, 3D imaging remains expensive, and the imaging quality may not be enough for our application.

General conclusion

Following these limitations, a good compromise between conventional B-Mode imaging and 3D imaging may be bi-plane imaging. This modality consists in using a probe with two orthogonal piezoelectric networks, and successively imaging the X and the Y planes. We designed and manufactured a cardiac adapted clinic bi-plane probe for the project and set up a beamforming technique based on a thin lens approximation, allowing to achieve a good compromise between image quality, monitored volume and frame rate. In fact, the great disadvantage of such technique is the loss on frame rate by half as compared to conventional imaging (as we have to beamform two planes). We tested its B-Mode capabilities and its performance in coherent passive cavitation imaging, giving promising results for Cardiawave's therapy guidance and monitoring.

Secondly, Cardiawave aims to treat calcified aortic valves using PCUT. There are natural constraints as the bubble cloud shall be big enough to cover an important surface of the valve for efficacy, but it shall be small enough not to go outside the valve. Following the specific configuration of Cardiawave's device, Valvosoft, we evaluated the cavitation cloud dynamics, dimensions and shape in simulations and *in vitro* to be sure that we respect such constraints. Moreover, we designed an alignment protocol to be deployed before each therapeutic procedure, allowing to quickly evaluate the position of the therapeutic focal spot in relation to the imaging plane.

Thirdly, Physics for Medicine in partnership with Cardiawave is exploring other target pathologies such as venous thrombosis, and a first feasibility study was published. We designed a new transducer for the project, allowing the focal spot steering along its central axis, and we integrated coherent passive cavitation imaging. Further improvements are to be conducted.

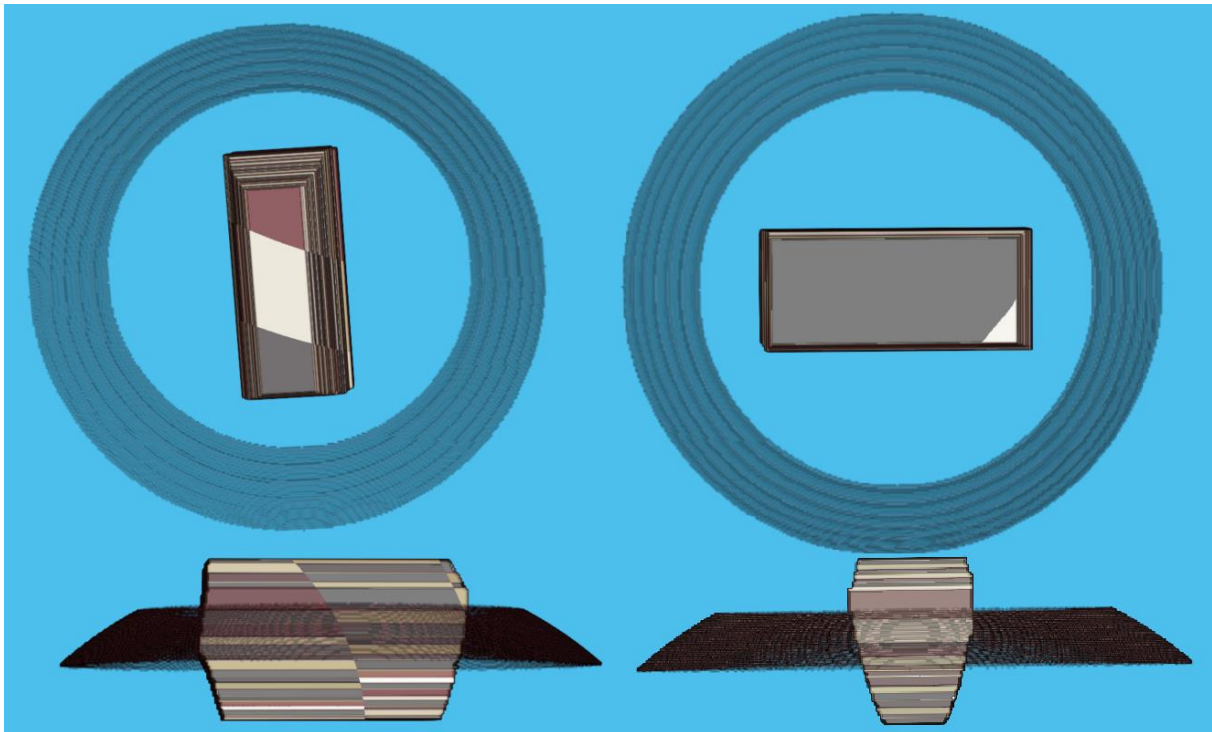
We can conclude that the result of this thesis was the development of a range of modalities allowing to better guide and monitor PCUT, and the global reflexion on the needs and the limitations of the procedure. The effective utilization or not of our modalities will depend on each device constraints, as well as on the target tissues and on each pathology's specific requirements and boundaries. There is still a lot of work to be done to develop and to improve PCUT guiding and monitoring modalities, and international standards are to be worked in order to homogenise PCUT engineering and testing.

Annexes

Annexe 1 – Designed therapeutic transducer and imaging probe for thrombotripsy

3D rendering of the designed therapeutic transducer for thrombotripsy and the linear probe (SL10-2, SuperSonic Imagine©) embedded in its central hole.

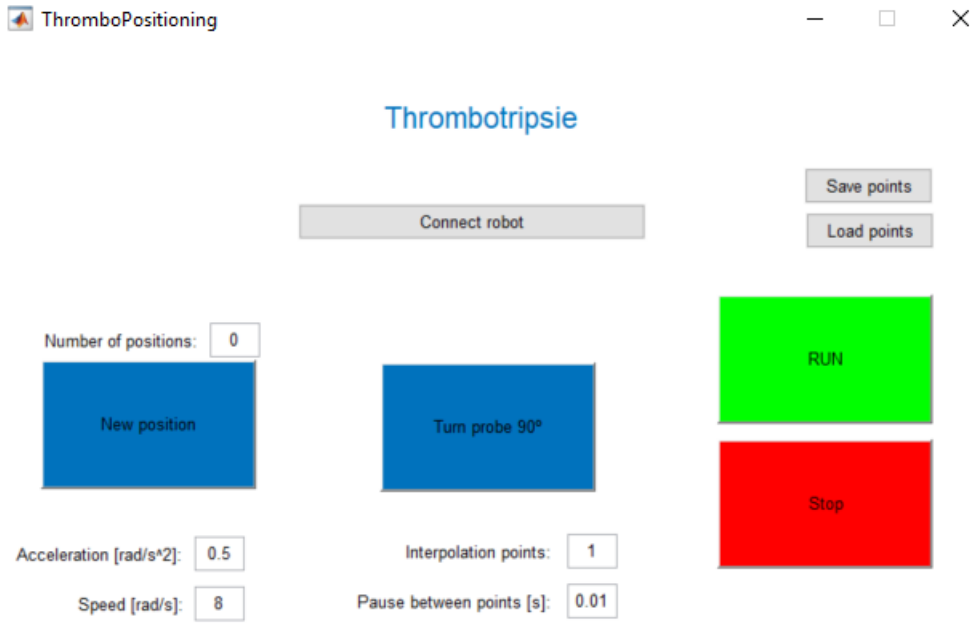
Upper left: Bottom view of the probe and the transducer; Upper right: Top view of the probe and the transducer; Bottom left: Side view of the probe and the transducer (plane Y); Bottom right: Side view of the probe and the transducer (plane X).



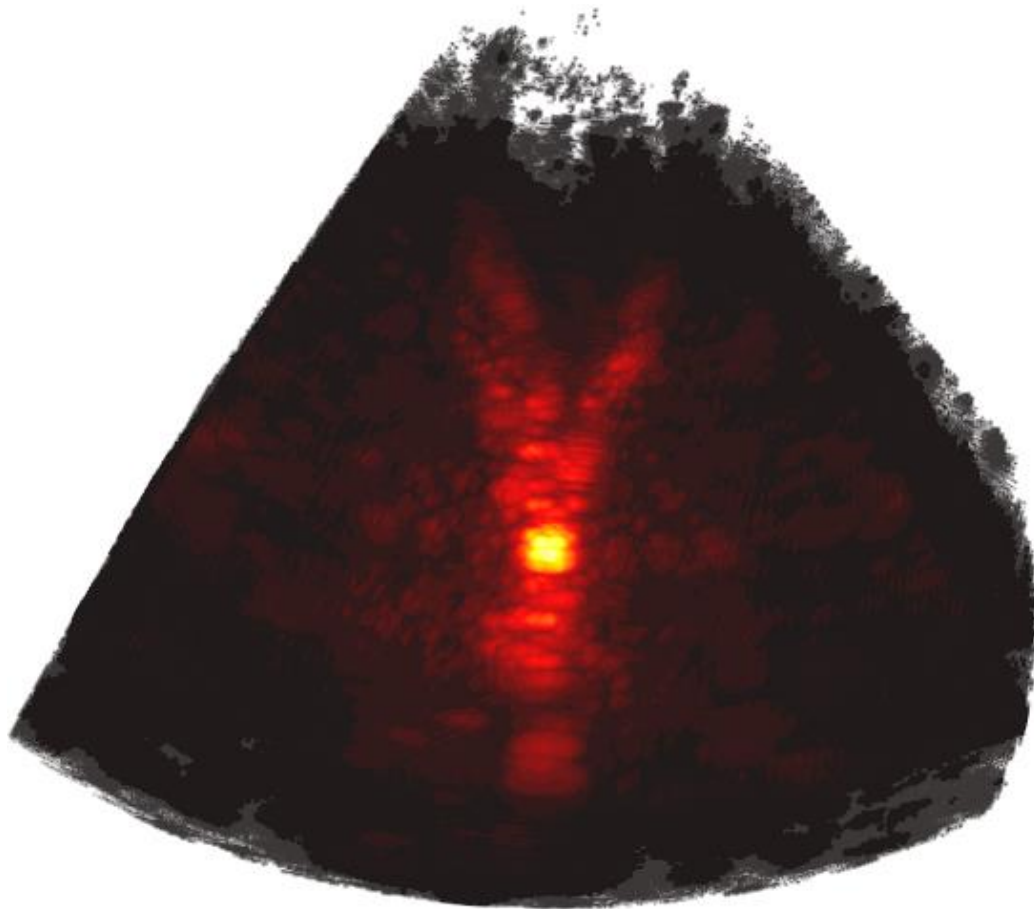
Annexe 2 – Human machine interface designed to control the robotic arm in thrombotripsy

Human machine interface designed to control the robotic arm while thrombotripsy and to retrieve the cavitation bubble displacement speed and trajectory.

Annexes



Annexe 3 – 3D coherent passive image rendering while cavitation in water



Annexe 4 – Acoustic characteristics of biological tissues and other materials

Source : ULTRASONS - IMAGERIE - ECHOGRAPHIE MEDICALE, Christian CACHARD, Olivier BASSET, Philippe DELACHARTRE, INSA Lyon – Creatis, p. 18

| Tissus biologiques et matériaux | Température (° C) | Densité ρ (kg m ⁻³) | Célérité c_L (m s ⁻¹) | Impédance acoustique z_L (kg m ⁻² s ⁻¹) | Atténuation α (dB cm ⁻¹) à 1 MHz |
|---------------------------------|-------------------|--------------------------------------|-------------------------------------|--|---|
| Air | 0 | 1,28 | 331 | 430 | 12 |
| | 20 | 1,20 | 344 | | |
| Eau | 20 | 1000 | 1480 | $1,52 \times 10^6$ | 0,0022 |
| Sang | 20 | 1060 | 1530 | $1,62 \times 10^6$ | 0,18 |
| Graisse | | 920 | 1410 à 1470 | $1,34 \text{ à } 1,39 \times 10^6$ | 0,6 |
| Muscle | | 1070 | 1550 à 1640 | $1,65 \text{ à } 1,7 \times 10^6$ | 1,2 |
| Foie | | 1060 | 1550 | $1,65 \times 10^6$ | 0,9 |
| Rein | | 1040 | 1560 | $1,62 \times 10^6$ | |
| Os | 20 à 37 | 1200 à 1810 | 2700 à 4100 | $3,2 \text{ à } 7,8 \times 10^6$ | 20 |
| Poumon | 35 | | 650 | $0,26 \times 10^6$ | 40 |
| Peau | | | 1519 | $1,58 \times 10^6$ | |
| Vaisseaux | | 1080 | 1530 | $1,65 \times 10^6$ | |
| Tissus mous | | | 1540 en moyenne | $1,63 \times 10^6$ | |
| Sein | | | 1440 à 1550 | | $1,68 \pm 0,48$ |
| Quartz | | | 5750 | $1,52 \times 10^7$ | |

RÉSUMÉ

La thérapie par ultrasons cavitationnels pulsés (PCUT) est une approche thérapeutique non invasive efficace pour traiter diverses indications médicales. Elle repose sur les effets mécaniques générés par des bulles de cavitation inertielle dans une zone focale très contrôlée. Ce type de thérapie se caractérise par une émission extrêmement intense d'ultrasons focalisés, à impulsions très courtes et sans effets de chauffe. Mise au point dans les années 2000, la PCUT reste toutefois très récente et il est nécessaire de développer de nouvelles modalités d'imagerie pour le guidage et le suivi de la procédure. En effet, la visualisation des bulles en échographie mode B est souvent limitée dans les organes profonds tels que le foie et le cœur, et elle reste qualitative pour l'opérateur. De plus, la cavitation inertielle est un phénomène tridimensionnel, ce qui crée le besoin de développer un outil d'imagerie tridimensionnel : par des raisons de sécurité, il est essentiel de pouvoir placer précisément le point focal thérapeutique sur la zone cible. En outre, à ce jour, il n'existe pas de normes internationales pour la PCUT.

La PCUT s'est avérée être une solution efficace pour le traitement de la sténose aortique calcifiée (SAC), valvulopathie la plus fréquente dans les pays développés et véritable problème de santé publique du fait du vieillissement de la population, et Cardiawave, en partenariat avec Physique pour la Médecine Paris et l'Hôpital Européen Georges Pompidou, développe une approche de thérapie par PCUT consistant à réparer la valvule aortique sans la remplacer. Aucune intervention chirurgicale n'est nécessaire, et cela pourrait représenter une alternative complètement non invasive et une solution complémentaire aux lourdes interventions chirurgicales actuelles.

Ce travail de thèse explore différents outils pour le guidage et la surveillance du traitement de la SAC par PCUT.

Premièrement, une nouvelle modalité d'imagerie du nuage de cavitation basée sur une acquisition ultrasonore passive cohérente et associée à un filtre spatio-temporel a été développée, adaptée aux applications cardiaques et facilement transposable aux appareils à ultrasons du commerce. La modalité tire parti des impulsions courtes de la PCUT et, en connaissant les retards absolus entre l'émission thérapeutique et la réception des échos par la sonde, elle permet de créer une image cohérente en « pulse-écho » du champ ultrasonore thérapeutique. La modalité a d'abord été testée en 2D, *in vitro* et *in vivo*, puis transposée en 3D.

Deuxièmement, nous avons développé des outils de sécurité pour assurer le guidage et la surveillance de la thérapie. La cavitation étant un phénomène tridimensionnel, il était nécessaire, en fonction de la conception du dispositif Cardiawave, d'assurer le positionnement précis du point focal thérapeutique. Une nouvelle sonde cardiaque a été conçue pour le projet. Des acquisitions ultra-rapides bi-planes en mode B ont été développées et testées, puis associées à l'imagerie de cavitation. Une modalité de formation d'image spécifique permettant une cadence d'image suffisante pour la surveillance et adaptée aux spécifications mécaniques de la sonde a également été mise au point sur la base de théories physiques et de simulations.

Simultanément, la PCUT est présentée comme une solution potentielle pour traiter la thrombose veineuse profonde en créant un canal pour permettre le passage du sang à travers le thrombus, en utilisant la cavitation inertielle. Nous avons proposé la conception d'un nouveau transducteur de thérapie adapté à cette pathologie et permettant de focaliser des ultrasons de haute intensité à différentes profondeurs. La conception a été optimisée à l'aide de simulations. Enfin, nous avons couplé l'ensemble du système PCUT, assisté par robot, à l'imagerie de cavitation pour permettre de positionner facilement la cible, et aboutir à un dispositif transposable en clinique.

MOTS CLÉS

[Thérapie ultrasons focalisés, guidage et monitoring, rétrécissement aortique]

ABSTRACT

Pulsed cavitation ultrasound therapy (PCUT) is an effective non-invasive therapeutic approach in various medical indications that relies on the mechanical effects generated by inertial cavitation bubbles in a controlled focal area. It is characterized by a short-pulse high intense focused ultrasound emission with no heating effects. This technology, developed in the 2000's, remains however very recent and there is a need to develop new imaging modalities for the guiding and the monitoring of the procedure. In fact, the B-Mode visualization of the bubble cloud is often limited in deep organs such as the liver and the heart and remains qualitative for the operator. Moreover, inertial cavitation remains a three-dimensional phenomenon which awakens the need for a three-dimensional imaging tool development, as for safety reasons it is essential to be able to precisely place the therapeutic focal spot on the target zone. At this date, there are no international standards for PCUT.

PCUT has been proved to be an effective solution for the calcified aortic stenosis (CAS) treatment, and Cardiawave, in partnership with Physics for Medicine Paris and the European Hospital Georges Pompidou, is developing an approach which consists in repairing the aortic valve, not replacing it. No surgery is required, and it could represent an alternative and a complementary solution to current surgical interventions.

The present work explores different tools for the guidance and monitoring of the PCUT treatment of CAS.

First, a new modality for the cavitation cloud imaging based on a passive coherent acquisition combined with a spatiotemporal filter was developed, adapted to cardiac applications and easily transposable to commercial ultrasound devices. The modality takes advantage of the short-pulses of PCUT, and by knowing the absolute time delays it allows a "pulse-echo" coherent beamforming of the therapeutic ultrasonic field. The modality was first tested in 2D, in vitro and in vivo, then transposed to 3D.

Secondly, we developed safety tools to ensure the guiding and the monitoring of the therapy. As cavitation is a three-dimensional phenomenon, following Cardiawave's device design it was necessary to ensure the sharp positioning of the therapeutic focal spot. A new cardiac probe was designed for the project. B-Mode and bi-plane ultrafast acquisitions were developed and tested. A specific beamforming allowing a sufficient frame rate and adapted to the mechanical specifications of the probe was also set up based on theory and simulations.

Simultaneously, PCUT is presented as a potential solution to treat venous thrombosis by creating a channel for blood on the thrombus, using cavitation. We proposed the design of a new therapy transducer adapted to this pathology and allowing to focus high intensity ultrasound at different depths. The design was optimized using simulations. Finally, we integrated the whole robotically assisted PCUT system for the therapy allowing cavitation monitoring and an easy positioning of the target, hopefully easily transposable to clinics.

KEYWORDS

[Focused ultrasound therapy, guidance and monitoring, aortic stenosis]